NUMERICAL AND EXPERIMENTAL STUDIES FOR OPTIMIZATION OF LASER WELDING OF 2205 DUPLEX STAINLESS STEEL

THESIS SUBMITTED

By

ARITRA GHOSH
REG NO: D-7/ISLM/40/18

DOCTOR OF PHILOSOPHY (ENGINEERING)

SCHOOL OF LASER SCIENCE AND ENGINEERING

FACULTY OF INTERDISCIPLINARY STUDIES, LAW & MANAGEMENT

JADAVPUR UNIVERSITY

KOLKATA – 700 032, INDIA

2023

JADAVPUR UNIVERSITY

KOLKATA-700 032, INDIA

REG NO: D-7/ISLM/40/18

1. Title of the Thesis

"NUMERICAL AND EXPERIMENTAL STUDIES FOR OPTIMIZATION OF LASER WELDING OF 2205 DUPLEX STAINLESS STEEL"

2. Name, Designation & Institution of the Supervisor

Dr. SANJIB KUMAR ACHARYYA

Professor

Department of Mechanical Engineering

Jadavpur University

Kolkata- 700032

India

List of Publications (Referred Journals):

1. “Numerical Simulation of the Laser Welding of 2205 Duplex Stainless Steel”, A. Ghosh, D. Misra and S.K. Acharyya, International Journal of Laser Science 2019, Vol. 1, pp. 293–313.

2. “Experimental and Numerical Investigation on Laser Welding of 2205 Duplex Stainless Steel”, Aritra Ghosh, Dipten Misra, Sanjib Kumar Acharyya, Lasers in Manufacturing and Materials Processing (2019) 6:228–246.

3. “Comparison of Molten Pool Behaviour of Different Numerical Models for Laser Welding of 2205 Duplex Stainless Steel”, Aritra Ghosh, Paramasivan Kalvettukaran, Dipten Misra, Sanjib Kumar Acharyya, Lasers in Manufacturing and Materials Processing. (Accepted for Publication)

List of Patents: Nil

List of presentation in National and International Conferences:

1. “Estimation of Weld-Bead Dimensions in Laser Butt Welding of 2205 Duplex Stainless Steel”, Aritra Ghosh and Dipten Misra, National Conference on Advanced Functional Materials Processing & Manufacturing (NCAFMPM-2017) CSIR-CMERI Durgapur.

2. “Experimental Investigation on Laser Welding of 2205 Duplex stainless steel”, Aritra Ghosh and Dipten Misra, INCOM18: Proceedings of the 1st International Conference on Mechanical Engineering Jadavpur University Kolkata

3. “Experimental Investigation on the Effect of Pulse Width on Laser Welding of 2205 Duplex Stainless Steel”, Aritra Ghosh, Paramasivan Kalvettukaran, Dipten Misra, Sanjib Kumar Acharyya, Virtual International Conference on Recent Advancements in Mechanical Engineering (ICRAME 2021)

To be communicated

1. “Experimental study on weld pool dimensions and mechanical properties of laser-welded 2205 duplex stainless steel”, Aritra Ghosh, Paramasivan Kalvettukaran, Dipten Misra, Sanjib Kumar Acharyya.

Statement of Originality

I Aritra Ghosh registered on 07/02/2018 do hereby declare that this thesis entitled "NUMERICAL AND EXPERIMENTAL STUDIES FOR OPTIMIZATION OF LASER WELDING OF 2205 DUPLEX STAINLESS STEEL" contains literature survey and original research work done by the undersigned candidate as part of Doctoral studies.

All information in this thesis have been obtained and presented in accordance with existing academic rules and ethical conduct.

I declare that, as required by these rules and conduct, I have fully cited and referred all materials and results that are not original to this work. I also declare that I have checked this thesis as per the "Policy on Anti Plagiarism, Jadavpur University, 2019", and the level of similarity as checked by iThenticate software is 7%.

Signature of Candidate: Aritra Ghosh

Date : 19/09/23

Certified by Supervisor(s):

(Signature with date, seal)

1. Dr. Sanjib Kumar Acharyya Acharyya 19.09.23

Professor
Dept. of Mechanical Engineering
Jadavpur University, Kolkata-32

CERTIFICATE FROM THE SUPERVISOR

This is to certify that the thesis entitled "NUMERICAL AND EXPERIMENTAL STUDIES FOR OPTIMIZATION OF LASER WELDING OF 2205 DUPLEX STAINLESS STEEL" submitted by Aritra Ghosh (Reg. No.: D-7/ISLM/40/18), who got her name registered on February, 2018 for the award of Ph.D. (Engineering) degree of Jadavpur University is absolutely based upon her own work under my supervision and neither her thesis nor any part of the thesis has been submitted for any degree/diploma or any other academic award anywhere before.

Acharyya 19.09.23

(Dr. Sanjib Kumar Acharyya)

Signature of the Supervisors
and Date with Official seal

Professor
Dept. of Mechanical Engineering
Jadavpur University, Kolkata-32

Acknowledgements

Truly speaking I believe that just a mere “thank you” doesn’t do proper justice to peoples’ contribution towards most of the endeavours. But usually, that remains the only thing we can offer, not just to acknowledge their efforts but also to pacify our consciences. Foremost, I would like to thank Jadavpur University, for providing me such a graceful opportunity. I believe the man who epitomizes this process is my teacher Shri Dipten Mishra, Director of our school. First, I would like to express my deepest gratitude to my respected supervisor, Dr. Sanjib Kumar Acharyya for his constant support and encouragement throughout the duration of work. His constructive suggestions and comments provided me more insight to this research work. I feel lucky that they gave me the opportunity to carry out my research under their guidance and supervision in spite of their busy schedule.

I am grateful to all the faculty members associated with our school, who have given me valuable suggestions throughout my work. I feel really blessed for receiving advice from late Dr. Asish Bandyopadhyay. I am grateful to the authority of Jadavpur University for providing the instrumental and laboratory facilities. This work is carried out with the financial support from TEQIP-COE Phase II & III of Jadavpur University. I feel that, I have been able to realise the meaning of a teacher by working with some of the best teachers whom I have met, during my tenure in this campus. I thank them all. I would like to thank senior research scholars who gave me their precious time for improvement of this project. I would also like to express gratitude to all laboratory assistants in the Department of Mechanical Engineering for always expending their helping hands.

I am very much thankful to all the members of the School of Laser Science & Engineering at Jadavpur University. I would like to offer my sincere gratitude to my senior Dr. Paramasivan K, for mentoring me continuously with his valuable suggestions during the course of my work. I would like to thank all non-teaching staff for their constant help and support. Although it could not be simply expressed by words, I thank my parents, my husband and my daughter, for their constant support and encouragement throughout my life. Most importantly, I would like to give God the glory for all the efforts I have put into the work and for giving me the physical strength and mental perseverance to carry out the work.

Aritra Ghosh

School of Laser science and Engineering

Jadavpur University, Kolkata

Abstract

The present work proposes to explore laser welding of duplex 2205 stainless steel through numerical and experimental methods for optimization of process parameters. Different types of welded joints are used in industry. Laser welding can be accomplished with comparatively lesser amount of heat and the heat can be delivered through a smaller and precise beam resulting in less residual deformation and a deeper penetration which helps in achieving a higher weld strength, a smaller bead width with better aesthetics, as well as a narrow heat affected zone (HAZ) such that lesser amount is affected by the thermal degradation process. Due to such advantages laser welding offers a promising route for welding compared to other welding techniques. Why we choose laser welding process was described above but reason behind choosing 2205 duplex stainless is its unique properties which should be explored much. Duplex stainless steels (DSS) represent a class of stainless steels with dual microstructure consisting of approximately equal proportions of ferrite and austenite phases. This balanced microstructure offers a favorable combination of mechanical strength and corrosion resistance, rendering DSS a popular choice for pipelines, handling high pressure and corrosive fluids. Along this, mechanical and chemical properties are being stable in elevated temperature. As it is predictable to reach very high temperature in welding process, the consistency of properties on such high heat is desirable. Application of the Duplex stainless-steel finds use in diverse fields, such as automotive industries, process industries, aerospace, marine and fabrication industries.

Laser welding process includes some process parameters to achieve some response parameters. It is known that a welding will be defined as satisfactory or complete only if it can offer quite high strength in joints. To ensure higher strength in joints we have to aim maximum penetration of heat into the material as well as minimum bead width so that heat affected zone can be minimal. A large area of heat affected zone can rise brittleness of weld materials. Higher strength weld joints require precise selection range of input or process parameters. Laser power, welding speed, beam diameter and pulse width are generally applied as laser welding process parameters where depth of penetration, bead width, ultimate tensile strength, yield strength, elongation and young's modulus are required response parameters to identify the quality of welding. So, for accruing high quality strength joints we have to identify optimum process parameters. In experimental way if we try to recognize this optimum range then we have to complete a very large number of experiments which will be

very expensive and time consuming as well. Due to this reason in present research we decided to develop a three-dimensional finite element model utilizing COMSOL MULTIPHYSICS® for laser welding simulation from which we can get idea of proper range of process parameters.

At first, we developed an isotropic model for laser welding including phase change with physical and temperature depended thermal properties of material. We applied power, welding speed and beam diameter as input. Symmetry was taken into account throughout the surface of the welding orientation. In order to choose the right quantity of components, a series of convergence trials were carried out, paying special attention to the depth axis along with regions adjacent to the weld alignment. Extremely condensed mesh was produced around the area close to the weld line, and coarse mesh was proposed around the left-over area. As output we are restricted to achieve only depth of penetration, bead width and temperature distribution from the simulation model. Mechanical characterization is not possible from the model. We have then validated those outputs with published results to check its adequacy and noticed that this method provides acceptable match though not exactly identical. Now based on this process we simulated quite a large number of welding to get a safe operating window and optimum process parameters, based on which we can go ahead for experimental investigation. But in actual, thermal properties are not consistent with elevated temperature in each direction, so isotropic simulation process needs to upgrade into anisotropic process. We have followed the anisotropic approach for simulation model and done some welding experiments to validate the results.

As we stated above that only depth of penetration and bead width can be measured from model, so we compared these two responses and found better match against isotropic model. With the help of optical microscope, we measured depth and width of fusion zone, additionally we identified the heat affected zone. For better realization of weld, base and HAZ zone we utilized scanning electron microscope, from where we understood the grain orientation and grain size variations at different zone. Welding quality cannot be only defined by depth of penetration and bead width without mechanical characterization. So, we decided to go for mechanical characterization of those few welded sample along with base metal by doing tensile test and hardness test. Here we noticed that hardness is very high at weld zone where after welding base zone hardness remain unchanged regarding base metal and HAZ has very low hardness value. But for tensile test we found that base material offers higher

ultimate tensile strength and elongation than welded materials. So, a clear mechanical property degradation was noticed.

Only depth of penetration and bead width are not sufficient at all to provide good quality weld until it offers satisfactory strength. So still there are some requirements to upgrade the present simulation model. So far for both simulation process we only consider isotropic and anisotropic approach but it is obvious to consider fluid flow as in reality there is a situation molten metals flows, so to achieve accurate simulation it is required to include the CFD in finite element method. Three numerical models are developed considering the flow in the molten pool to be laminar in the first model and turbulent in the two other models. We measured depth and width from these three CFD model and validate with experimented one. We found a turbulent model provide best match to the experimented result so far against isotropic and anisotropic model. Although we were still unable to found the strength of joints from this CFD model so we decided to do a bunch of experimental welding investigation to check depth of penetration, bead width along with ultimate tensile strength and elongation taken into account. And depending on the experimental result we create a design matrix to analyse response parameters by developing mathematical corelation between process and response parameters to predict future responses with another set of process parameters. Also, we upgrade the optimization model with taking into account depth of penetration, bead width along with ultimate tensile strength and elongation and found optimum process parameters which can deliver maximum ultimate strength and elongation with maximum penetration and minimum bead width. Considering weld response parameters like depth of penetration, bead width along with mechanical properties like ultimate tensile strength and elongation is appraisable to identify the optimum weld conditions under laser welding process.

Table of Contents

List Publications based on this Thesis…….. I

Statement of originality…… II

Certificate from the Supervisors…… III

Acknowledgements …….. IV

Abstract …… V

Table of Contents…….. VIII

Nomenclature and Abbreviations …… XIII

List of Figures …….. XV

List of Tables…… XXI

Chapter 1: Introduction to LASER, Explanation of proposed work and Literature survey *1*

1.1 Introduction…….. *2*

1.1.1. But joint…….. *3*

1.1.2. Lap joint…….. *3*

1.1.3. T-joint…….. *3*

1.1.4. Advantages of Laser Welding…….. *4*

1.1.5. Restrictions of the Laser Welding Process…….. *4*

1.1.6. Modes of Laser Welding…….. *5*

1.1.6.1.Conduction mode…….. *5*

1.1.6.2.Transition mode…….. *5*

1.1.6.3.Keyhole or penetration mode…….. *6*

1.2 Proposed Research Work…… *7*

1.3 Brief Literature Survey…… *10*

1.4 Objectives of Present research work…… *19*

Chapter 2: Finite Element Simulation of Laser butt Welding of 2205 Duplex stainless steel (isotropic) 21

2.1. Introduction 22
2.2. Finite Element Modeling 22
2.2.1. Governing Equation and Boundary Conditions 25
2.2.2. Validation of Numerical Model 26
2.3. Development of Mathematical Model 28
2.3.1. Response Surface Methodology 28
2.3.2. Design Matrix 29
2.4. Results and Discussion 30
2.4.1. Transient Temperature Field Analysis 30
2.4.2. Analysis of Variance (ANOVA) 39
2.4.2.1. Effect of Process parameters on the Bead Width 40
2.4.2.2. Effect of Process parameters on the Depth of Penetration 43
2.4.2.3. Effect of Process parameters on the Maximum Temperature 46
2.4.3. Optimization 50
2.5. Conclusions 51

Chapter 3: Finite element simulation (anisotropic) and Experimental validation 52

3.1. *Introduction* 53
3.2. *Finite Element Simulation* 53
3.2.1. Governing Equation and Boundary Conditions 56
3.3. Experimental Investigation 58
3.3.1. Experimental Set Up 58
3.3.2. Materials and Methodology 59
3.4. Results and Discussion 62
3.4.1. Validation of Simulated Weld bead geometries with Experimental study 62
3.4.1.1 Temperature distribution for different welding speed (simulation model) ... 62
3.4.1.1.1. Effect of Welding Speed on Microstructure 63
3.4.1.1.2. Effect of welding speed on tensile strength 69
3.4.1.1.3. Effect of welding speed on microhardness 71

3.4.1.1.4. Effect of welding speed on XRD..... 73
3.5 Conclusion 74

Chapter 4: Experimental study on weld pool dimensions and mechanical properties of laser-welded 2205 duplex stainless steel with multiobjective optimization 76

4.1. Introduction..... 77
4.2. Experimental procedure and measurement equipment..... 78
4.3. Response surface methodology (RSM) and design matrix..... 81
4.4. Results and Discussion..... 83
4.4.1. Microstructure Analysis and Tensile strength of the base material..... 83
4.4.2. Microstructure analysis and tensile strength of the welded samples..... 84
4.4.2.1. Analysis of Bead width using ANOVA..... 87
4.4.2.2. Analysis of depth of penetration using ANOVA..... 88
4.4.2.3. Analysis of ultimate tensile strength using ANOVA..... 89
4.4.2.4. Analysis of elongation using ANOVA..... 90
4.4.2.5. Effect of process parameters on the bead width..... 92
4.4.2.6. Effect of process parameters on the depth of penetration..... 94
4.4.2.7. Effect of process parameters on the ultimate tensile strength (UTS)..... 96
4.4.2.8. Effect of process parameters on the elongation..... 98
4.4.3. Multi-objective Optimization..... 100
4.5. Conclusions..... 101

Chapter 5: *Comparison of Molten Pool Behaviour of Different Numerical Models (CFD) and validation with experimental study* 103

5.1. Introduction…… 104
5.2. *Methodology*…… 105
5.2.1. N*umerical modeling*…… 105
5.2.2. Experimental setup…… 113
5.3. Results and Discussion…… 115
5.3.1. Temperature Iso-surfaces and Heat flux Vectors in the Molten pool…… 115
5.3.2. Width of the weld…… 116
5.3.3. Depth of the weld…… 117
5.3.4. Volume of the molten pool…… 118
5.3.5. Keyhole formation…… 120
5.3.6. Velocity field in the molten pool…… 121
5.3.7. Comparison of experimental results with all simulation models (CFD, Anisotropic, Isotropic) …… 124
5.4. Conclusion…… 125

Chapter 6: *General Conclusions and Future Scope* 127

6.1 General Conclusions…… 128
6.2 Future Scope…… 130

Bibliography…… *131*
Publication from the thesis……*138*

Nomenclature and Abbreviations

Nomenclature

A	Absorption coefficient
C_P, $C_P(T)$	Specific heat, J/kg.K
$C_{P\ solidus}$	Specific heat at solidus temperature, J/kg.K
$C_{P\ liquidus}$	Specific heat at liquidus temperature, J/kg.K
C_P^{app}	Apparent specific heat
Q_v	Volumetric heat source, W/m^3
a,b	Beam diameter, mm
d	Thickness of material, mm
E	Young's modulus, GPa
h	Heat transfer coefficient, W/m^2K
k, k (T), k_{xx}, k_{yy}, k_{zz},	Thermal conductivities, W/m.K
$k_{solidus}$	Thermal conductivity at solidus temperature, W/m.K
$k_{liquidus}$	Thermal conductivity at liquidus temperature, W/m.K
L_f	Latent heat of fusion, kJ/kg
P	Laser power, W
q_{conv}	Heat loss by convection per unit area, W/m2
q_{rad}	Heat loss by radiation per unit area, W/m2
Q	Heat flux of the laser beam, W/m2
r	Distance from center of laser beam, m
t	Time, s
T_m	Sheet metal surface temperature, K
T_s	Solidus temperature, K
T_l	Liquidus temperature, K
T_0	Ambient temperature, K
α (T)	phase transition function
T_{max}	Maximum Temperature, K
x_1, x_2 ,....x_n	Independent parameters
y	Response
V	Scanning speed, mm/s

Greek Symbols

ρ, $\rho(T)$	Material density, kg/m3
$\rho_{solidus}$	Density at solidus temperature, kg/m3
$\rho_{liquidus}$	Density at liquidus temperature, kg/m3
σ	Stefan Boltzmann constant, W/m^2K^4
Ɛ	Material emissivity

Operator

ΔT ΔTm	Temperature difference, K

Abbreviation

ANOVA	Analysis of Variance
LBW	Laser Beam Welding
LBM	Laser Beam Machining
TIG	Tungsten Inert Gas
MIG	Metal Inert Gas
Al	Aluminium
Cu	Copper
DSS	Duplex Stainless Steel
AISI	American Iron and Steel Institute
Ti-6Al-4V	α–β titanium alloy that exhibits high strength, low density, and good corrosion resistance
NiTi	Nitinol, an alloy with a near-equiatomic composition (i.e., 49%–51%) of nickel and titanium.
DP	Dual Phase
BW	Bead Width
DOP	Depth of penetration
HAZ	Heat Affected Zone
DOE	Design of Experiment
FEA	Finite Element Analysis
FEM	Finite Element Method
CFD	Computational Fluid Dynamics

Nd	Neodymium
Nd:YAG	Neodymium-doped Yttrium Aluminium Garnet
PRESS	Predicted Residual Error of Sum of Square
RSM	Response Surface Methodology

List of Figures

Figure 1.1	Schematic diagram of laser welding	2
Figure 1.2	Different kinds of weld joint: a) butt joint, b) lap joint, c) T-joint	3
Figure 1.3	Conduction mode welding	5
Figure 1.4	Transition mode welding	6
Figure 1.5	Keyhole / Penetration mode welding	7
Figure.2.1	Schematic geometry of the symmetrical sample	23
Figure.2.2	Mesh pattern used for discretizing the geometry	24
Figure 2.3 (a, b)	Justification of Weld geometry of bead cross section surface: (a) Present Simulation Study, (b) Experimental study of Batahgy *et al*.	27
Figure 2.4 (a, b)	a) Maximum temperature along the weld line and (b) Spot weld geometry of top surface when the laser beam is at middle of the plate (t=0.8s) (laser power = 500W, welding speed = 750 mm/min, beam diameter = 1 mm, plate thickness = 1.5 mm)	30
Figure 2.5	Temperature distribution at four instances: (a) beam is at the beginning, (b) beam is at the middle, (c)beam is at the farthest edge, (c) after cooling (laser power = 500W, welding speed = 750 mm/min, beam diameter = 1 mm, plate thickness = 1.5 mm)	31

Figure.2.6	Temperature distribution with time for different laser powers, beam diameters and welding speeds on the upper surface of the plate at the middle (10 mm) along weld line	33
Figure.2.7	Maximum Temperature at the top surface of material with distance along weld line for different laser powers, beam diameters and welding speeds	36
Figure 2.8	Effect of (a) Laser power, (b) Beam diameter and (c) Welding speed on Bead width and Depth of penetration of welded material	37
Figure 2.9	Effect of (a) Power, (b) Welding speed and (c) Beam diameter on Maximum temperature values of the top surface	38
Figure 2.10 (a-c)	Contours and response surface plots showing the effects of input parameters on the bead width	42
Figure 2.11 (a-c)	Contours and response surface plot show the effects of input parameters on the depth of penetration	46
Figure 2.12 (a-c)	Contours and response surface plot show the effects of input parameters on the Maximum temperature	49
Figure 3.1 (a, b)	(a) One half of the symmetrical sample, (b) Finite element mesh used for modelling	56
Figure 3.2	Experimental set-up for laser welding	59

Figure 3.3	Base material microstructure	61
Figure 3.4 (a, b)	Tensile test result performed for basic material (a) stress-strain curve, (b) sample of basic material	62
Figure 3.5	Micro hardness of base material	62
Figure 3.6	Simulated temperature contour and distributions for different scanning speed	63
Figure 3.7 (a-c)	Optical micrographs of all welded samples: (a) Weld-HAZ-Base junction, (b) Weld zone (higher magnification) and (c) Fusion zone	67
Figure 3.8 (a, b)	SEM micrographs of all welded samples: (a) Full welding, (b) HAZ zone	69
Figure 3.9	Tensile stress-strain curve of the welded samples	71
Figure 3.10	Photographs of samples used for the tensile testing	72
Figure 3.11	Micro Hardness from weld centre to base for four numbers of experiments	74
Figure 3.12	X-ray Diffraction pattern of all weld samples	75
Figure 4.1	Schematic diagram of the laser butt welding process	79
Figure 4.2	Experimental set-up for laser welding	79

Figure 4.3	Mounted samples for microstructural inspection after welding	80
Figure 4.4	Experimental set up of INSTRON- 8801 for tensile test	80
Figure 4.5 (a, b)	Tensile test sample (a) Dimensions (in mm) as per ASTM E8 standard, (b) Actual view of welded sample	81
Figure 4.6 (a, b)	Base material microstructure: (a) optical micrograph image, (b) SEM micrograph image	83
Figure 4.7	Stress-strain curve of the base material	84
Figure 4.8	Optical micrograph of welded sample (Laser power = 450 W, pulse width = 4.8 ms, scanning speed = 4.5 mm/s)	85
Figure 4.9	Measurement of bead width and depth of penetration using Image J software (Laser power = 450 W, pulse width = 4.8 ms, scanning speed = 4.5 mm/s)	86
Figure 4.10 (a-d)	Stress-strain curve of all the welded samples	86
Figure 4.11 (a-d)	Plot of predicted vs. actual response of (a) bead width, (b) depth of penetration, (c) ultimate tensile strength, and (d) elongation	92
Figures 4.12 (a-f)	Contours and 3-D response surface plots showing the effects of input parameters on the bead width	94

Figures 4.13 (a-f)	Contours and response surface plot show the effects of input parameters on the depth of penetration	96
Figures 4.14 (a-f)	Contours and response surface plot show the effects of input parameters on the ultimate tensile strength	98
Figures 4.15 (a-f)	Contours and response surface plot show the effects of input parameters on the elongation	100
Figure 5.1	Computational domain and boundary conditions used in the present model	108
Figure 5.2	A defined pulse profile over time	109
Figure 5.3	Time step variation during the events	109
Figure 5.4	Normalised temperature-dependent material properties of 2205 DP stainless steel	111
Figure 5.5	Scheme of phenomena in laser welding	114
Figure 5.6	Nd:YAG laser machine setup for laser welding	114
Figure 5.7	Contours of temperature and total heat flux vectors in the molten pool	115
Figure 5.8	Comparison of the numerically obtained weld width with experiment	117

Figure 5.9 Comparison of the numerically obtained weld depth with experiment 118

Figure 5.10 Comparison of the numerically obtained volume of the molten pool 119

Figure 5.11 Volume of the molten pool for three models 120

Figure 5.12 Comparison of the numerically obtained keyhole 121

Figure 5.13 Comparison of the numerically obtained velocity magnitude distribution 123

Figure 5.14 Numerically calculated Marangoni numbers 123

Figure 5.15 Numerically calculated Grashof numbers 123

Figure 5.16 Comparison of the numerically obtained weld depth with experiment: (a) Isotropic model vs experimental result, (b) Anisotropic model vs experimental result, (c) CFD model vs experimental result 125

List of Tables

Table 2.1	Physical parameters and their units	23
Table 2.2	Temperature dependent thermal properties of 2205 Duplex stainless steel	24
Table 2.3	Validation of Response parameter with **Batahgy** *et al.*	27
Table 2.4	Validation of Response parameters with Shanmugam *et al.*	27
Table 2.5	Process parameters and their units and limits	29
Table 2.6	Design layout and numerically calculated responses	29
Table 2.7	ANOVA for Response Surface Quadratic Model of Bead Width	40
Table 2.8	ANOVA for Response Surface Quadratic Model OF Depth of penetration	43
Table 2.9	ANOVA for Response Surface Quadratic Model OF Maximum Temperature	46
Table 2.10	Criteria of numerical optimization	50
Table 2.11	Optimal welding condition based on the criterion	50
Table 3.1	Physical parameters and their units	56
Table 3.2	Temperature dependent thermal properties of 2205 Duplex stainless steel	56
Table 3.3	Technical specifications of JK-600 HP Nd: YAG Laser	60
Table 3.4	Parameters considered for experimental investigations	60
Table 3.5	Chemical composition of base material 2205 duplex stainless steel	61
Table 3.6	Variation of overlapping factor, depth of penetration and bead width for different welding speed	65
Table 3.7	Laser input parameters and the validation of weld bead dimensions	70
Table 3.8	Laser input parameters and the experimental results of mechanical properties of the welded sample	71
Table 4.1	Process parameters and their units and limits	82
Table 4.2	Design matrix with experimentally calculated responses	82

Table 4.3	Mechanical properties of the base material	83
Table 4.4	ANOVA for response surface quadratic model of bead width	87
Table 4.5	ANOVA for response surface quadratic model of depth of penetration	88
Table 4.6	ANOVA for response surface quadratic model of ultimate tensile strength	90
Table 4.7	ANOVA for response surface quadratic model of elongation	91
Table 4.8	Criteria of numerical optimization	101
Table 4.9	Optimal welding condition based on the criterion	101
Table 5.1	Laser, geometric and material properties used in the simulations	110
Table 5.2	Solved governing equations and boundary conditions used in the model	111
Table 5.3	Comparison of experimental and simulation results for width of the weld	117
Table 5.4	Performance of the computational domains	124
Table 5.5	Comparison of experimental, CFD model simulation, Anisotropic model simulation and Isotropic model simulation results for Bead width of the weld	124
Table 5.6	Comparison of experimental, CFD model simulation, Anisotropic model simulation and Isotropic model simulation results for Depth of penetration of the weld	124

CHAPTER 1

Introduction to LASER, Explanation of proposed work and Literature survey

1.1. Introduction

A focused stream of coherent, monochromatic energy imposing at the junction generates heat resulting in amalgamation of the components during a technique of joining is classified as laser beam welding (LBW). The illumination from the laser is concentrated on extremely narrow area in order to have superior energy intensity, over those components being worked on during the LBM procedure employing ether reflecting focal equipment or lens after being transmitted via convex ocular devices, like reflectors. This acts as a non-contact approach so; zero compression needs to be used. In order to avoid molten pool from oxidizing, inert gas shielding can be utilized and metallic fillers are infrequently utilized in Laser beam welding process. The neodymium (Nd) atom as well as molecular CO_2 respectively, serve as the key components that are often utilized in both types of lasers, those are Nd:YAG laser and CO_2 laser, that have been most regularly applied to manufacturing preparation and welding jobs. The schematic for laser welding is shown in Figure 1.1.

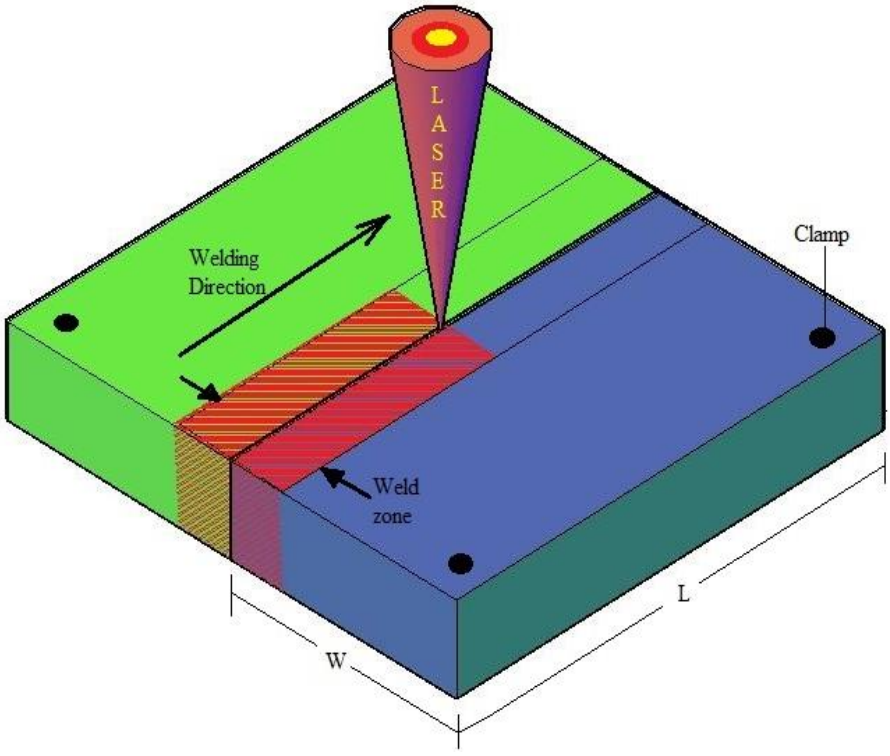

Figure 1.1 Schematic diagram of laser welding

Quite a few kinds of laser welding joints are available to bring both materials organized to join like; butt joint, lap joint, T-joint etc. Figure 1.2 shows the different joints which are used in many industries.

1.1.1. Butt Joint

The components join together along their edges forming a co-planar surface during butt welding. If the components are joined properly inside the depth in the base material, fully penetrated butt welds take place. That is achievable to complete welding penetration on thin pieces. Boundary pretreatment is often needed with more opaque pieces to acquire satisfactory welding.

1.1.2. Lap Joint

The lap joint is made up with a pair of components that overlap with each other. The individual pieces are welded together after being overlapped to create this. Single transverse, double transverse, or parallel fillet joints are the three possible configurations.

1.1.3. T-Joint

In a T-joint, each part forms roughly a letter shaped "T" with another joint, at right angle. Once both components cross over 90 degrees, the sides of the surface or component's centroid are brought alongside one another, creating a T-shaped connection. T-Joints have been created when a pipe or tube is welded to a base structure which is classified as some kind of fillet weld. To guarantee adequate permeation beneath the weld's surface, additional attention must be taken.

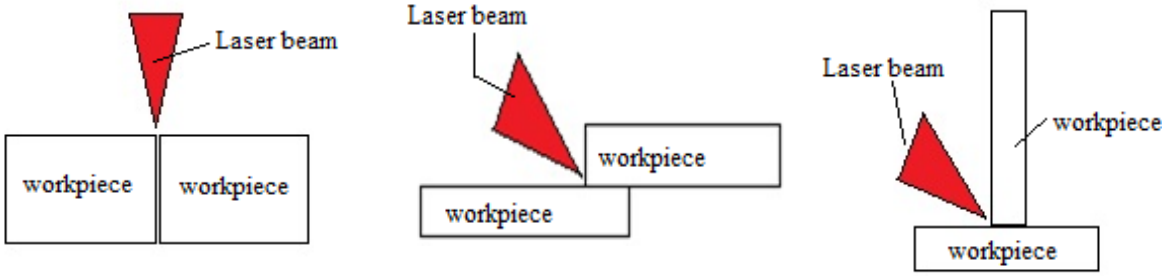

Figure 1.2 Different kinds of weld joint: a) butt joint, b) lap joint, c) T-joint.

Laser welding method is preferred over other conventional welding techniques due to some beneficial properties of the laser beam as well as laser welding process. The relative advantages and limitations of Laser welding process are discussed below:

1.1.4. Advantages of Laser Welding

A number of advantages over TIG, MIG, and spot welding are provided by the laser beam's ability to be controlled precisely.

1. The laser weld has a greater tenacity as well as a good depth-to-width ratio since it forms narrower width.

2. Limitation of the heat-affected zone and fast cooldown prevent annealing of the adjacent substance.

3. Carbon steel, high-strength steel, stainless steel, titanium, aluminum, and high-value alloys along with diverse components can all be satisfactorily welded together by lasers.

4. Precise micro-welding of tiny elements is possible due to the laser's narrow and precisely regulated output.

5. It causes minimum shrinkage or distortion of the components.

6. There exist no direct interaction among the substance with the laser head.

7. Laser welding, which requires accessibility to a single direction, may substitute spot welding.

8.The amount of trash created by laser welding is manageable yet minimal.

1.1.5. Restrictions of the Laser Welding Process

1. It’s necessary to precisely place junctions beneath the beam and in relation to the beam's focus point.

2. The weld joints are mechanically clamped; it is imperative to guarantee that the joint's ultimate location aligns precisely with the spot where the beam impinges.

3. The highest joint thickness that a laser beam may weld is considerably constrained. It is therefore challenging to weld through weld penetrations bigger than 19 mm.

4. Materials having high heat conductivity and reflectivity, such as Al and Cu alloys, may not be as easily welded with lasers.

5. When performing moderate to high power laser welding, it is necessary to use a suitable plasma control equipment to assure the reproducibility of the weld.

6. The energy conversion efficiency of lasers is often low, typically less than 10%.

7. Because of the LBM's quick solidification properties, some weld porosity and brittleness are to be expected.

1.1.6. Modes of Laser Welding

A high-power density source, the laser beam offers a special welding ability that maximizes penetration while requiring the least amount of heat input. The material is heated by the powerful laser beam quickly, usually in milliseconds, forming the weld. According to the power density inside the focus spot size, there are three different sorts of welds: penetration/keyhole mode, transition mode, and conduction mode.

1.1.6.1. Conduction mode

The process of conduction mode welding produces a broad but minimal depth weld nugget at low energy densities, usually 0.5 MW/cm^2. Heat from the irradiated surface conduction provides the heat needed to generate the weld into the substance. When there is a possibility of particle infiltration, as in some battery sealing applications, or when an aesthetically pleasing weld is required, this can generally be utilized. Figure 1.3 displays the conduction mode welding schematic diagram.

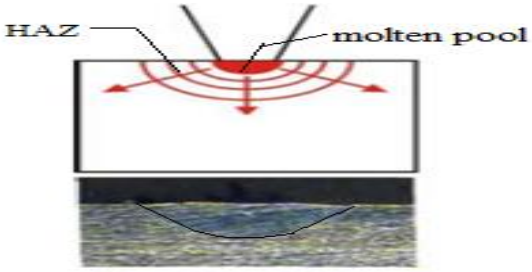

Figure 1.3 Conduction mode welding

1.1.6.2. Transition mode

By virtue of the formation of the "keyhole," transition mode, which happens at a medium power density of around 1 MW/cm^2, allows for more penetration than conduction mode. A vapor pressure sustains the keyhole's diameter, which is significantly less than the weld width, resisting the pulling power of the adjacent molten matter. The keyhole is a column of vaporized metal that penetrates into the substance. Time and power density govern how deep the keyhole goes into the substance. The keyhole serves as a channel to transfer laser power into the substance because of its low optical density. The schematic diagram for transition mode welding is displayed in Figure 1.4.

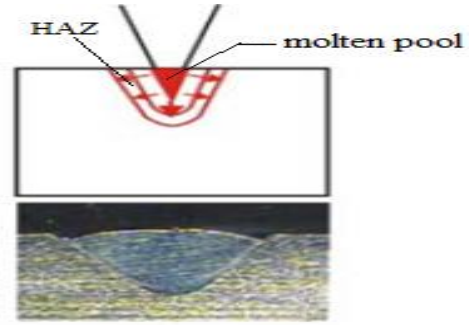

Figure 1.4 Transition mode welding

Conduction welding can be conceptualized as a point source of heating from the surface, but the keyhole offers a more efficient welding source by acting as a line source of heating from within the metal. In transition mode, the time or power density is just enough to start a keyhole in the part, but not to get very far into it. With a normal weld aspect ratio (depth/width) of approximately 1, the welds show shallow penetration as a result. Pulsed Nd: YAG and fiber lasers are the only sources of this type of welding employed in numerous spot and low heat input seam welding applications.

1.1.6.3. Keyhole or penetration mode

The weld transitions to keyhole mode, which is characterized by deep narrow welds with an aspect ratio larger than 1.5, when the peak power density is increased beyond 1.5MW/cm^2. When the peak power density exceeds 1 MW/cm^2, the penetration depth grows quickly, switching the weld mode from conduction to keyhole/penetration welding.

The narrow welds found in penetration or keyhole mode welding typify the process. By delivering laser power directly into the material, component distortion and the heat-affected zone are reduced while weld depth is maximized and heat input is minimized. Either extremely high speeds (over 500 mm or 20 inches per second) with small penetration (usually less than 0.5 mm or 0.02 inch) or lower speeds (deep penetration up to 12 mm or 0.5 inch) can be used to perform the weld in this keyhole mode. Figure 1.5 shows the schematic diagram of keyhole / penetration mode welding.

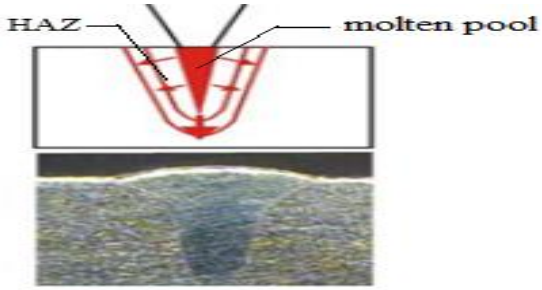

Figure 1.5 Keyhole / Penetration mode welding

1.2. Proposed Research Work

Considering relative advantages and limitation of different modes of laser welding, keyhole mode welding against other modes of welding is more desirable to acquire complete welding. The present work proposes to explore laser welding of duplex 2205 stainless steel through numerical and experimental methods for optimization of process parameters. Laser welding can be accomplished with comparatively lesser amount of heat and the heat can be delivered through a smaller and precise beam resulting in less residual deformation and a deeper penetration which helps in achieving a higher weld strength, a smaller bead width with better aesthetics, as well as a narrow heat affected zone (HAZ) such that lesser amount is affected due to thermal degradation process. Such advantages of laser welding offer a promising route for welding compared to other welding techniques. Selection of 2205 duplex stainless steel is because its unique properties which should be explored much. The family of stainless steels known as duplex stainless steels (DSS) has a dual microstructure made up of roughly equivalent amounts of austenite and ferrite phases. This microstructure maintains equilibrium and provides an excellent amount of mechanical strength and ductility along with corrosion resistance, rendering DSS a popular choice for pipelines, handling high pressure and corrosive fluids. Besides, mechanical and chemical properties are being stable in elevated temperature. As it is predictable to reach very high temperature in welding process, the consistency of properties on such high heat is desirable. Application of the Duplex stainless-steel finds use in diverse fields, such as automotive industries, process industries, aerospace, marine and fabrication industries.

Laser welding process requires to control some process parameters to achieve some response parameters. It is known that a welding will be defined as satisfactory or acceptable only if it can offer quite high strength in joints. To ensure higher strength in joints we have to aim

maximum penetration of heat into the material as well as minimum bead width so that heat affected zone can be minimal. A large area of heat affected zone can rise brittleness of weld materials. Higher strength weld joints require precise selection range of input or process parameters. Laser power, welding speed, beam diameter and pulse width are generally applied as laser welding process parameters where depth of penetration, bead width, ultimate tensile strength, yield strength, elongation and young's modulus are required response parameters to identify the quality of welding. So, for accruing high quality strength joints we have to identify optimum process parameters. In experimental way if we try to recognize this optimum range then we have to complete a very large number of experiments which will be very expensive and time consuming as well. Due to this reason in present research, it is planned to develop a three-dimensional finite element model for laser welding simulation results from which will be compared with experimental results and then process parameters will be optimized using both the experimental and simulated results.

At first, an isotropic model for laser welding is developed including phase change with physical and temperature dependent thermal properties of material. Applied power, welding speed and beam diameter are given as input. Symmetry was maintained throughout the surface of the welding orientation. In order to choose the right quantity of components, a series of convergence trials were carried out, paying special attention to the depth axis along with regions adjacent to the weld alignment. Extremely condensed mesh was produced around the area close to the weld line, and coarse mesh was proposed around the left-over area. For assessing the quality of weld, it is restricted to consider only the depth of penetration, bead width and temperature distribution as obtained from the simulation model. Assessment based on Mechanical characterization is not possible from the model. Then those outputs are validated with published results to check its adequacy and it is observed that this method provides acceptable match though not exactly identical. Now based on this process we simulated quite a large number of welding to get a safe operating window and optimum process parameters, based on which we can go ahead for experimental investigation. But in actual, thermal properties are not consistent with elevated temperature in each direction, so isotropic simulation process needs to upgrade into anisotropic process. To overcome the limitation anisotropic approach is implemented in simulation model and compared with experimental observations.

As stated above that only depth of penetration and bead width can be measured from model, so we compared these two responses and found better match against isotropic model. With the help of optical microscope, we measured depth and width of fusion zone, additionally we identified the heat affected zone. For better realization of weld, base and HAZ zone we utilized scanning electron microscope, from where we understood the grain orientation and grain size variations at different zone. Welding quality can not be only defined by depth of penetration and bead width but it also needs to ensure required mechanical properties. So, we decided to go for mechanical characterization of those few welded sample along with base metal by doing tensile test and hardness test. Here we noticed that hardness is very high at weld zone where after welding base zone hardness remain unchanged regarding base metal and HAZ has very low hardness value. But for tensile test we found that base material offers higher ultimate tensile strength and elongation than welded materials. So, a clear mechanical property degradation was noticed.

Only depth of penetration and bead width are not sufficient at all to provide good quality weld until it offers satisfactory strength. So still there are some requirements to upgrade the present simulation model. So far for both simulation process we only consider isotropic and anisotropic approach but it is obvious to consider fluid flow as in reality there is a situation molten metals flows, so to achieve accurate simulation it is required to include the CFD in finite element method. Three numerical models are developed considering the flow in the molten pool to be laminar in the first model and turbulent in the two other models. We obtained depth of penetration and bead width from these three CFD model and compared with experimented one. We found a turbulent model provide best match to the experimental results so far against isotropic and anisotropic model. Although we were still unable to find the strength of joints from this CFD model so we decided to carry out a bunch of experimental welding investigation to check depth of penetration, bead width along with ultimate tensile strength and elongation taken into account. And depending on the experimental result we create a design matrix to analyse response parameters by developing mathematical corelation between process and response parameters to predict future responses with another set of process parameters. Also, we upgrade the optimization model taking into account depth of penetration, bead width along with ultimate tensile strength and elongation and found optimum process parameters which can deliver maximum ultimate strength and elongation with maximum penetration and minimum bead width. Considering weld response

parameters like depth of penetration, bead width along with mechanical properties like ultimate tensile strength and elongation is appraisable to identify the optimum weld conditions under laser welding process.

1.3. Brief Literature Survey

A number of attempts have been made to simulate laser welding process using numerical methods and experimental study with design of experiments (DOE) techniques. Sathiya *et al.* [1] described an investigation conducted on the process of 3.5 kW cooled slab laser welding, using various shielding gases, specifically argon, helium, and nitrogen, with a consistent flow rate, of 904 L super austenitic stainless steel. Mechanical characteristics were precise to achieve favourable responses such as bead width (BW), depth of penetration (DOP) and the tensile strength, to ensure good quality joints and Taguchi approach with grey relational analysis was employed as a statistical design of experiment (DOE) technique to optimize the welding conditions alongside in order to verify the improved variables in each case, affirmation tests also carried out.

Frewin and Scott [2] introduced a finite element model in three dimensions that depicts the heat flow during pulsed laser beam welding. These findings imply that the laser beam's energy distribution and absorptivity have a significant influence on the temperature profile and weld proportions. De *et al.* [3] offered a two-dimensional axisymmetric finite element study of the heat flow during laser spot welding, accounting for the latent heat of transformations and the temperature dependence of physical characteristics. They claim that an accurate estimation of the weld pool dimensions has been accomplished utilizing the established method. Benyounis and Olabi [4] furnished a thorough analysis of optimization methods for obtaining the geometry of the weld beads. Ming *et al.* [5] created a dynamic simulation of the temperature distribution during 304 stainless steel laser welding. Anawa and Olabi [6] optimized the welding pool of dissimilar laser welded components using Taguchi method. Their results indicate that the developed models can predict the fusion zone and shape satisfactorily. Abderrazak *et al.* [7] utilized both techniques such as experimental and finite volume method as a means of studying the thermal processes that occur during continuous laser keyhole welding. It has been discovered that the dimension and shape of the molten pool within the workpiece are influenced by welding parameters, such as laser power and welding speed. Belhadja *et al.* [8] developed employing a three-dimensional finite element model to replicate the thermal evolution of alloys based on magnesium using laser

beam welding. Moreover, they have conducted experimental studies to validate the results of numerical simulation and those are found to be in good agreement.

Abhilash and Sathiya [9] investigated effect of the laser power, welding speed and focal point position on bead geometry and proposed that FEM can be a useful technique for bead geometry prediction during laser welding at minimal heat input intensities. Batahgy *et al.* [10] examined the impact of laser process parameters on the duplex stainless steel's mechanical, corrosion, and fusion zone microstructure as well as dimension. The researchers have arrived at the conclusion that in order to achieve welded joints with mechanical and corrosion qualities that are suitable, it's necessary to optimize the laser power, welding speed, defocusing location, and kind of shielding gas composition. Kumar *et al.* [11] performed a numerical investigation on transient temperature profile of laser beam welding process of titanium alloy taking into account the entire double-ellipsoidal heat source model for the transient and stationary heat sources. It was noticed when beam power improves so does the maximum temperature in the fusion region. Furthermore, the laser beam's power has a significant impact on the of heat affected zone. Akbari *et al.* [12] compared both computational and experimental methods, the titanium alloy laser welding process is investigated to simulate the temperature distribution and forecast the heat-affected zone. They discovered that penetration depth rises at steady pulse length, pulse frequency, and pulse power for reduced welding speeds. Azizpour *et al.* [13] simulated laser welding process of Ti6Al4V 1.7 mm sheets in butt joint through finite element analysis to predict the temperature distribution, hardness and weld geometry. They observed that hardness at the center of the weld pool is maximum and higher laser speeds caused more variation in hardness between the weld pool and base metal. Kumar [14] developed a three-dimensional finite element model for AISI 316L stainless steel sheets that are 2 mm thick utilizing a pulsed laser beam employing COMSOL MULTIPHYSICS. For AISI 316L stainless steel sheets, they forecasted the highest and lowest temperatures that would occur throughout laser welding.

Acherjee *et al.* [15] looked into how carbon black affects the weld morphology and distribution of temperatures during laser transmission welding of polymers employing a transient numerical model by ANSYS that is based on conduction mode heat transfer. A reasonable level of agreement is revealed while they experimentally and numerically computed the weld pool dimensions results. The obtained results demonstrate that the

creation of the weld pool shape and the temperature field distribution are significantly influenced by the carbon black. Daha *et al.* [16] analysed the temperature field resulting from keyhole plasma arc welding (PAW) of 2205 duplex stainless steel and estimated the weld geometry using a three-dimensional thermal transient finite element model. Daneshkhah *et al.* [17] investigated the form of the molten pool and temperature field throughout laser keyhole welding employing a three-dimensional numerical model utilizing FLUENT software. To account for the latent heat during melting and solidification, the enthalpy-porosity approach was utilized. Marimuthu *et al.* [18] conducts a sequentially linked thermo-structural multiphase analysis with the aim of forecasting how laser settings would affect the weld bead's surface topological change and how that would affect the structural qualities that followed. Bannach [19] described that COMSOL Multiphysics and the Heat Transfer Module provide a customized platform that enables the use of the Apparent Heat Capacity method for representing phase transitions from solid to liquid, liquid to solid, or solid to solid. In every substance, a maximum of five phase changes are permitted. Shanmugam *et al.* [20] investigated how input variables affected the depth of penetration, bead width, length, and bead length in laser spot welding of 2.5 mm thick AISI 304 stainless steel sheet. The computational modeling outcomes, when validated against experimental findings that demonstrated good acceptance, forecast the form of the weld beads for various variations of laser process parameters. Utilizing design of experiments (DoE) and finite element analysis (FEA) methods, Acherjee *et al.* [21] conducted a methodical inquiry by executing sensitivity analysis into the laser transmission contour welding process to check the influence of various levels of a random parameter on a certain depending parameter. The book of Montgomery [22] delivers a brief knowledge about design of experiment, analysis procedures and about different experimental approaches along with statistical relationship among process and response parameters. Yang *et al.* [23] examined how welding heat inputs influenced the microstructure and corrosion characteristics of the heat-affected zone in 2205 duplex stainless steels. The researchers discovered that the expansion of intragranular, widmanstatten, and coarsening of grain boundary austenite all triggered an upsurge in the restructured austenite content, which improved lower-temperature toughness and had an impact on the corrosion phase. Pekkarinen *et al.* [24] objectively identified the microstructural alterations that ferritic and duplex stainless steels undergo when the welding conditions regulate the heat input without the use of shielding gas and also, they located and investigated microstructural

alterations in welds, employing optical metallographic techniques. Soltysiak [25] reported on the fatigue testing performed on duplex 2205 steel laser-welded butt joints along with base material using a Nd-YAG disk laser with no filler for two distinct welding parameters. The ideal laser welding parameters for fatigue life of duplex 2205 steel were determined based on the results of the testing. Yang *et al.* [26] used pulsed Nd:YAG laser welding to examine the characteristics and welding process of 2205 duplex stainless steel and defines welds underwent tests for tensile strength, surface microhardness, surface topography, and microstructures at varying welding speeds, input currents, pulse widths, frequencies, and defocus distances and demonstrated that the amount of ferrite and austenite in the welds was approximately the same and under certain conditions, the weldability was good. Soltysiak *et al.* [27] described fatigue tests on laser butt welded DUPLEX 2205 steel joints employing a Nd-YAG disk laser without filler for two welding conditions. Previous testing on weld joints, having a minimum of ten welding conditions, determined the parameters. The testing determined the best fatigue life conditions of laser welding DUPLEX 2205 steel. Hosseini *et al.* [28] examined how heat input and repeated welding cycles influenced the microstructure of the heat-affected zone when 2507 super duplex stainless steel was TIG welded. In a study conducted by Zhang et al. [29], the microstructure, impact toughness, and pitting corrosion resistance of duplex stainless steel welding joints made using fluxed cored arc welding and gas tungsten arc welding with various shielding gas compositions were examined. They have discovered that when plates are exposed to N2-supplemented shielding gas during the welding process, their impact toughness and pitting resistance enhance. The effect of heat input on mechanical properties such as microhardness, toughness, joint strength, and metallurgical and corrosion characterization of UNS S31803 duplex stainless steel in solid state continuous drive friction welding was investigated by Asif et al. [30]. They have noted that the welded samples do not contain any intermetallic phases. Moreover, toughness decreases with an increase in the heat input at room temperature. Micro hardness and Corrosion resistance increases with an increase in heat input. Capello *et al.* [31] studied the enhancement of laser weldability of a type 22Cr_ 5Ni_ 3Mo (UNS S32205) duplex steel. They have demonstrated that by an optimized choosing the post-weld surface treatment laser settings, it is possible to attain a good structural control of the weld bead microstructure. Safdar *et al*. [32] utilized Computational Modeling to evaluate the isotropic and anisotropic improved thermal conductivity techniques for laser melting of Inconel 718. Experimental

melt pool geometry has been comparable to modeling. Anisotropic enhanced thermal conductivity correlates closely to experimental results, while isotropic enhanced thermal conductivity cannot reliably estimate melt pool geometry. Badji *et al.* [33] examined the phase changes and mechanical behaviour of 2205 duplex stainless steel throughout welding and the annealing process. Mourada *et al.* [34] conducted a comparable analysis of the effects of carbon dioxide laser beam welding (LBW) and gas tungsten arc welding (GTAW) regarding the microstructure and size of the fusion zone, along with the mechanical and corrosion properties of 6.4 mm thick duplex stainless steel DSS grade 2205 plates. Mirshekari *et al.* [35] conducted comparison research on the laser welding of NiTi wire to AISI 304 austenitic stainless-steel wire alongside its own. According to the research's findings, the development of brittle intermetallic compounds in the weld zone throughout dissimilar laser welding of NiTi to AISI 304 leads in a considerable drop in tensile strength and ductility. Furthermore, researchers proposed for the enhancement of the joint characteristics necessitates an adequate modifying technique. Jia *et al.* [36] offered a thorough analysis of the dissimilar joints between the DP600 and DP980 using a focused and defocused fibre laser beam. The primary crucial factor in determining the penetration depth is the proportion of pulse energy to pulse duration, determined by Akman *et al.* [37] from their experimental study on laser welding of thick titanium alloy. Kashaev *et al.* [38] explored the joining techniques for Ti-6Al-4V butt joints and T-joints using a filler wire that is suitable with alloys. Moreover, they conducted further surveys examining the mechanical characteristics, microstructure, and weld morphology for achieving joints with regular shape, without visible cracks, pores and geometrical defects. According to their findings, base metal joints are less ductile with lower joint strength compared to butt and T-joints. Lei *et al.* [39] evaluated the mechanical and microstructure characteristics of the Ti-22Al-27Nb alloy laser beam welded joints. The findings demonstrate that ductility of joints reached 56% of the base metal, and the joint strength at room temperature is on par with those of the base metal. Adjacently, joint strength and ductility of weld joints at elevated temperature is not close to that of the base material. Shanmugarajan *et al.* [40] studied the effects of laser welding on 6 mm thick P92 material (Cr-Mo-W-V-Nb steel) on metallurgical characteristics following a three-hour post-weld heat treatment at 760 ^{0}C and on mechanical properties at ambient temperature and elevated temperatures. They have observed that good fusion with full penetration without any weld defect and no coarse-grained heat affected zone is formed.

Moreover, higher micro hardness is observed at fusion and heat affected zone than base material. Artinov *et al.* [41] presented a CFD modelling for the prediction of the 3-D transient temperature field for full-penetration keyhole laser welding considering the effect of thermo-capillary and natural convection. Bachmann *et al.* [42] created the computational framework for turbulent steady state in three dimensions, to examine the impact of a static magnetic field through incomplete penetration high power laser keyhole welding of thick aluminium substrates. According to their suggestion, the impact of Marangoni stresses at the upper surface is notably reduced by the produced magnetic drag element. Courtois *et al.* [43] developed a heat and fluid flow model to research the primary physical processes involved in the formation of the keyhole. In their model, they have analysed the velocity of fluid in the molten pool and its free surface deformation. Zhao *et al.* [44] studied the keyhole and molten pool behaviour such as development of keyhole and molten pool, oscillation of keyhole and molten pool, forces of interaction of fluid dynamics in the keyhole and molten pool and keyhole-induced porosities using their developed CFD model. They have found that the molten pool's depth stays constant while the keyhole height varies periodically during continuous laser welding. They observed that bubbles form at the bottom of the molten pool when the keyhole depth decreases suddenly, which is the main cause of porosity defect. Ai *et al.* [45] proposed a novel three-dimensional model considering all welding process phenomena to simulate the process of formation of the weld bead and predict its full size. They have clearly demonstrated because of the buoyancy force created by the temperature difference and recoil pressure in the back of the keyhole, the colliding fluid flow forms the weld strengthening. In their following work [46], they have investigated the features of the weld shapes in the fiber laser keyhole welding. The top surface of the weld is assumed as the flat surface; hence weld reinforcement is ignored in their model. Their results showed that suggested approach for fibre laser keyhole welding performs exceptionally well when it comes to weld bead attributes study. Kooa *et al.* [47] proposed a numerical model to understand the evolution of hourglass shaped melt pool during laser welding. Recoil pressure and melt surface tension are two factors which have been thought to be important in developing hourglass-shaped welds, as demonstrated by their ultimate weld morphologies. Gao *et al.* [48] developed a 3-D numerical model explore the change of the weld bead shape in high power laser welding while taking the fluctuating characteristics of the molten pool and keyhole into consideration. According to their suggestions, the key elements influencing

the alteration of the weld bead shape are the fluid flow, temperature field, and mechanical balance over the molten pool. Ramkumar *et al.* [49] discussed the electron beam welding (EBW) technique's capacity to weld 6 mm thick super-duplex stainless-steel plates. A thorough structure-property relationship study was performed as well using point and line mapping EDAX analysis throughout the weldment. Saravanan *et al.* [50] investigated the weldability of super duplex stainless steel UNS S32750 (SDSS) utilizing a 600W pulsed Nd:YAG laser welding system. The procedure was carried out by changing the welding speed while maintaining the same additional variables in order to adjust the heat input. Because of the increased ferritic phase in the weld zone, weld joints have superior Vickers microhardness and tensile strength compared to PWHT joints. Sato *et al.* [51] examined the mechanical characteristics and microstructure of SAF 2507 super duplex stainless steel that was friction stir (FS) welded. Utilizing a polycrystalline cubic boron nitride (PCBN) tool and friction stir welding (FSW), high-quality, full-penetration welds have been achieved in the super duplex stainless steel. The transverse tensile specimen, that was welded, disintegrated around close proximity of the retreated side's stir domain and TMAZ boundary because the weld's characteristics were similar to those of the base material. Luchtenberg *et al.* [52] examined the DSS weld overlaying characteristics that were acquired by coating a mild steel plate (ASTM A 516 Gr 60) with the duplex stainless steel alloy ER 2209. Pavan *et al.* [53] conducted a comprehensive investigation on the microstructure and mechanical behaviour of 11 mm thick type 316LN stainless steel joints that are welded using a combination of laser and metal inert gas. They found that the position of the laser and arc source have a significant impact on the depth of penetration, and that the mechanical properties of the weld joint are primarily affected by the δ-ferrite content, secondary dendrite arm spacing, and variation in zone-wise micro-segregation. Karimi *et al*. [54] studied the effects of fiber laser welding parameters determined by the reactions of the melt pool's hardness, depth, microstructure, temperature, and tensile strength. The highest tensile strength of 500 MPa and 18% elongation are attained at the laser power of 400 W, welding speed of 300 mm/min at the focus point. Researchers concluded as the most significant influences on the tensile strength of the weld are the scanning speed and absorbent power of the laser. Madhankumar *et al.* [55] focused on the effects of process parameters on the ultimate tensile strength of dissimilar metals, specifically Inconel 718 alloy and duplex 2205 stainless steel. They found that the laser power is the most prominent factor affecting the output response of the ultimate tensile

strength, followed by the focal location and welding speed. Ahmad *et al.* [56] performed Ytterbium fiber laser welding on superalloy Inconel 625 and duplex stainless steel 2205 at different heat inputs. They discovered that heat input is a highly influential parameter affecting the bead shape, with higher energy input resulting in top glass shape and X-shape bead, and lower energy input resulting in V-shape bead formation. Kose and Topal [57] investigated the impact of heat input and post-weld heat treatment over mechanical, surface, texture, and microstructure characteristics. They discovered that toughness values rose but tensile strength, hardness, and bending force in the welded samples dropped with increasing heat input. Mansur *et al.* [58] studied the applicability of laser welding in dual phase 600 steel sheets and examined the mechanical properties of the welded sample through metallographic analysis, microhardness, tensile tests, and erichsen cupping tests. Kumar and Sinha [59] focused on the effects of heat input on weld bead shape, fusion zone width, heat-affected zone width, and fusion zone area, and found that an increase in heat input resulted in an increase in fusion zone area, fusion zone width, HAZ width, and the size of micropores, while the average microhardness of the fusion zone decreased. Ahmad *et al.* [60] studied the effects of the process parameters on molten weld-pool lifetime and cooling rate, as well as the influence of cooling rate on hardness and tensile strength of Inconel 625 and 2205 duplex steel. Benyounis *et al.* [61] explored AISI304 laser welded butt joints for their tensile and impact strength as well as their joint operating cost utilizing Design-expert application to create the design matrix, analyse the experimental data along with optimization of the welding procedure. Sunny *et al.* [62] In this respect, the goal of the investigation is to determine the ideal set of input process parameters for using A-TIG welding to create 10 mm thick junctions between SASS AISI 904L plates using bead on plate welding experiments. Sun *et al.* [63] addressed the optimization of laser-MAG hybrid welding parameters for ship steel with 10CrNi3MoV content utilizing the Box-Behnken Design (BBD) model inside Response Surface Methodology (RSM). Heydari *et al.* [64] focused on laser welding of Ti6Al4V alloy sheets, having a thickness of 3 mm, which were all subjected to rigorous investigation for tensile strength, elongation, and temperature field of the fusion zone, on the impact of input variables and to create multiple regression models, the laser welding experiments were carried out using the RSM approach and central composite design. Cheepu *et al.* [65] examined the fusion zone width, penetration, heat affected zone width, and strength of the titanium alloy welds through the laser welding procedure. RSM approach is

implemented for the experimental design for creating regression equations. The outcomes of the RSM technique were verified by comparing them with the findings of the experiment. Chellu *et al.* [66] aimed to achieve a high-quality butt joint on 2.5-mm thick 304 grade stainless steel in the current research. Torabi and Kolahan [67] employed the Central Composite Design matrix in Response Surface Methodology (RSM) to simulate and optimize the process, fully replicating thirty-one trials. This was carried out using experimental data from pulsed laser welding of thin AISI316L austenitic stainless-steel sheets, during which Ultimate Tensile Strength (UTS) was measured to be the primary characteristics for a superior laser welding. According to the numerical outcomes, it is evident that the suggested simulation and optimization approaches work pretty effectively regarding the pulsed laser welding method. Joyce et al. [68] demonstrated a computational modelling employing COMSOL Multiphysics on a carbon black loaded PMMA (polymethyl-methacrylate) for transient heat transfer and thermochemical impairment realization in an IR opaque component. At the evaporation temperature, they suitably adjusted the thermal conductivity and density of PMMA to record the disposal substance due to evaporation. Metais et al. [69] attempted to analyze substance interaction throughout laser welding both experimentally and numerically. In order to enhance comprehension of the convection-diffusion process-based materials integrating in fully penetrated laser welding, a three-dimensional simulation of heat, mass, and fluid flow has been carried out to generate a diagram of the component's arrangement and the geometry of the fusion zone.

It is found from literature survey that not much work has been done in the area of laser welding of duplex stainless steel for different types of joints. Survey of the state of the art also reveals that numerical simulation of laser welding of DSS has not been seen so far. Numerical simulation of laser welding process is planned in the proposed work since it will help us to explore the physics of the process to gain a better insight. Besides, since the numerical tool is a cheaper alternative compared to experiments, it will help us to generate a huge volume of data based on which we shall be able to develop reliable and accurate mathematical relations to predict optimized process conditions. The optimized process conditions, thus generated is planned to be validated with limited number of experiments requiring less time and cost.

1.4. Objectives of Present research work

The present work proposes to

1. Explore laser butt welding of duplex 2205 stainless steel through experimental and numerical methods for optimization of process parameters.
2. Develop a three-dimensional numerical model using finite element method, considering phase change through COMSOL MULTIPHYSICS and validated with initially by published then inhouse experimental work.
3. Study the effects of Laser weld process parameters and geometric parameters on temperature distribution at weld zone and bead geometry (depth of penetration and width).
4. Development of mathematical model based on simulation results to predict response parameters by using response surface methodology.
5. Optimization of process parameters based on multi-objective criteria.
6. Evaluation of mechanical properties (ultimate strength and elongation) by experiments for welded joint with different laser weld inputs and to establish a functional relationship between input and output along with optimization using Response surface methodology.
7. Characterizing the strength of joints and the formation of bead geometry for post processing of the experimental coupons.

Research Project Flowchart

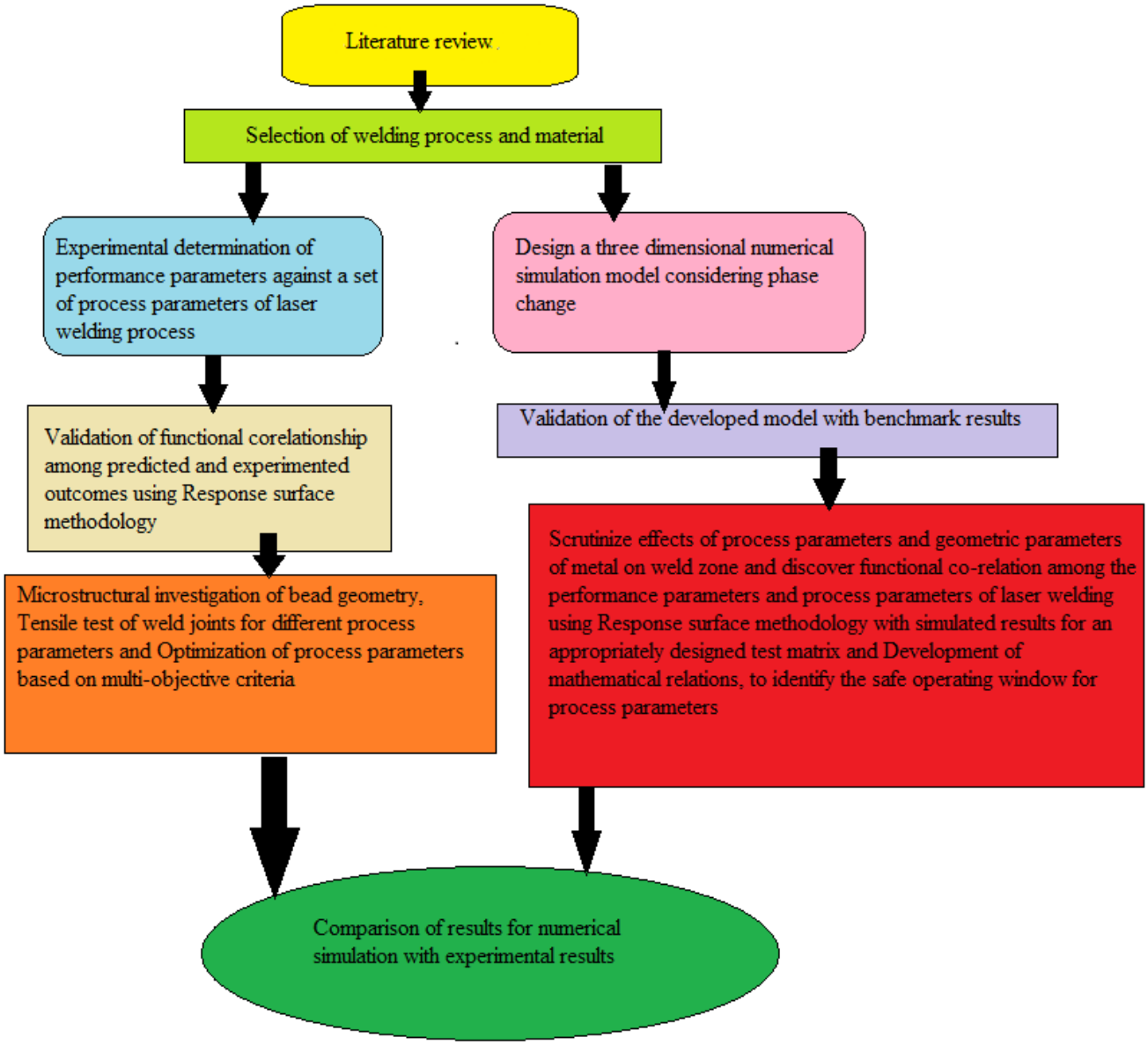

CHAPTER 2

Finite Element Simulation of Laser butt Welding of 2205 Duplex stainless steel (isotropic)

Chapter 2

2.1. Introduction

The present study deals with laser welding of duplex 2205 stainless steel considering phase change, for butt joint developing three-dimensional modelling by finite element method using COMSOL MULTIPHYSICS. At first, we model the system with isotropic approach and followed conduction welding method. The temperature distribution can be obtained from the heat conduction equation for a particular amount of power, welding speed, beam diameter and material thickness of this particular material. Due to the nonlinearities involved, analytical solution is ruled out. During the welding procedure applied energy or heat makes a solid to liquid transition in metal, taking this into account a phase transition function is involved in governing equations. Using temperature dependent properties such as thermal conductivity and specific heat capacity along with latent heat we incorporate the phase change. The depth of penetration and bead width in weld zone are measured as response parameters. We also identified the maximum temperature on weld line as output. The limitation of this model is the inability of mechanical characterizations but based on the theory that full penetration or maximum penetration can provide higher strength in weld joints and lower bead width includes narrower heat affected zone resulting in better weld quality, it is possible to found a safe operating window for this process. The results obtained from FE simulated welded joint are compared with results available with published papers. After a convincing match we used that model to design a bunch of simulation and made a design matrix to find out the optimum range of process parameters. A statistical technique is applied to develop a mathematical model among process parameters such as, power, welding speed and beam diameter, based on simulation results to predict response parameters such as, bead width, depth of penetration and maximum temperature. Considering multi-objective criterion optimization of process parameters were done.

2.2. Finite Element Modeling

In order to evaluate the impacts of the procedure variables on the temperature gradient and bead geometry developed through laser butt welding, we performed a three-dimensional numerical simulation incorporating the finite element method. Schematic representation of the geometry is shown in Figure 2.1 and Figure 2.2 shows the mesh pattern that is used for discretizing the model. Input factors for the simulation of laser welding include laser power, welding speed, and beam diameter, whereas response factors include bead width, depth of penetration, and maximum temperature.

2205 Duplex stainless steel sheets, each sized 100×20×1.5 mm, were chosen for laser welding simulation process and carried out by using COMSOL 4.2a software with moving energy origin in different velocities throughout the joining edge. In case of building the model some physical parameters are used that are given in following Table 2.1.

Table 2.1 Physical parameters and their units [16]

Material Property	**Symbol**	**Value**	**Unit**
Ambient Temperature	T_0	300	K
Solidus Temperature	T_S	1658	K
Liquidus Temperature	T_L	1773	K
Latent heat of fusion	L_f	500	kJ/kg
Emissivity	ε	0.7	
Heat transfer coefficient	h	10	W/m^2K

Specific heat and thermal conductivity are two temperature-dependent thermal parameters that define a material's temperature response. Table 2.2 presents the temperature dependent physical properties of 2205 Duplex stainless steel those are used for the present FE simulation [16]. Density of the material is taken as 7860 kg/m^3.

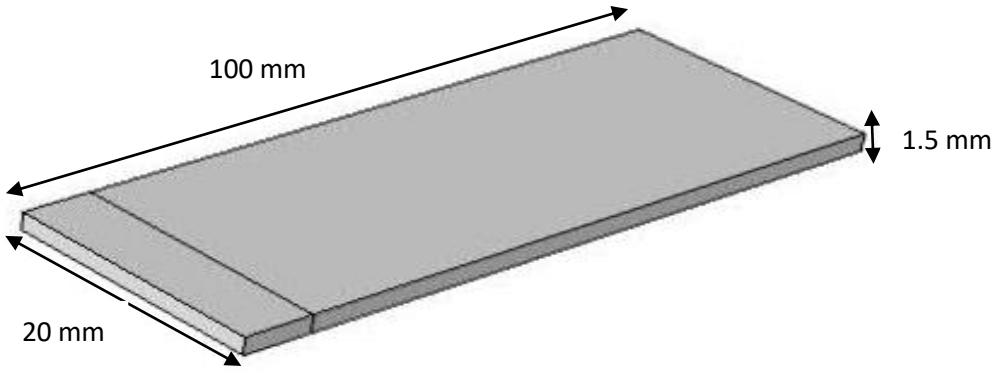

Figure.2.1 Schematic geometry of the symmetrical sample

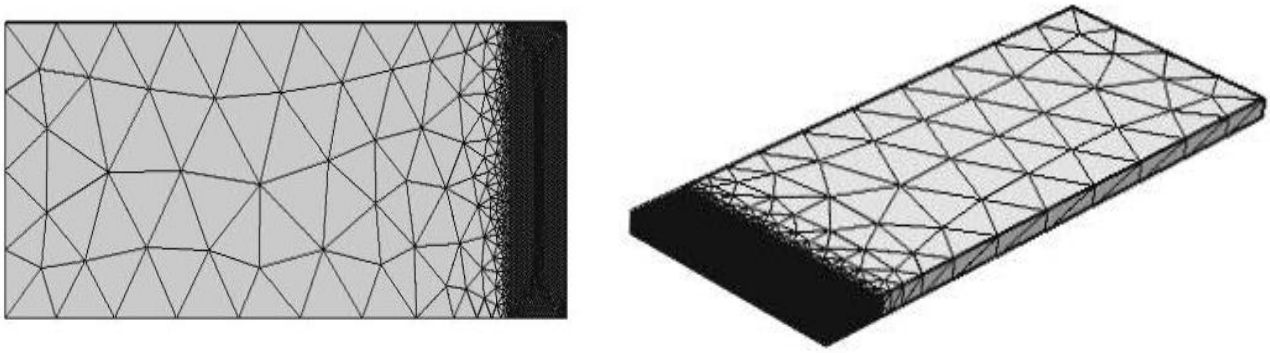

Figure.2.2 Mesh pattern used for discretizing the geometry

Table 2.2 Temperature dependent thermal properties of 2205 Duplex stainless steel [16]

Temperature (K)	**Thermal conductivity (W/m. K)**	**Specific heat (J/kg.K)**
250	15	500
500	18	500
750	20	500
1000	25	600
1250	27.5	620
1500	30	700
1750	35	750
1950	45	850
2250	55	1000
2500	65	1250

In the welding direction along the plane, symmetry has been considered. In order to accomplish the objectives of the research, this model's idealization is sufficient to depict the issue [15]. Selecting an appropriate number of elements has involved a series of convergence experiments, especially in the depth orientation along with the vicinity of the weld line. At the zone near weld line a dense mesh has been developed and coarse mesh has been considered for the remaining part. Total numbers of elements are 1,15,210. During the simulation process maximum surface temperature exceeds the liquidus temperature and hence the phase change has been considered. This phase change phenomenon has been done by considering latent heat of fusion L_f of the material. Following steps describe how this property is used for phase change purpose:

An effortless switching among phases occurs near the phase change temperature, during the period $\Delta T = TL - TS$, when a phase transition function α (T) is implemented. A mushy zone with heterogeneous material qualities exists throughout such timeframe. The shorter the time

period, the transition should be sharper. There are distinct specifications for the material's liquid and solid phases. To create a seamless crossover from solid to liquid, such parameters are paired with the phase transition factor. It is possible to define the material's heat capacity as [19]:

$C_P = C_{P,\,solid}\cdot(1-\alpha(T)) + C_{P,\,liquid}\cdot(\alpha(T))$

Similarly, for thermal conductivity and density of the material are expressed. For a pure solid, $\alpha(T) = \frac{T - T_S}{T_L - T_S} = 0$, and for a pure liquid, $\alpha(T) = \frac{T - T_S}{T_L - T_S} = 1$. During the transition period, properties of material are varying continuously. In the heat capacity, the latent heat is involved through an additional term.

Integrating this function over ΔT gives 1 and multiplying by the latent heat L_f gives the amount of latent heat that is released over ΔT.

The Apparent Heat Capacity method uses the following expression for the heat capacity:

$$C_P = C_{P,\,solid}\cdot(1-\alpha(T)) + C_{P,\,liquid}\cdot(\alpha(T)) + L_f\frac{\partial\alpha}{\partial T}$$

It is not necessary to know in advance where the phase interface appears, which is the benefit of this technique. Every investigation is carried out utilizing the 2205 Duplex stainless steel's temperature-dependent thermal characteristics.

The FE model is formulated with the following presumptions:

- ✓ The initial temperature of the work piece is 293.15 K. The laser beam is movable and the sheet material is fixed.
- ✓ The distribution of laser intensity follows a Gaussian mode.
- ✓ Material properties of the workpiece are isotropic
- ✓ Heat is transferred within the work piece via conduction, which follows Fourier's law. Heat loss occurs from the surfaces of the sheet metal to the surrounding air through radiation and free convection.
- ✓ During the simulation process maximum surface temperature exceeds the liquidus temperature and hence the phase change has been considered.

2.2.1. Governing equation and boundary conditions

The transient temperature field (T) in time (t) and space (x, y, z), in a heat transfer analysis, is realized through explaining the subsequent equation:

$$\frac{\partial}{\partial x}(k(T)\frac{\partial T}{\partial x})+\frac{\partial}{\partial y}(k(T)\frac{\partial T}{\partial y})+\frac{\partial}{\partial z}(k(T)\frac{\partial T}{\partial z})+Q_v=\rho(T)C_P(T)(\frac{\partial T}{\partial t}) \quad (1)$$

Here, k (T) is the thermal conductivity as a function of temperature in$Wm^{-1}K^{-1}$, ρ (T) is the density as a function of temperature in kg m^{-3}, C_P(T) is the specific heat as a function of temperature in J kg^{-1} K^{-1}, and Q_v is the volumetric heat flux in W m^{-3}.

The most commonly used heat sources of this kind have a Gaussian distribution. For simulating an accurate energy transfer to the work piece, the volumetric heat source model was utilized. The heat source that was employed in this investigation can be stated as [17,18]:

$$Q_v=Q(x,y,z)=\frac{3P}{\pi abd}\exp(-\frac{3x^2}{a^2})\exp(-\frac{3y^2}{b^2})\exp(-\frac{3z^2}{d^2}) \quad (2)$$

P is the total power of laser beam. The parameters a and b are taken to be equal to the radius of the laser beam, d is the max depth. The material cooling phase is made through natural convection and radiation from its surfaces exposed to ambient air.

The convection boundary condition can be expressed as follows:

$$q_{conv}=h(T_m-T_o) \quad (3)$$

Where, h is the heat transfer coefficient, which is taken as (10 W/m^2K) [16], T_m is the sheet metal surface temperature and T_0 is the ambient temperature, which is taken as 300K.

The radiation boundary condition can be expressed as follows:

$$q_{rad}=\varepsilon\sigma(T_m-T_o)^4 \quad (4)$$

ε is the emissivity (set as 0.7) [16] and σ is the Stefan Boltzmann constant (5.6703×10^{-8} W/m^2K^4).

2.2.2. Validation of numerical model

Due to the high expenses of experimental laser welding process, at the beginning we decided to validate this conduction welding model with published work.

(I) A simulation process is carried out for the analysis of 2205 Duplex stainless steel to obtain the depth of penetration and bead width. In order to verify the efficacy of the present simulation model, the outcomes are validated against the outcomes of **Batahgy** *et al.* [10].

Table 2.3 Validation of Response parameter

PROCESS PARAMETERS			RESPONSE PARAMETER				
			From Simulation study			From Experimental study of Batahgy *et al*	PERCENTAGE ERROR
Laser Power (kW)	**Welding speed (m/min)**	**Plate thickness (mm)**	Depth (mm)	Width (mm)	**Depth/ Width Ratio (f_t)**	**Depth/Width Ratio (f_s)**	$[\frac{f_t - f_s}{f_s} \times 100]$
8	0.5	6.4	5.15	5	1.03	0.99	4.04

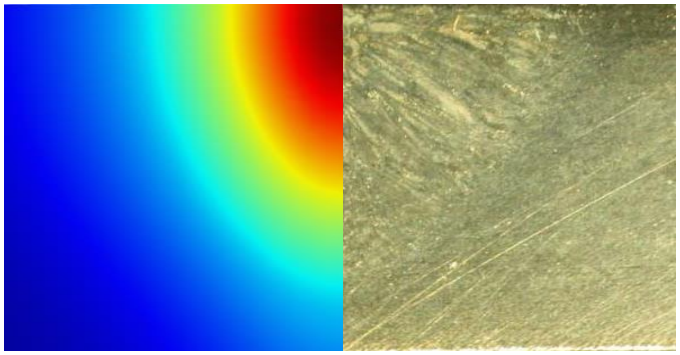

(a) (b)

Figure 2.3 Justification of Weld geometry of bead cross section surface: (a) Present Simulation Study, (b) Experimental study of Batahgy *et al*.

(II) A simulation process is carried out for thermal analysis of AISI 304 stainless steel to obtain the maximum temperature, depth of penetration and bead width. In order to verify the efficacy of the present simulation model, the outcomes are validated against the outcomes of Shanmugam *et al.* [20].

Table 2.4 Validation of Response parameters

PROCESS PARAMETERS	**RESPONSE PARAMETERS**	**From Present simulation study (f_t)**	**From simulation and experimental study of Shanmugam *et al.*(f_s)**	**Percentage error** $[\frac{f_t - f_s}{f_s} \times 100]$
	Depth of Penetration (mm)	1.99	1.98	0.51

Laser Power (W)	**Welding speed (mm/min)**	**Plate thickness (mm)**	**Bead Width (mm)**	1.6	1.56	2.56
1000	750	2.5	**Peak Temperature (^{0}C)**	3016	3025	-0.3

Regarding the validation, the present model is quite acceptable, so we designed an experimental matrix based on this simulation model and investigated the process parameters. Through Design Expert 7.0 software statistical computations were accomplished, which is employed as well to derive the final regression equation. In accordance with a central composite design (CCD) comprising three components and five levels, the computational architecture is created applying the response surface methodology.

2.3. Development of Mathematical Model

Depending on simulation results, to develop a safe operating window by optimizing process parameters and to design a functional co-relationship among process and response parameters so that we can predict future outcomes we used one of the statistical techniques named Response surface methodology [21,22].

2.3.1. Response Surface Methodology

Response surface methodology is an array of statistical and mathematical methods which are helpful in empirical modeling and optimization. Regression analysis and experimentation can be used to create a model that predicts the answer for a few independent process parameters. [21, 22]. Assuming that every variable is quantifiable, the response surface can be represented in the following way:

$$y = f(x_1, x_2, x_3, ...x_n) \pm \varepsilon$$

where y is the response, f is the function of response, ε is the experimental error, and $(x_1, x_2, x_3, ...x_n)$ are independent parameters. In order to derive an approximative correlation among a genuine response and the number of design variables using observable data within the procedure or mechanism, the response surface methodology is applied through a series of planned experiments. Responses to laser welding of 2205 Duplex stainless steel are gathered numerically in the current research.

2.3.2. Design matrix

The notation and units of process parameters (low and high levels) are listed in Table 2.6. A central composite design matrix with three factors (laser power, welding speed and laser beam diameter) and five levels ($-\alpha$, -1, 0, +1, $+\alpha$), is considered.

Table 2.5 Process parameters and their units and limits

Parameter	Notation	Unit	Low actual	High actual
Laser power	*P*	W	400	500
Welding speed	*V*	mm/min	500	750
Beam diameter	*D*	mm	0.7	1

The response surface method is employed to create the design matrix for attaining the regression equations and to produce the statistical response plots. The numerical simulations are carried out according to the design matrix and the maximum temperature and weld bead dimensions as responses are listed in Table 2.6.

Table 2.6 Design layout and numerically calculated responses

Sl. No.	**Process parameters**			**Responses**		
	Power [W]	**Speed [mm/min]**	**Beam diameter [mm]**	**Bead Width [mm]**	**DOP [mm]**	**Maximum Temperature [K]**
1	400	750	1	0.53	0.6	2052.99
2	450	625	0.85	0.66	0.83	2357.7
3	400	500	0.7	0.66	0.97	2434.31
4	400	500	1	0.71	0.79	2218.82
5	534.09	625	0.85	0.75	1.17	2553.91
6	450	835.22	0.85	0.55	0.71	2226.612
7	500	500	0.7	0.81	1.22	2691.4
8	400	750	0.7	0.5	0.74	2263.75
9	450	625	0.85	0.66	0.83	2357.7
10	450	625	0.85	0.66	0.83	2357.7
11	500	750	0.7	0.65	1	2525.6
12	365.91	625	0.85	0.5	0.67	2138.94
13	450	414.78	0.85	0.85	1.06	2517.814
14	450	625	0.85	0.66	0.83	2357.7
15	500	750	1	0.61	0.8	2279.2

16	500	500	1	0.85	1	2458.64
17	450	625	1.1	0.68	0.74	2179.77
18	450	625	0.85	0.66	0.83	2357.7
19	450	625	0.6	0.61	0.96	2569.812
20	450	625	0.85	0.66	0.83	2357.7

2.4. Results and Discussion

2.4.1. Transient temperature field analysis

At laser power of 500 W, welding speed of 750 mm/min, spot diameter of 1 mm and plate thickness of 1.5 mm, figure 2.4 shows the spot weld geometry of top surface when the laser beam is at middle of the plate (i.e., 10 mm) and maximum temperature profile along weld line. It is evident from the figure 2.4 (a) that throughout the initial heating phase, the temperature on the top surface progressively rises and achieves a constant peak. Once the laser beam approaches the plate's uppermost edge, the plate acquires its highest temperature. From the figure 2.4 (b), it is seen that the maximum temperature of 2272.4 K has been achieved at the center of laser beam and then it is gradually decreasing to 400 K. The temperature distribution on the plate at four different time instances has been shown in Figure 2.5: (a) The times at which the laser beam is at the starting point of the plate (t = 0.1008 s), the center of the plate (t = 0.8 s), the outermost boundary of the plate (t = 1.5008 s), and the end of the plate (t = 15 s) are all included in the analysis. At the most distant position on the weld line, a peak temperature of 2277 K is obtained while heating. The temperature continues to decline within the range of 300 K to 407 K after 15 seconds.

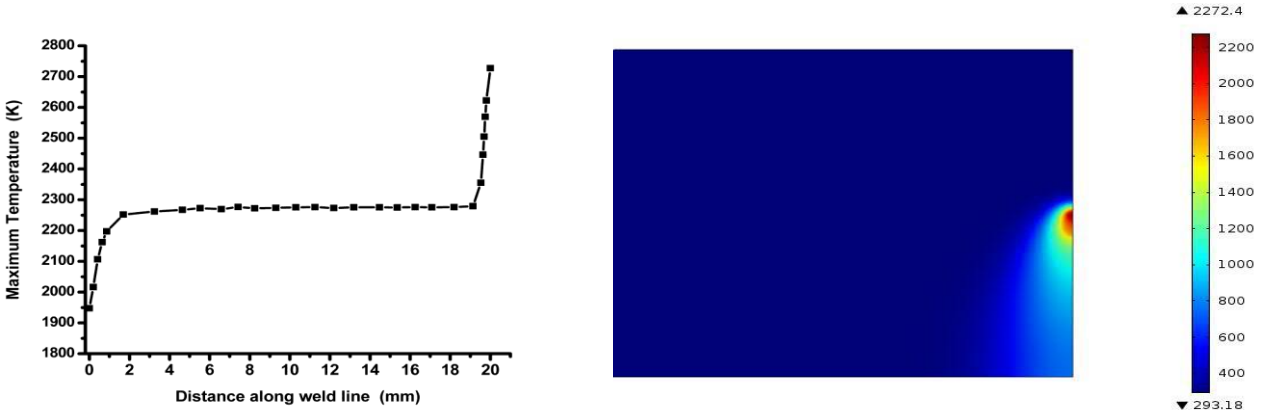

(a) (b)

Figure 2.4: (a) Maximum temperature along the weld line and (b) Spot weld geometry of top surface when the laser beam is at middle of the plate (t=0.8s) (laser power = 500W, welding speed = 750 mm/min, beam diameter = 1 mm, plate thickness = 1.5 mm)

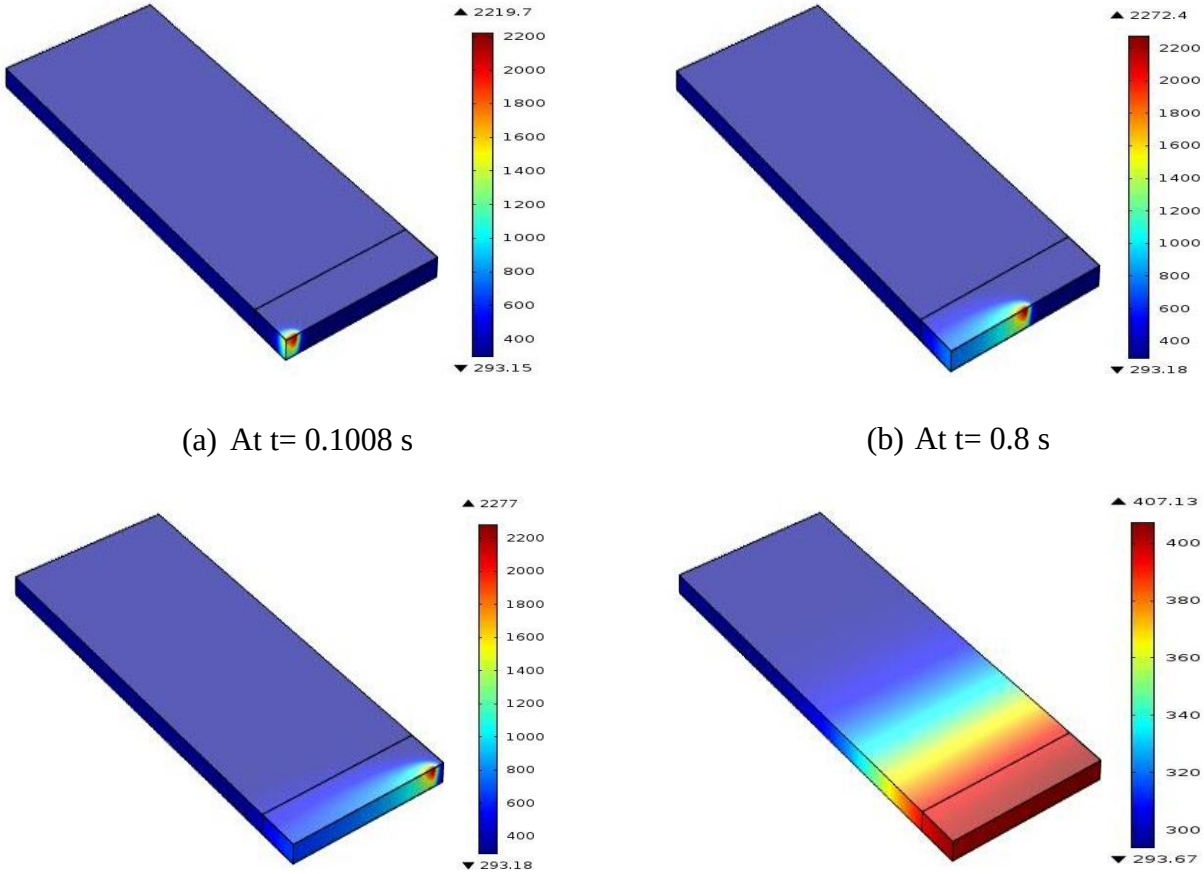

(a) At t= 0.1008 s

(b) At t= 0.8 s

(c) At t= 1.5008 s

(d) At t= 15 s

Figure 2.5 Temperature distribution at four instances: (a) beam is at the beginning, (b) beam is at the middle, (c)beam is at the farthest edge, (c) after cooling (laser power = 500W, welding speed = 750 mm/min, beam diameter = 1 mm, plate thickness = 1.5 mm)

The numerical simulations along the weld line at the middle i.e., 10 mm are carried out according to the design layout for 20 numbers of experiments consisting the Maximum temperature, bead width and depth of penetration as responses are tabulated in table 5. Depending upon these results temperature distribution with time and along weld line for different laser powers, beam diameters and welding speeds at the top edge of the upper surface have been plotted, shown in figure 2.6 and 2.7. In figure 2.8 and 2.9, changes in depth of penetration, bead width and maximum temperature with laser power, beam diameter and welding speed have been shown.

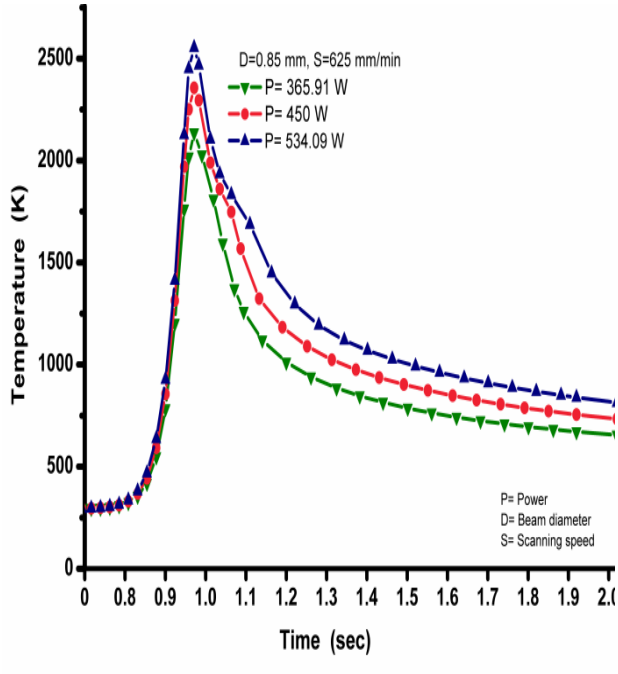
D=0.85 mm, S=625 mm/min
P= 365.91 W
P= 450 W
P= 534.09 W
Temperature (K)
Time (sec)
P= Power
D= Beam diameter
S= Scanning speed

(a)

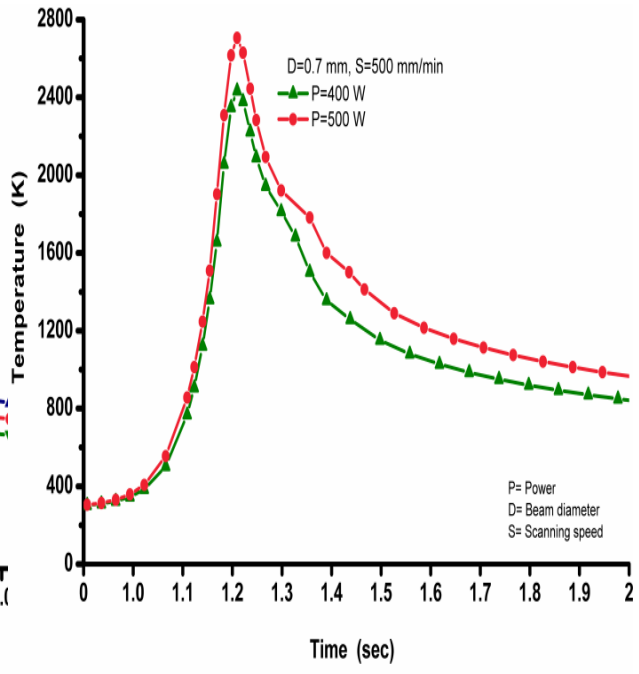
D=0.7 mm, S=500 mm/min
P=400 W
P=500 W
Temperature (K)
Time (sec)
P= Power
D= Beam diameter
S= Scanning speed

(b)

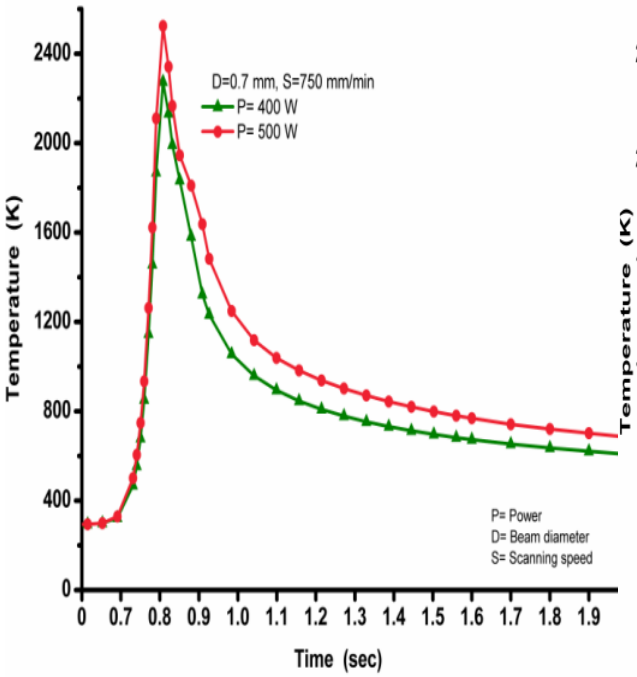
D=0.7 mm, S=750 mm/min
P= 400 W
P= 500 W
Temperature (K)
Time (sec)
P= Power
D= Beam diameter
S= Scanning speed

(c)

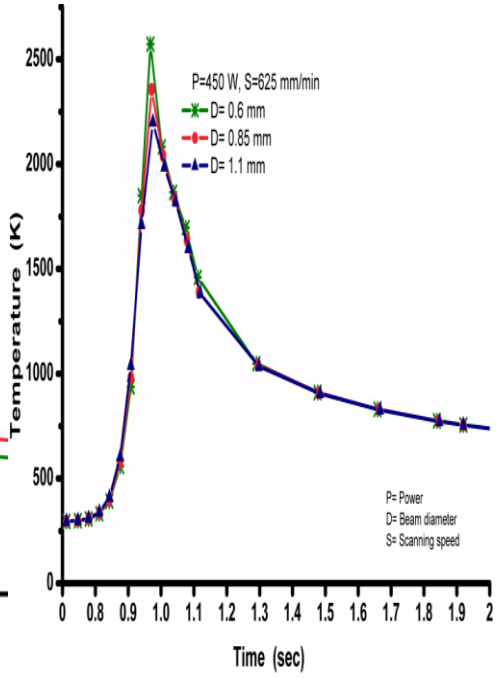
P=450 W, S=625 mm/min
D= 0.6 mm
D= 0.85 mm
D= 1.1 mm
Temperature (K)
Time (sec)
P= Power
D= Beam diameter
S= Scanning speed

(d)

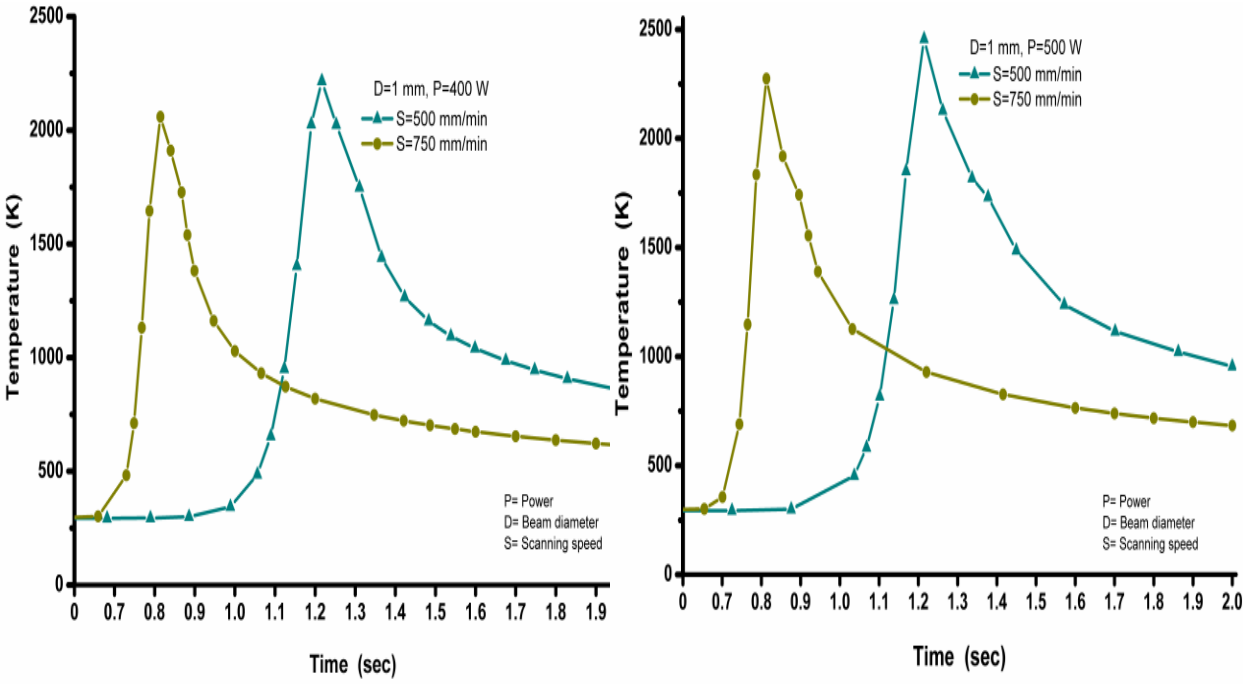

(e) (f)

Figure.2.6 (a, b, c, d, e, f) : Temperature distribution with time for different laser powers, beam diameters and welding speeds on the upper surface of the plate at the middle (10 mm) along weld line

Figure 2.6 shows the temperature profile of the node at the upper surface of the plate at the middle (10 mm) along weld line for different powers, beam diameter and welding speed while other process parameters are kept constant. The figure 2.6(a) shows, higher temperature is achieved with the increase of power because with the increase of power, applied heat input to the material is increased, which is able to produce higher temperature.

Figure 2.6(b) and 2.6(c) shows the temperature profile for two different powers while beam diameter is kept constant at 0.7 mm and welding speeds are kept at 500 mm/min and 750 mm/min respectively. Higher temperature is achieved with higher power but with higher welding speed peak temperature decreases. From the figure 2.6(b) it is shown, when speed is 500 mm/min, peak temperatures are near 2600 K and 2400 K for 500 W and 400 W respectively at 0.7 mm beam diameter. From figure 2.6(c) shows, when speed is 750 mm/min peak temperatures are near 2500 K and 2300 K for 500 W and 400 W respectively at the same beam diameter of 0.7 mm.

Figure 2.6(d) shows the peak temperature for different beam diameter while laser power and welding speed are kept constant at 450 W and 625 mm/min respectively. Higher temperature

is achieved with the decrease of beam diameter because with the decrease of beam diameter, the applied heat flux increases, causing higher heat input to the material which produces higher temperature.

Figures 2.6(e) and 2.6(f) show the peak temperature profile of the node at the upper surface for different welding speed while beam diameter is kept constant at 1 mm and powers are kept at 400 W and 500 W respectively. It is shown for fixed beam diameter and power the time instant for peak temperature will be varied with the variation of welding speed. For figure 2.6(e), peak temperatures are near 2100 K and 2300 K at time instants of 0.8 s and 1.2 s for welding speed of 750 mm/min and 500 mm/min respectively at 400 W power and 1 mm beam diameter. For figure 2.6(f), peak temperatures are near 2300 K and 2500 K at time instants of 0.8 s and 1.2 s for welding speed of 750 mm/min and 500 mm/min respectively at 500 W power and 1 mm beam diameter.

Figure 2.7 shows the maximum temperature of the top surface of the material along the weld line for different power, beam diameter and welding speed while other process parameters are kept constant. Figure 2.7(a) shows that with increase of power the maximum temperature increases as applied heat input to the material increases.

It is evident from Figure 2.7(b) that with increase of welding speed maximum temperature decreases. The reason behind this is higher welding speed reduces the interaction time between applied heat source and material surface.

In Figure 2.7(c), we see that with the increase of beam diameter maximum temperature decreases as higher beam diameter reduces the applied heat flux, resulting in decreased heat input per unit area to the material. For different beam diameter and welding speed, figures 2.7(d) and 2.7(e) show that the maximum temperature decreases with the increase of beam diameter and speed while the power is kept constant.

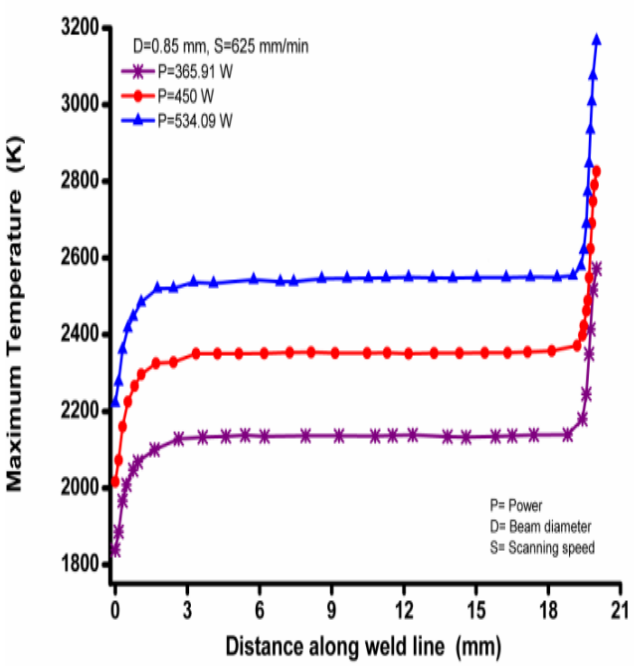
D=0.85 mm, S=625 mm/min
P=365.91 W
P=450 W
P=534.09 W
Maximum Temperature (K)
Distance along weld line (mm)
P= Power
D= Beam diameter
S= Scanning speed

(a)

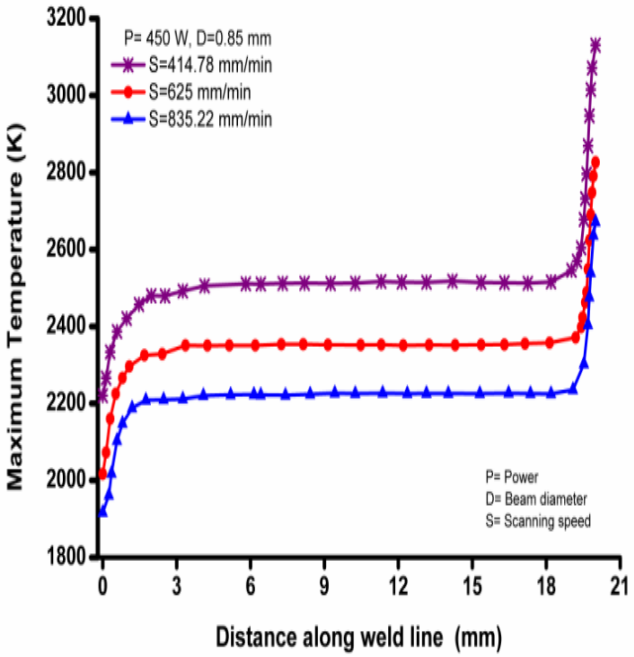
P= 450 W, D=0.85 mm
S=414.78 mm/min
S=625 mm/min
S=835.22 mm/min
Maximum Temperature (K)
Distance along weld line (mm)
P= Power
D= Beam diameter
S= Scanning speed

(b)

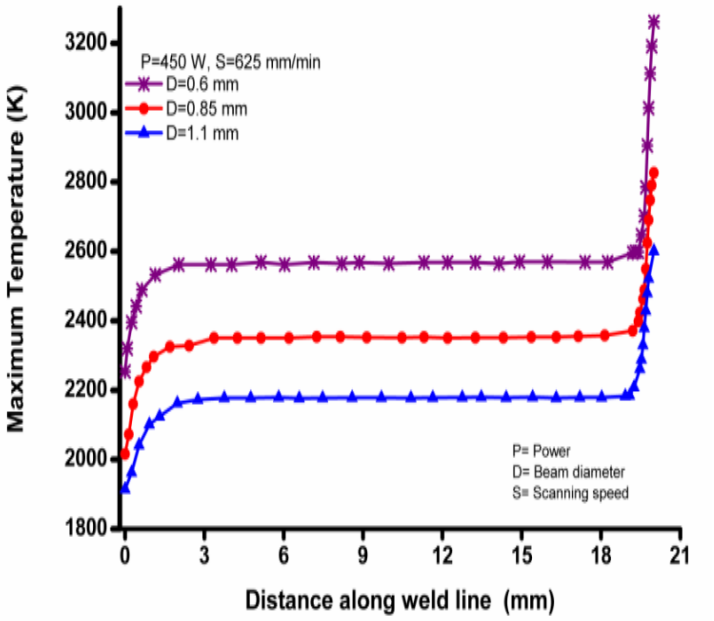
P=450 W, S=625 mm/min
D=0.6 mm
D=0.85 mm
D=1.1 mm
Maximum Temperature (K)
Distance along weld line (mm)
P= Power
D= Beam diameter
S= Scanning speed

(c)

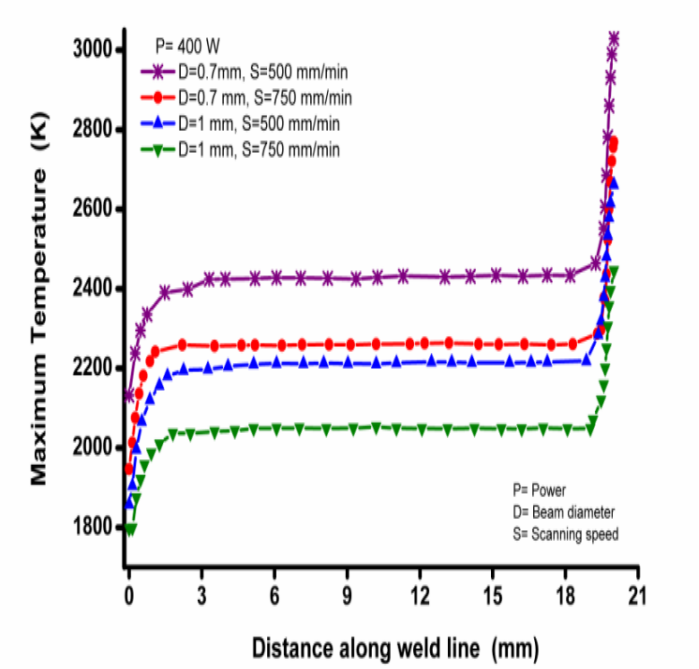

(d)

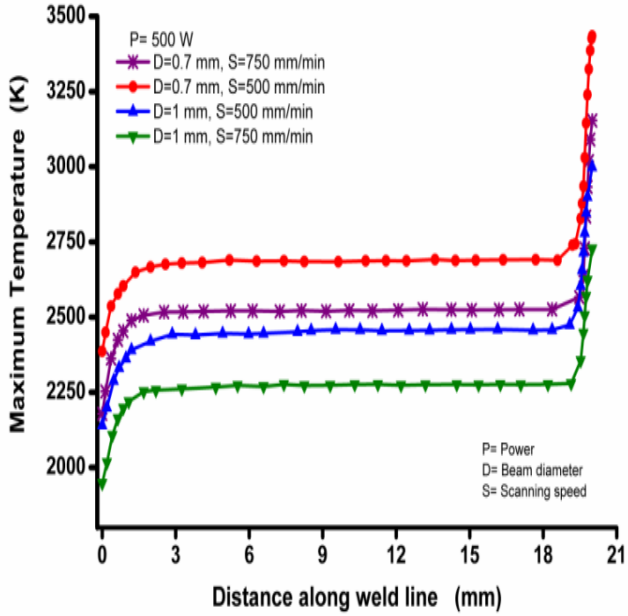

(e)

Figure.2.7 (a, b, c, d, e): Maximum Temperature at the top surface of material with distance along weld line for different laser powers, beam diameters and welding speeds

Figure 2.8(a), 2.8(b) and 2.8(c) show the effects of Laser power, Beam diameter and Welding speed respectively on Bead width and Depth of penetration of welded material. From figure 2.8(a) it is revealed that bead with and depth of penetration both increases with increase of power as heat input increases.

It is seen from figure 2.8(b) that with increase of beam diameter, bead with increases but depth of penetration decreases as heat flux, increases along radial direction of laser beam but decreases along thickness of material.

From figure 2.8(c) we can see that both bead width and depth of penetration decreases with increase of welding speed as higher welding speed reduces the interaction time between applied heat source and material resulting in decrease of heat input to the material.

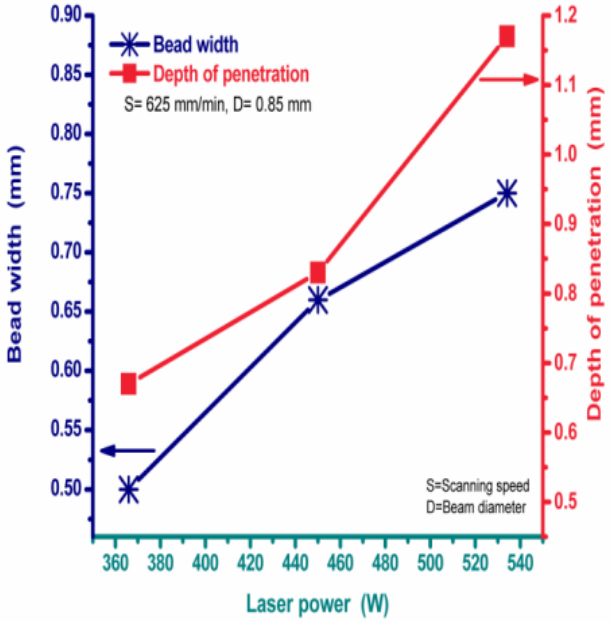

(a)

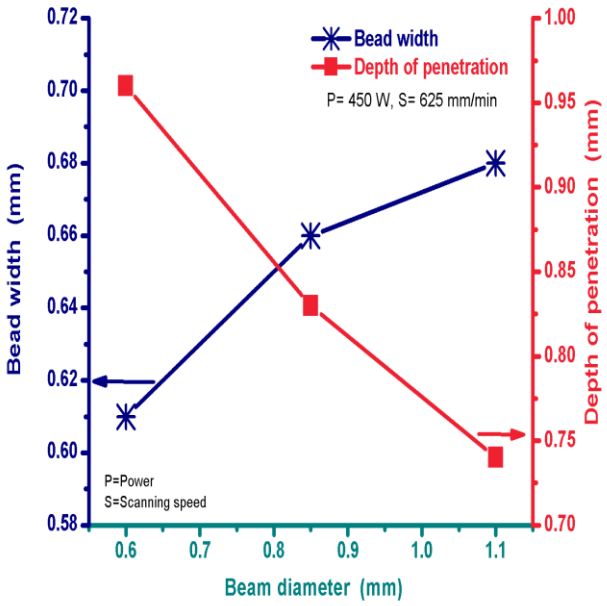

(b)

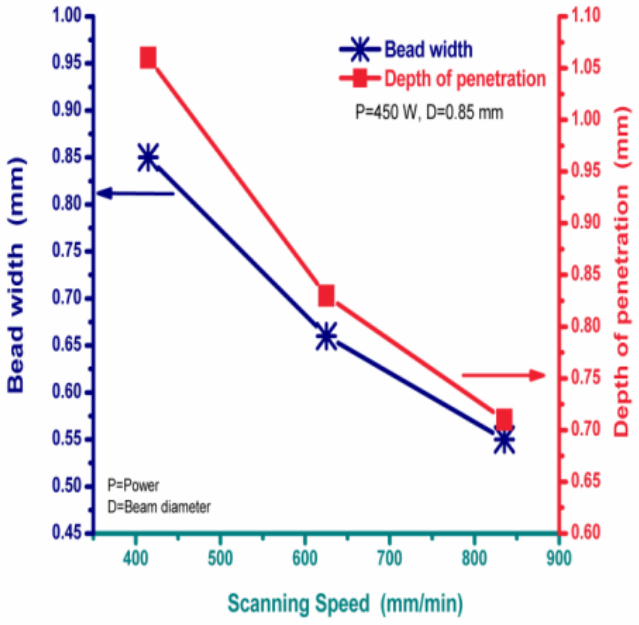

(c)

Figure 2.8 Effect of (a) Laser power, (b) Beam diameter and (c) Welding speed on Bead width and Depth of penetration of welded material

Figure 2.9(a), 2.9(b) and 2.9(c) show the effects of Laser power, Beam diameter and Welding speed respectively on Maximum temperature values of the top surface of the material after

welding. Figure 2.9(a) shows temperature value increases with increase of power. It is observed from figure 2.9(b) that temperature value decreases with increase of welding speed and from figure 2.9(c) it is observed that temperature value decreases with increase of beam diameter.

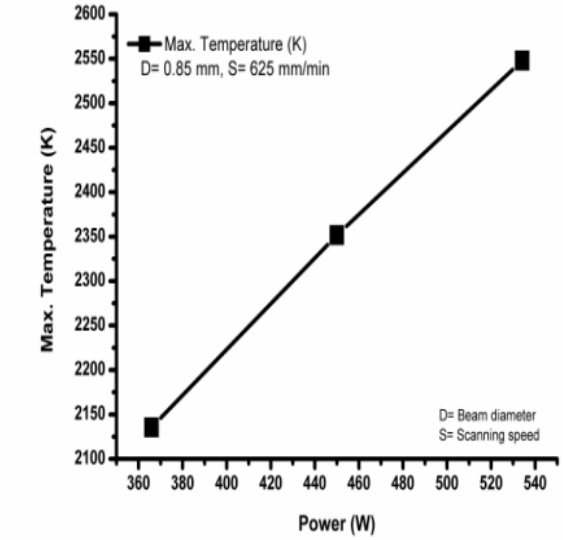

(a)

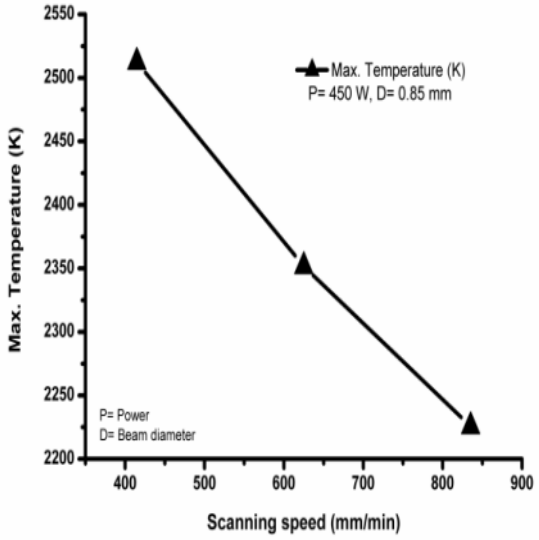

(b)

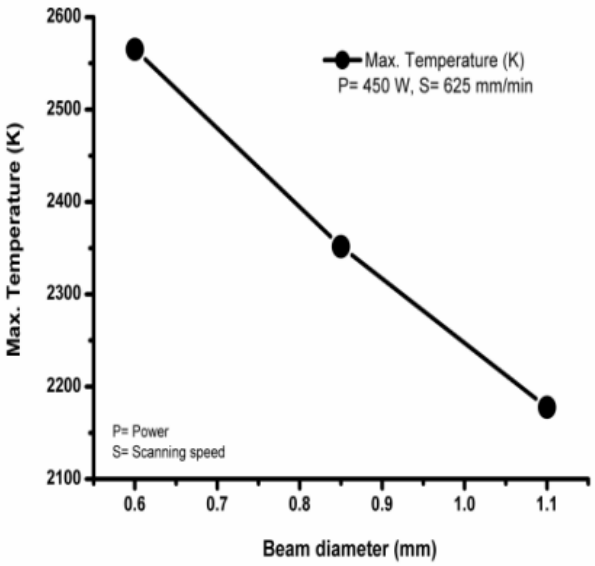

(c)

Figure 2.9 Effect of (a) Power, (b) Welding speed and (c) Beam diameter on Maximum temperature values of the top surface

2.4.2. Analysis of Variance (ANOVA)

ANOVA stands for Analysis of Variance. ANOVA technique and sequential *f*-test are employed to check the adequacy of a model through Design Expert® 7.0 application to attain the best-fit models.

The results from experiments are analyzed using ANOVA. The estimates and tests are intended to evaluate population variance and mean hypotheses. Using an ANOVA, one can divide the overall variation in a collection of data by multiple factors. To determine how the source of variation affects the overall variance, it needs to be evaluated. Comparing means when there are three or more has another usage for it.

H_0: all means are equal: $\mu_1 = \mu_2 = \ldots \mu_T$.

H_A: not all means are equal: $\mu_i \neq \mu_j$.

When the numerator and denominator degrees of freedom are appropriately specified at the selected stage, the variance ratio that is expressed as F, is the ANOVA test statistic.

$$F = \frac{Among \text{ groups mean square}}{Within \text{ groups mean square}} = \frac{MS_{Group}}{MS_{Error}}$$

The null hypothesis is rejected when F has a large value. A minimal amount indicates that it is not rejected. The ANOVA table includes sections labeled as mean squares (MS), sums of squares (SS), and degrees of freedom (df). Total $df = N - 1$ (N, the total number of observations), Group $df = k - 1$ (k, the total number of groups), Error $df = N - k$. The phrase "error" expresses the variation between the population mean of each group and each individual observation. Sum of Squares Total value (SS_{Total}) represents all of the data's variation. Variance of the estimated factor level mean from the overall mean is known as SS_{Group}. SS_{Error} is the deviation of an observation from its corresponding factor level mean.

corresponding factor level mean.

$$SS_{Total} = SS_{Group} + SS_{Error}$$

$$SS_{Group} = \sum n_i (\overline{y_i} - \overline{y_{..}})^2$$

$$SS_{Error} = \sum_i \sum_j (y_{ij} - \overline{y_i})^2$$

$$SS_{Total} = \sum_i \sum_j (y_{ij} - \overline{y})^2$$

$$MS_{Total} = MS_{Group} + MS_{Error}$$

$\overline{y_i}$ = Mean of the observations at the i th level of group

$\overline{y}$ = Mean of all observations

y_{ij} = Value of the j th observation at the i th level of group

$$\left\{ MS_{Group} = \frac{SS_{Group}}{df_{Group}} , MS_{Error} = \frac{SS_{Error}}{df_{Error}} \right\}$$

2.4.2.1. Effect of Process parameters on the Bead Width

Table 2.7 ANOVA for Response Surface Quadratic Model of Bead Width

Source	**Sum of Squares**	**df**	**Mean Square**	**F-Value**	**Prob > F p-value**	
Model	0.19	9	0.021	151.06	< 0.0001	significant
P	*0.065*	*1*	*0.065*	*464.42*	*< 0.0001*	
V	*0.11*	*1*	*0.11*	*813.32*	*< 0.0001*	
D	*2.863E-003*	*1*	*2.863E-003*	*20.53*	*0.0011*	
PV	*4.500E-004*	*1*	*4.500E-004*	*3.23*	*0.1027*	
PD	*8.000E-004*	*1*	*8.000E-004*	*5.74*	*0.0376*	
VD	*1.250E-003*	*1*	*1.250E-003*	*8.96*	*0.0135*	
P^2	*1.611E-003*	*1*	*1.611E-003*	*11.55*	*0.0068*	
V^2	*3.663E-003*	*1*	*3.663E-003*	*26.27*	*0.0004*	
D^2	*1.768E-004*	*1*	*1.768E-004*	*1.27*	*0.2865*	
Residual	1.394E-003	10	1.394E-004			
Lack of Fit	*1.394E-003*	*5*	*2.789E-004*			
Pure Error	*0.000*	*5*	*0.000*			
Cor Total	0.19	19				
Standard deviation = 0.012 Mean=0.66 Coefficient of variation (%) =1.79 Predicted residual error of sum of squares (PRESS) = 0.011				R^2= 0.9927 Adjusted R^2= 0.9861 Predicted R^2=0.9409 Adequate precision=43.228		

The final mathematical model for Bead Width (B_W) in terms of actual factors as determined by Design-Expert® 7.0 software is shown below:

$$B_W = -1.35840 + 7.06693\times10^{-3}\times P - 8.97834\times10^{-4}\times V + 1.37779\times D - 1.20000\times10^{-6}\times P\times V - 1.33333\times10^{-3}\times P\times D - 6.66667\times10^{-4}\times V\times D - 4.22927\times10^{-6}\times P^2 + 1.02037\times10^{-6}\times V^2 - 0.15565\times D^2 \quad (5)$$

The model F-value of 151.06 indicates the significance of model. Here is a probability of only 0.01% so that a 'model F-value' being huge might happen owing to noise. The ANOVA table of the quadratic model with other adequacy measures R^2, adjusted R^2 and predicted R^2 are listed in Table 2.8. The adequacy measures R^2, adjusted R^2 and predicted R^2 are in reasonable agreement and are close to 1. The associated p-value of less than 0.05 for the model indicates model terms are significant. The adequate precision compares the signal to noise ratio and a ratio greater than 4 is desirable. The ANOVA results show that the effect of laser power (P), welding speed (V) and beam diameter (D), the quadratic effects of the square of laser power (P^2) and welding speed (V^2), and the two-level interaction of laser power and beam diameter ($P\times D$) and welding speed and beam diameter ($V\times D$) are the most significant model terms related with the bead width. The other model terms are not significant.

The response surface model that has been created allows for the identification of the impacts of variables on the response. Figure 2.10 (a) shows the response contour and 3-D surface plot of the effects of laser power and welding speed on bead width. It is observed from these figures that the bead width increases when the laser power increases and the welding speed is kept constant. Similarly, when welding speed is amplified at a static laser power, the bead width is reduced. If power is increased, more heat input will be generated on work piece. Thus, the work piece will absorb more heat and bead width will be increased. As welding speed increases, the work piece absorbs minimal heat as a consequence of a shorter duration of contact among the laser beam and the work piece. Therefore, when welding speed increases, bead width reduces. The response contour and 3-D surface plot of the effects of laser power and beam diameter on the bead width has been seen in figure 2.10 (b). It is observed from the figure, that bead width increases when laser power is increased keeping the beam diameter as constant. Bead width also increases with increase of beam diameter while power is kept constant. As beam diameter increases, the heat distribution along beam radius will be increased, resulting in a wider bead width. The effects of welding speed and

beam diameter are seen from the response contour and 3-D surface plot in figure 2.10 (c). It is seen from this figure that bead width increases with beam diameter while welding speed is kept constant. Similarly, bead width decreases with welding speed while beam diameter is kept constant.

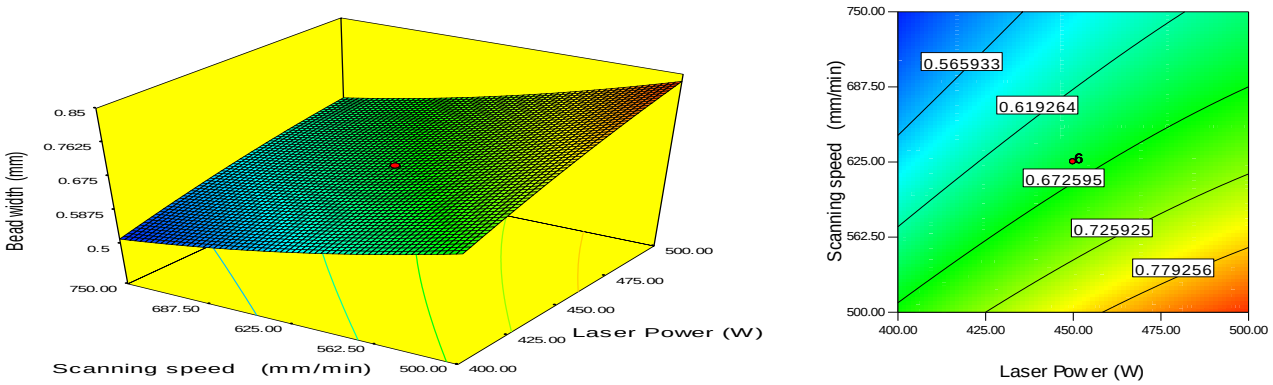

(a) At 0.85 mm Beam diameter

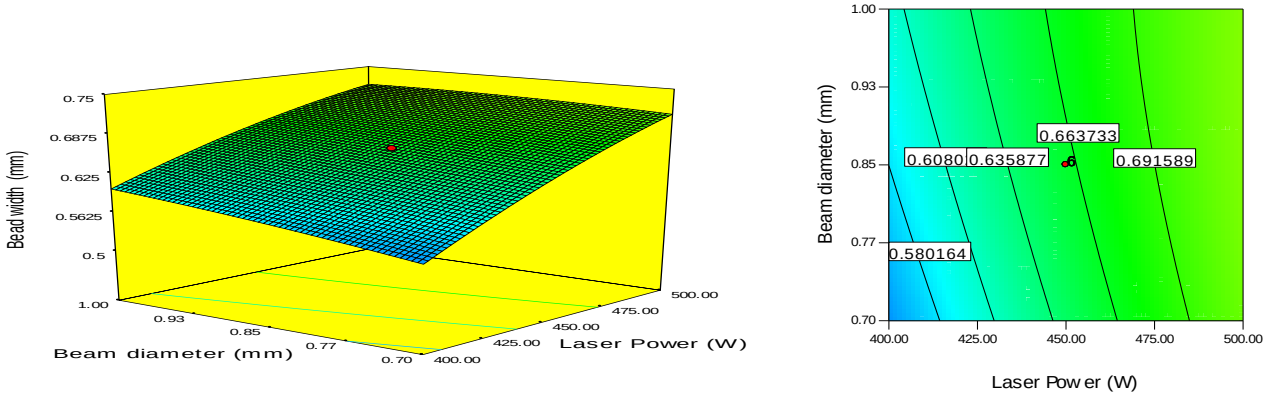

(b) At 625 mm/min Welding speed

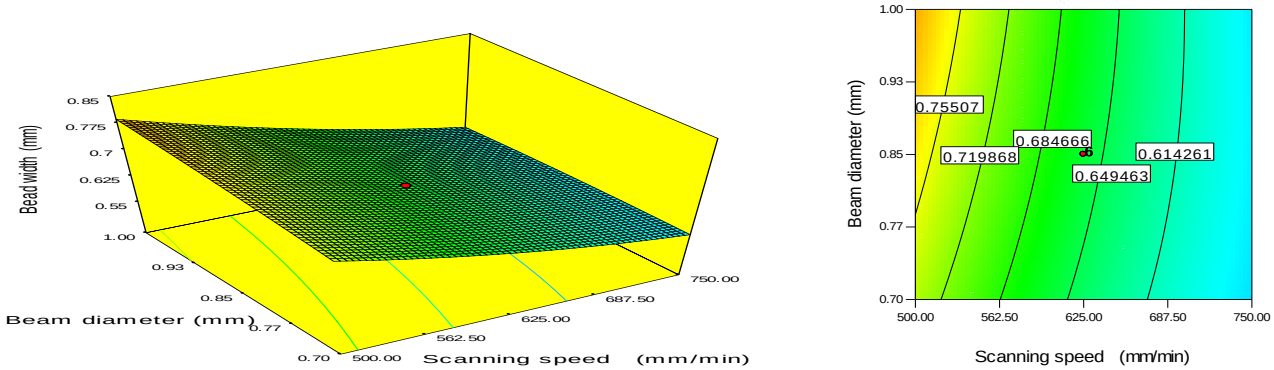

(c) At 450 W Power

Figures 2.10 (a-c): Contours and response surface plots showing the effects of input parameters on the bead width

2.4.2.2. Effect of Process parameters on the Depth of Penetration

Table 2.8 ANOVA for Response Surface Quadratic Model OF Depth of penetration

Source	**Sum of Squares**	**df**	**Mean Square**	**F-Value**	**Prob > F p-value**	
Model	0.49	9	0.054	86.70	< 0.0001	significant
P	*0.23*	*1*	*0.23*	*363.47*	*< 0.0001*	
V	*0.15*	*1*	*0.15*	*239.24*	*< 0.0001*	
D	*0.090*	*1*	*0.090*	*144.43*	*< 0.0001*	
PV	*0.000*	*1*	*0.000*	*0.000*	*1.0000*	
PD	*1.250E-003*	*1*	*1.250E-003*	*2.00*	*0.1876*	
VD	*4.500E-004*	*1*	*4.500E-004*	*0.72*	*0.4159*	
P^2	*0.015*	*1*	*0.015*	*23.88*	*0.0006*	
V^2	*5.648E-003*	*1*	*5.648E-003*	*9.04*	*0.0132*	
D^2	*7.939E-004*	*1*	*7.939E-004*	*1.27*	*0.2859*	
Residual	6.247E-003	10	6.247E-004			
Lack of Fit	*6.247E-003*	*5*	*1.249E-003*			
Pure Error	*0.000*	*5*	*0.000*			
Cor Total	0.49	19				
Standard deviation=0.025 Mean=0.87 Coefficient of variation (%) =2.87 Predicted residual error of sum of squares (PRESS) = 0.048				R^2=0.9873 Adjusted R^2=0.9760 Predicted R^2=0.9037 Adequate precision=35.628		

The final mathematical model for depth of penetration (D_P) in terms of actual factors as determined by Design expert software is furnished below:

$$\begin{aligned} D_P = {} & +3.56720 - 7.58608\times10^{-3}\times P - 2.76059\times10^{-3}\times V - 0.60263\times D \\ & + 0.000000\times P\times V - 1.66667\times10^{-3}\times P\times D + 4.00000\times10^{-4}\times V\times D \\ & + 1.28684\times10^{-5}\times P^2 + 1.26698\times10^{-6}\times V^2 + 0.32987\times D^2 \end{aligned} \quad (6)$$

The model F-value of 86.70 indicates the significance of model. Here is a probability of only 0.01% so that a 'model F-value' being huge might happen owing to noise. The ANOVA table of the quadratic model with other adequacy measures R^2, adjusted R^2 and predicted R^2 are listed in Table 2.9. The adequacy measures R^2, adjusted R^2 and predicted R^2 are in reasonable agreement and are close to 1. The associated p-value of less than 0.05 for the model indicates model terms are significant. The adequate precision compares the signal to noise ratio and a ratio greater than 4 is desirable. According to the ANOVA results, the most significant model terms correlated with the bead width are the impacts of laser power (P), welding speed (V), and beam diameter (D), as well as the quadratic effect of the square of laser power (P^2) and welding speed (V^2). The other model terms are not significant.

Response surface models that have been designed allow for the identification of the impacts of variables on the response. Figure 2.11 (a) shows the response contour and 3-D surface plot of the effects of the laser power and welding speed on the depth of penetration. From the figure, it is found that the depth of penetration increases when the laser power increases and the welding speed is kept constant. Similarly, when welding speed is amplified at a static laser power, depth of penetration is reduced. If power is increased, more heat input will be generated on work piece. Thus, the work piece will absorb more heat and depth of penetration will be increased. As welding speed increases, An inverse relationship among the work piece's interface period and the laser beam causes the work piece to absorb minimal heat. Consequently, when welding speed increases, the penetration depth reduces. The response contour and 3-D surface plot of the effects of beam diameter and laser power on the depth of penetration can be seen from figure 2.11(b). It is observed from the figure, that depth of penetration will increase if laser power increases at fixed beam diameter and decrease if beam diameter increases at fixed laser power. As beam diameter increases, the heat power density per area will be reduced, results less penetration of heat into the work piece. From figure 2.11(c), the response contour and 3-D surface plot of effects of welding speed and beam diameter on the depth of penetration can be observed. It is observed from the figure,

that depth of penetration will decrease for both cases if beam diameter increase at fixed welding speed as the heat power density per area will decrease results less heat penetration into work piece and if welding speed increases at fixed beam diameter as the interaction time of laser beam on work piece decreases results less absorption of heat by the work piece.

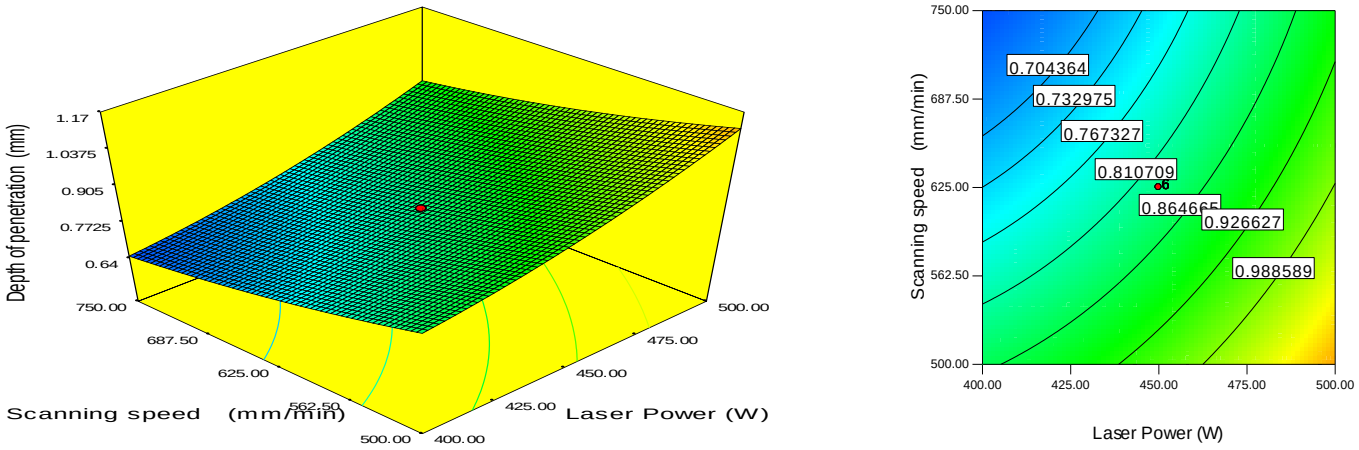

(a) At 0.85 mm Beam diameter

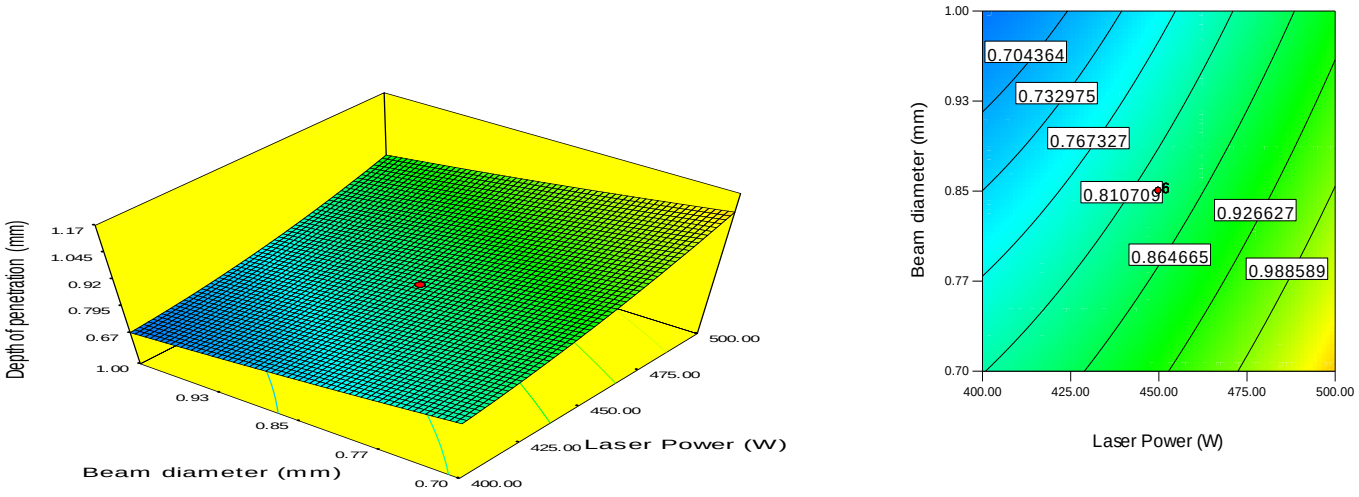

(b) At 625 mm/min Welding speed

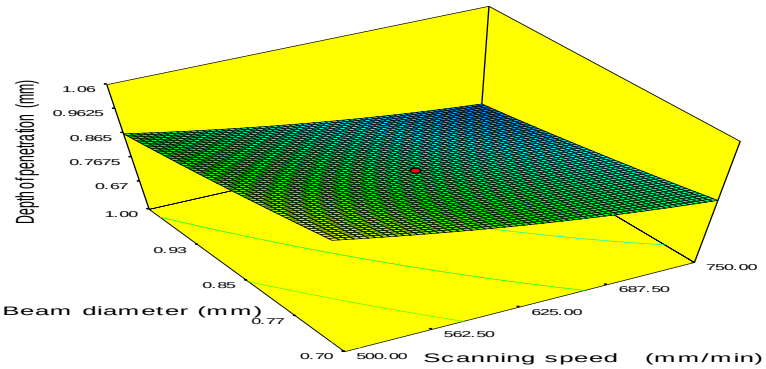

(c) At 450 W Power

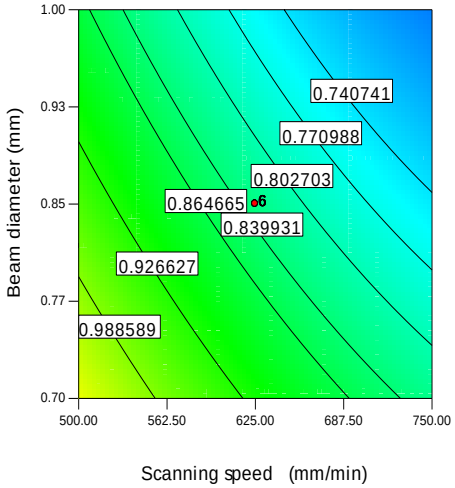

Figures 2.11 (a-c): Contours and response surface plot show the effects of input parameters on the depth of penetration

2.4.2.3. Effect of Process parameters on the Maximum Temperature

Table 2.9 ANOVA for Response Surface Quadratic Model OF Maximum Temperature

Source	**Sum of Squares**	**df**	**Mean Square**	**F-Value**	**Prob > F p-value**	
Model	4.879E+005	9	54215.55	7145.64	< 0.0001	significant
P	*2.074E+005*	*1*	*2.074E+005*	*27331.57*	*< 0.0001*	
V	*1.005E+005*	*1*	*1.005E+005*	*13242.07*	*< 0.0001*	
D	*1.785E+005*	*1*	*1.785E+005*	*23527.94*	*< 0.0001*	
PV	*9.79*	*1*	*9.79*	*1.29*	*0.2825*	
PD	*349.93*	*1*	*349.93*	*46.12*	*< 0.0001*	
VD	*9.92*	*1*	*9.92*	*1.31*	*0.2794*	
P^2	*212.32*	*1*	*212.32*	*27.98*	*0.0004*	
V^2	*401.63*	*1*	*401.63*	*52.94*	*< 0.0001*	
D^2	*552.29*	*1*	*552.29*	*72.79*	*< 0.0001*	
Residual	75.87	10	7.59			

Lack of Fit	*75.87*	*5*	*15.17*			
Pure Error	*0.000*	*5*	*0.000*			
Cor Total	4.880E+005	19				
Standard deviation=2.75 Mean=2362.89 Coefficient of variation (%) =0.12 Predicted residual error of sum of squares (PRESS) =642.66				R^2=0.9998 Adjusted R^2=0.9997 Predicted R^2=0.9987 Adequate precision=332.005		

The final mathematical model for maximum temperature (T_M) in terms of actual factors as determined by Design expert software is shown below:

$$\begin{aligned} T_M &= +1926.60170 + 4.70647 \times P - 0.97836 \times V - 795.97907 \times D \\ &\quad -1.77000 \times 10^{-4} \times P \times V - 0.88183 \times P \times D - 0.059400 \times V \times D \\ &\quad -1.53532 \times 10^{-3} \times P^2 + 3.37864 \times 10^{-4} \times V^2 + 275.13713 \times D^2 \end{aligned} \quad (7)$$

The model F-value of 7145.64 indicates the significance of model. Here is a probability of only 0.01% so that a 'model F-value' being huge might happen owing to noise. The ANOVA table of the quadratic model with other adequacy measures R^2, adjusted R^2 and predicted R^2 are listed in Table 2.10. The adequacy measures R^2, adjusted R^2 and predicted R^2 are in reasonable agreement and are close to 1, which is indicating the higher predictive power of this regression model. Model terms are significant, as indicated by the accompanying p-value for the model being less than 0.05. When comparing the signal to noise ratio, an appropriate precision of larger than 4 is considered preferable. The most significant model terms correlated to the maximum temperature of the plate, according to the ANOVA results, are the consequences of laser power (P), welding speed (V), beam diameter (D), the quadratic effect of the square of laser power (P^2), welding speed (V^2), and beam diameter (D^2), as well as the two-level interaction of laser power and beam diameter ($P \times D$). The other model terms are not significant.

Response surface models that have been designed allow for the identification of the impacts of variables on the response. Figure 2.12 (a) shows the response contour and 3-D surface plot of the effect of the laser power and welding speed on temperature. From the figure, it can be said that the temperature increases when the laser power increases and the welding speed is

kept constant. Similarly, when welding speed increases at a fixed laser power, temperature decreases. With increased power heat input will be increased which can raise the temperature. As welding speed increases, the work piece absorbs less heat as a consequence of a shorter duration of contact among the laser beam and the work piece. Consequently, when welding speed increases, the rate of temperature rise reduces. We can see from figure 2.12 (b), the response contour and 3-D surface plot of the effects beam diameter and laser power on temperature profile. It is observed from the figure, that temperature will increase if laser power increases at fixed beam diameter and decreases if beam diameter increases at fixed laser power. The heat power density per area will be decreased when beam diameter will be increased. Thus, the temperature will be decreased with increase of beam diameter. The response contour and 3-D surface plot of effects of welding speed and beam diameter on temperature has been observed from figure 2.12 (c). It is observed from the figure, that temperature will decrease for both cases if beam diameter increase at fixed welding speed as the heat power density per area will decrease and if welding speed increases at fixed beam diameter as the interaction time of laser beam on work piece decreases, results less heat absorption by the work piece.

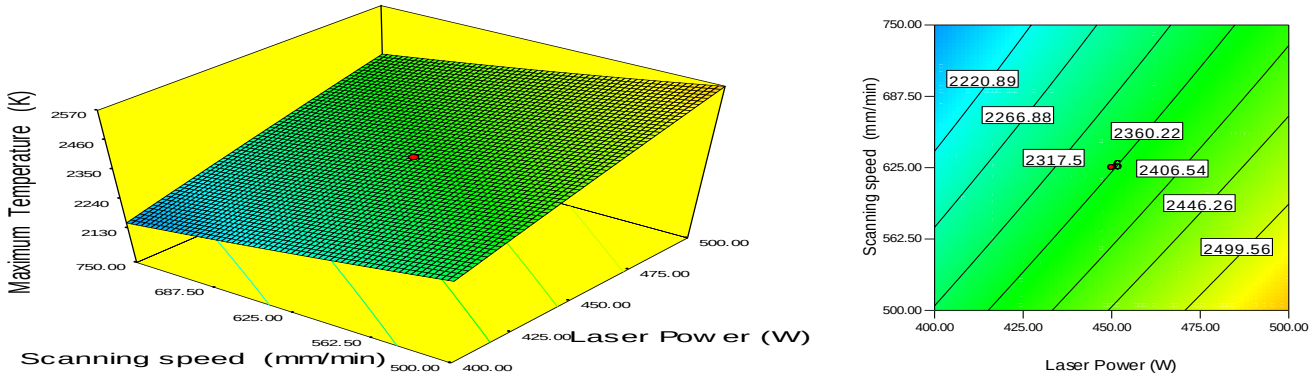

(a) At 0.85 mm Beam diameter

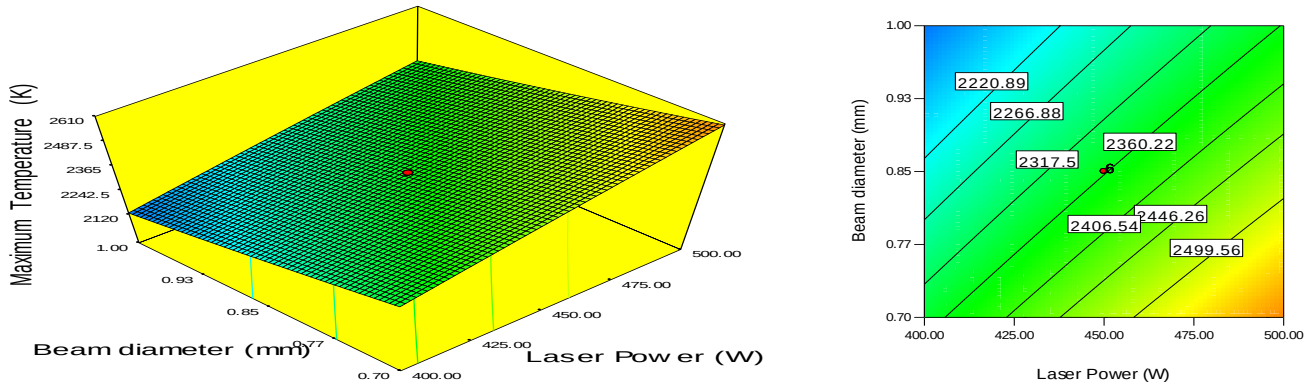

(b) At 625 mm/min Welding speed

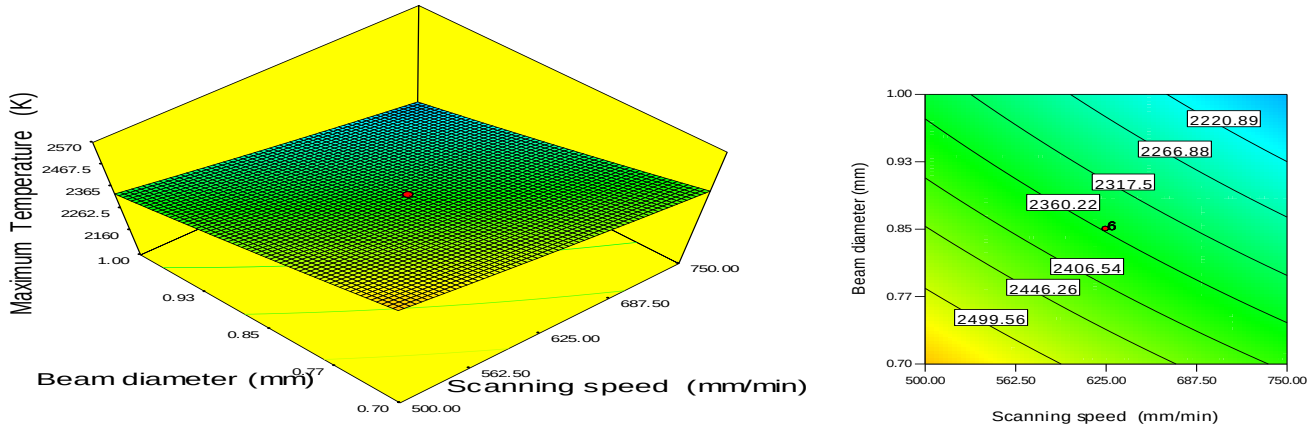

(c) At 450 W Power

Figures 2.12 (a-c): Contours and response surface plot show the effects of input parameters on the Maximum temperature

The aim of this numerical study is to investigate the effect of the process parameters on bead width, depth of penetration and maximum temperature distribution on stainless steel plate during the process of laser welding with fixed plate thickness. The results indicate that bead widths, depth of penetrations and temperatures increase with laser power, but decrease with increase of welding speed. And with increase of beam diameter, bead width increases but depth of penetration and temperature decreases. This FEM model can be used for analyzing the laser welding process when the laser beam scans along straight- line. This study is also important for the further analysis of subsequent stress analysis, thermal distribution analysis for different thickness of material, required for deformation studies.

2.4.3. OPTIMIZATION

The aim of the numerical optimization method, using Design Expert® 7.0 software, is to identify optimum process parameters to achieve a minimum bead width with maximum depth of penetration at comparatively minimal expenses for operation through the use of maximum welding speed and minimum laser power in the region of design. Table 2.11 summarizes the goal, lower and upper limits and importance of each response which are derived from response surface methodology.

Table 2.10 Criteria of numerical optimization

Parameter	**Goal**	**Lower limit**	**Upper limit**	**Lower weight**	**Upper weight**	**Importance**
P (W)	Minimize	400	500	1	1	3
V (mm/min)	Maximize	500	750	1	1	3
D (mm)	is in range	0.7	1.0	1	1	3
T_M (K)	is in range	2052.99	2691.40	1	1	3
B_W (mm)	Minimize	0.5	0.85	1	1	5
D_P (mm)	Maximize	0.6	1.22	1	1	5

Table 2.11 Optimal welding condition based on the criterion

Sl.No	***P*** **(W)**	***V*** **(mm/min)**	***D*** **(mm)**	$\boldsymbol{B_W}$ **(mm)**	$\boldsymbol{D_P}$ **(mm)**	$\boldsymbol{T_M}$ **(K)**	**Desirability**
1	400.00	683.82	0.70	0.522368	0.761008	2306.37	0.607 *selected*
2	400.00	684.87	0.70	0.521899	0.760225	2305.72	0.607
3	400.00	695.37	0.70	0.517316	0.752536	2299.15	0.606
4	400.00	680.97	0.70	0.523766	0.762825	2307.68	0.606
5	400.00	687.26	0.70	0.520957	0.758072	2303.64	0.606
6	424.95	747.80	0.70	0.541412	0.764827	2334.65	0.601

Table 2.12 presents the best welding parameter combinations based on the criteria, stated in Table 2.11, which leads to achieve a minimum bead width with maximum depth of penetration at comparatively minimal expenses for operation through the use of maximum welding speed and minimum laser power in the region of design. To achieve a near minimum bead width with near maximum depth of penetration, the optimum range of laser process

parameters to be maintained are: laser power 400-424.95 W, welding speed 747.80-695.37 mm/min and spot diameter 0.70-1.0 mm.

2.5. Conclusions

1) Maximum temperature at weld zone increases with laser power and decreases with increase of welding speed and spot diameter.

2) Bead width increases with increase in laser power and beam diameter and decreases with increase in welding speed.

3) Depth of penetration increases with laser power and decreases with increase in welding speed and spot diameter.

4) The optimum process parameters for minimum bead width with maximum depth of penetration at relatively low operating (energy) cost and high productivity are also found based on desirability function.

CHAPTER 3

Finite element simulation (anisotropic) and Experimental validation

Chapter 3

3.1. Introduction

Previously we used isotropic thermal conductivity for welding simulations, which is an approximation of the reality where thermal properties are anisotropic in reality. So, to improve our model for achieving more accurate bead geometry compared to experimental bead geometry, we incorporate anisotropic thermal conductivity approach in our model. The influence of welding speed on the geometry of the laser melt pool, namely the penetration depth and bead width are examined and outcomes are compared with experimental melt pool geometry.

Earlier we have done simulations and validate results with published papers. Any simulation needs to be validated with in-house experiments. So, we have decided to design few numbers of experiment with varying process parameters based on the safe operating window obtained based on simulation with isotropic approach, The purpose of the experiment is to investigate the impact of welding speed on the excellence of the butt weld, including bead width, depth of penetration and strength of joint, while other parameters such as laser power and pulse width retained as unchanged. We considered the same process parameters for anisotropic based simulations to acquire a proper validation among simulated and experimented investigation. In case of isotropic simulations, we considered power, weld speed, and beam diameter as process parameters but for experimental study we were restricted to a fixed beam diameter due to constraint of laser welding machine. For experimental and anisotropic investigations pulse width instead of beam diameter is considered to assess the predictability of isotropic and anisotropic simulation against experimental results. However, we are capable of validate only bead geometry and mechanical properties are not predictable from the simulation model. After obtaining the optimum condition for based on bead width and depth of penetration, the quality of butt joints along with base material have been assessed through tensile test, microstructure observations, microhardness test and XRD for better understanding the process.

3.2. Finite Element Simulation

Finite element simulations are developed to observe the temperature changes at weld interface and obtain the melt pool geometry such as depth of penetration and bead width. Normally, material melting will take place on laser direct metal deposition techniques, like laser cladding, laser fusion welding, and laser surface melting, necessitate accurate oversight in order to attain the desired microstructure, stress distribution, thermal stress distortions, and

other essential response parameters. To achieve any level of optimization, modeling such procedures is a crucial step [32]. Nevertheless, because marangoni and buoyancy-driven convection dominate melt pool flows, modeling these processes is challenging. Accurate melt pool geometry prediction necessitates the use of intricate computational fluid dynamics models. However, these modes are more complex to compute and call for more experience [32]. A few researchers have accounted for melt pool convection in their models using the isotropic and anisotropic improved thermal conductivity technique, which simplifies and expedites the modeling process. They discovered that the melt pool geometry may be precisely predicted by the anisotropic increased thermal conductivity technique [32]. In light of what they discovered; an anisotropic enhanced thermal conductivity approach has been employed in this present study. These developed anisotropic enhanced thermal conductivity approach simulations results are compared with experimental results. Merely half of the model is taken into account for FE simulation owing to material symmetries, which helps to shorten the simulation interval. For the purpose of achieving the study's objectives, this idealization of the model fits the issue well [15]. In case of building the model some physical parameters are used that are given in following Table 3.1. Temperature dependent thermal properties are used, namely, thermal conductivity, specific heat and density and those are listed in Table 3.2. The initial temperature of work piece is considered as 300 K. A changing surface heat flux with tiny time increments is used to represent the laser beam. The simulation duration and RAM need are reduced by using a 3-D free tetrahedral mesh utilizing an inconsistent mesh design. Extremely small meshes are employed throughout the laser beam's path because of the significant heat flux involved in the laser path. In other areas of the plate, coarser meshes are employed. Figure 3.1 (b) shows the mesh used for finite element simulation.

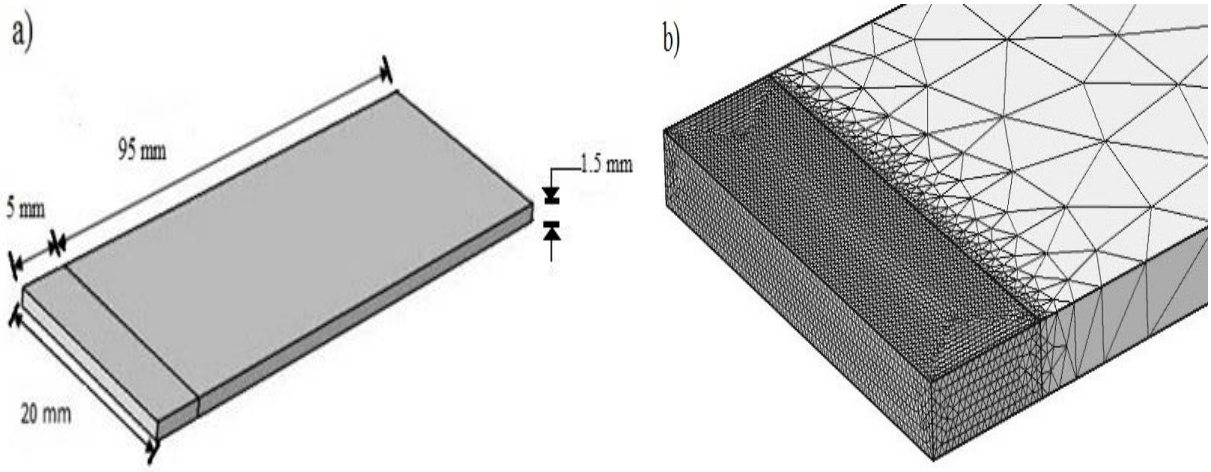

Figure 3.1 (a) One half of the symmetrical sample, (b) Finite element mesh used for modelling

Table 3.1 Physical parameters and their units

Material Property	**Symbol**	**Value**	**Unit**
Ambient Temperature	T_0	300	K
Solidus Temperature	T_S	1658	K
Liquidus Temperature	T_L	1773	K
Latent heat of fusion	L_f	500	kJ/kg
Emissivity	ε	0.7	
Heat transfer coefficient	H	10	W/m^2K

Table 3.2 Temperature dependent thermal properties of 2205 Duplex stainless steel [16]

Temperature (K)	**Thermal conductivity (W/m. K)**	**Specific heat (J/kg. K)**	**Density (kg/m^3)**
250	15	500	7860
500	18	500	
750	20	500	
1000	25	600	
1250	27.5	620	
1500	30	700	
1750	35	750	
1950	45	850	
2250	55	1000	
2500	65	1250	

3.2.1. Governing equation and boundary conditions

The following equation for three-dimensional heat conduction is implemented to simulate heat transmission in laser welding, which controls the temperature distribution. [32].

$$\frac{\partial}{\partial x}(k_{xx}(T)\frac{\partial T}{\partial x})+\frac{\partial}{\partial y}(k_{yy}(T)\frac{\partial T}{\partial y})+\frac{\partial}{\partial z}(k_{zz}(T)\frac{\partial T}{\partial z})+Q=\rho(T)C_P(T)(\frac{\partial T}{\partial t}) \quad (1)$$

Concerning the standard heat transfer and isotropic modified thermal conductivity methods, $k_{xx} = k_{yy} = k_{zz} = k$. Thermal conductivity values are three and five times higher than their initial values in the isotropic modified thermal conductivity models. The isotropic modified thermal conductivity *k' can* be expressed by Eq. (2). $\rho(T)$ is the density as a function of temperature in kg/m^3, $C_P(T)$ is the specific heat as a function of temperature in J /kg*K, and Q is the surface heat flux in W/ m^2.

$$k' = \alpha\, k \quad (2)$$

here k is the standard isotropic thermal conductivity value at the corresponding temperature and α is the isotropic improvement factor which is outlined as

$$\alpha=\begin{Bmatrix}1 & if\ \ T<T_{liquidus}\ \ \&\,T_{solidus}\\ Multiplying\ \ factor & if\ \ T>T_{liquidus}\end{Bmatrix} \quad (3)$$

Similarly anisotropic enhanced thermal conductivity $k_{ii}^{"}$ is defined by Eq. (3).

$$k_{ii}^{"}=\alpha_{ii}^{"}\,k \quad (4)$$

where k is the standard isotropic thermal conductivity value at the corresponding temperature, *ii* denote the spatial co-ordinate and α_{ii} is the anisotropic improvement factor for the respective spatial co-ordinate, which is defined as [32]:

$$\alpha_{ii}=\begin{Bmatrix}1 & if\ \ T<T_{liquidus}\ \ \&\,T_{solidus}\\ Multiplying\ \ factor & if\ \ T>T_{liquidus}\end{Bmatrix} \quad (5)$$

The transient thermal analysis governed by Eq. (1), is written in FEM, in the matrix form as:

$$[C]\{\dot{T}\}+[K]\{T\}=\{Q(t)\} \quad (6)$$

To simulate a transfer of the energy to the work piece, the surface heat source model is used. The heat source used in this present study can be expressed as [17, 18]:

$$Q_v=Q(x,y,z)=\frac{3P(1-R)}{\pi abd}\exp\left(-\frac{3x^2}{a^2}\right)\exp\left(-\frac{3y^2}{b^2}\right)\exp\left(-\frac{3z^2}{d^2}\right) \quad (7)$$

where *P* is the power [W] of the incident laser beam and R is the reflectivity. The parameters *a* and *b* are taken to be equal to the radius [mm] of the laser beam, *d* is the max depth [mm]. The natural convection and radiation from the material's exposed surfaces to the surrounding air create the material's cooling phase.

The following is an expression for the convective boundary condition:

$$q_{conv} = h(T_{st} - T_o) \tag{8}$$

here *h* is the heat transfer coefficient, that is considered as 10 W/m^2**.** K [16], T_{st} is the sheet metal surface temperature and T_0 is the ambient temperature, which is considered as 300K.

The following is an expression for the radiation boundary condition:

$$q_{rad} = \varepsilon\sigma({T_{st}}^4 - {T_o}^4) \tag{9}$$

ε is the emissivity, which is taken as 0.7 [16] and σ is the Stefan Boltzmann constant (5.6703×10^{-8} W/m^{2}K^4).

Throughout the welding procedure, the temperature in the fusion zone rises over the material's melting point. In order to accurately describe laser melting processes, consideration of latent heat effects is necessary. For the purpose of modeling solid-liquid phase change problems, numerous numerical approaches have been designed. The latent heat effects are incorporated using two methods such as effective heat capacity method and enthalpy method. The enthalpy method is most common method. This approach enables treatment of latent heat effects directly as a function of temperature. Effective heat capacity method requires very precise control of time stepping to ensure change of phase [32]. A seamless switch among phases occurs surrounding the phase change temperature, within the interval $\Delta T = T_L - T_S$, when a phase transition function α (T) is implemented. A mushy zone with heterogeneous material qualities exists during this time frame. More abrupt switches ought to occur with decreasing intervals. There are differences in the material properties for the liquid and solid phases. To provide a seamless crossover from solid to liquid, these parameters are paired with the phase transition function. Thus, the heat capacity method is used to incorporate a phase change phenomenon in FE simulation. The heat capacity of the material is expressed as:

$$C_p = C_{p,solid}.(1-\alpha(T)) + C_{p,liquid}.(\alpha(T)) + L_f \frac{\partial\alpha}{\partial T} \tag{10}$$

$$\alpha(T)=\begin{cases}1 & T \geq T_l \\ \dfrac{T-T_s}{T_l-T_s} & T_s \leq T \leq T_l \\ 0 & T \leq T_s\end{cases} \qquad (11)$$

For pure solid, $\alpha(T)=0$, and for a pure liquid, $\alpha(T)=1$. Latent heat of material is considered as L_f=500 KJ/Kg. The material solidus (T_s) and liquidus (T_l) temperature are considered as 1658 K and 1773 K respectively [16].

3.3. Experimental Investigation

3.3.1. Experimental set up

We have done six numbers of butt weld experiments of 2205 Duplex stainless steel sheets, each sized 100×20×1.5 mm at CSIR-CMERI Durgapur on JK-600 HP Nd: YAG Laser. The pulsed Nd:YAG laser is operated at 1064 nm wavelength. The experimental setup for the current study is photographed and is displayed in Figure 3.2. The work pieces are placed on the metal plate of the holding fixture and both ends are clamped to prevent misalignment between the parts to be welded in butt joint geometry. The technical specifications of the used Laser device are tabulated in table 3.3. The ranges of parameters which are taken for the present experiment are tabulated in table 3.4. After experiments, we have done the tensile strength test of welded samples along with base material to find out the strength of welded joints and the base material. We have also investigated the microstructure of base material and welded samples. Hardness also has been measured for base material and the welded samples.

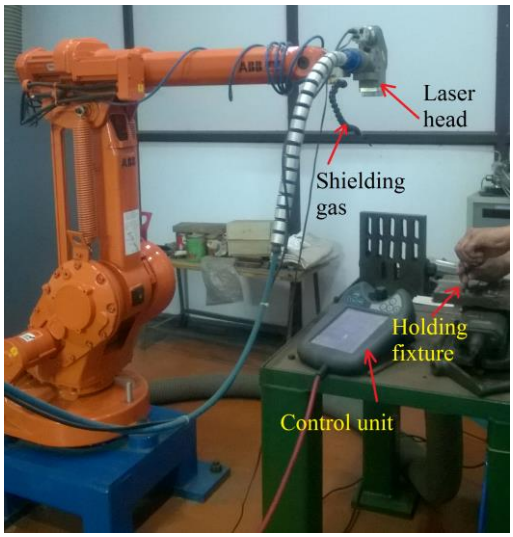

Figure 3.2 Experimental set-up for laser welding

Table 3.3 Technical specifications of JK-600 HP Nd: YAG Laser

PARAMETERS	VALUES
Maximum average power at Laser (W)	600
Typical Power at Work Piece (W)	500
Maximum Peak Power (kW)	10
Energy (J)	10-100
Frequency (Hz)	20-50
Pulse Width (ms)	0.2-20
Beam quality (mm.mrad)	28
Scanning Speed (mm/s)	1-3000
Focal Length (mm)	80, 100, 120, 200, 300
Shielding gas at flow rate	Argon gas at 7 L/min

Table 3.4 Parameters considered for experimental investigations

PARAMETERS	VALUES
Wavelength	1064 nm
Beam diameter	0.75 mm
Shielding gas at flow rate	Argon gas at 7 L/min
Frequency	25 Hz
Power	425 W, 525 W
Weld speed	3.5 mm/sec, 4.25 mm/sec, 5 mm/sec, 6 mm/sec, 7mm/sec
Pulse width	4 ms, 5 ms

3.3.2. Materials and Methodology

Base material was cut in a size of $10mm \times 10mm \times 1.5mm$ and all of the welded samples were cut in a size of $10mm \times 3mm \times 1.5mm$. Then the base material and cross section of welded samples are mounted by metallographic mosaic machine followed by polishing through emery sheets of grit range fineness from 100 to 2000, continued with light disc cloth polish with alumina solution.

A combination of 30 ml Glycerin, 30 ml HCL and 10 ml HNO_3, the solution named Glycergia, was used as an etchant to reveal the microstructure. Each welded sample consist base material, HAZ and Weld zone. The microstructure of welded samples and base metal were observed by LEICA DM 2700 M (type: DFC450, input: 12 V/350 mA) optical

microscope and JEOL 6360 scanning electron microscope. Chemical composition of base material 2205 duplex stainless steel is tabulated in table 3.5.

Table 3.5 Chemical composition of base material 2205 duplex stainless steel

C %	Si %	Mn %	P %	S %	Cr %	Ni %	Mo %	Cu %	N %	Co %	Ti %	Nb %	V %	B %	Sn %	Ca %	Fe %
0.028	0.6	1.39	0.029	0.011	22.65	5.19	3.32	0.186	1.18	0.057	0.012	0.046	0.116	0.0043	0.0074	0.0004	66.3

The base material microstructure, as acquired, is depicted in Figure 3.3 and exhibits an equivalent phase ratio of austenite and ferrite accompanied by an extended grain shape. Ferrite phase is seen in the black region and austenite phase in the white region. This illustration illustrates how the continuous ferrite phase matrix surrounds the stripe type austenite phase, leaving no additional precipitates in its wake.

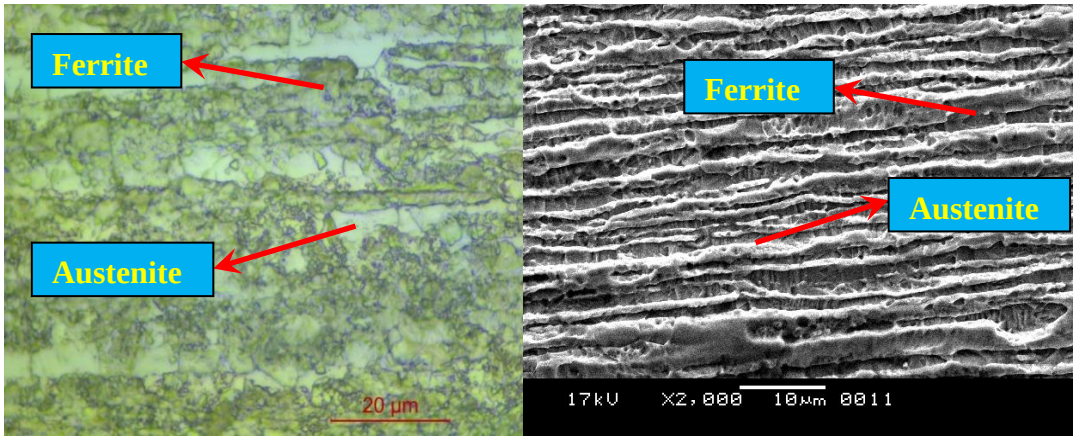

Figure 3.3 Base material microstructure

Tensile tests were performed for basic material along with welded samples on INSTRON-8801(with strain rate $10^{-3}/s$). For basic material, size100×20×1.5 mm, a large strain zone is present in the stress-strain curve, demonstrated in Figure 3.4 (a). It also shows the maximum tensile strength of 870 MPa before it tears. Figure 3.4 (b) is the sample on which tensile test was performed. Yield strength of the material was 700 MPa and the tensile strain at break was 37.8 %, from this we can say that the material has good ductility. The load and strength at break point were 18.73 kN and 590.08 MPa respectively. Young's modulus of 267.5 MPa has been calculated from stress-strain curve.

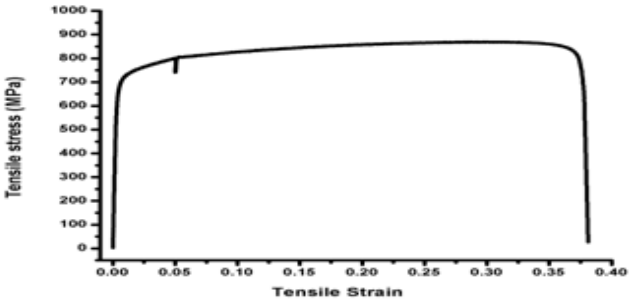

(a)

(b)

Figure 3.4 Tensile test result performed for basic material (a) stress-strain curve, (b) sample of basic material

In order to determine the hardness profiles, microhardness measurements are conducted for base material and all welded samples joints. The microhardness measurements are carried out using Vickers Hardness tester- AMT- X7FS fitted with a diamond indenter considering 50 g-f load and a dwell time of 20 s. Micro hardness distribution of base metal has been shown in figure 3.5. From the figure it is seen that the average hardness of base material is 280 HV. Hardness depends on grain size. According to Hall-Petch equation,

$$\sigma_s=\sigma_0+kd^{-1/2} \quad (12)$$

Where σ_s is yield strength (MPa), σ_0 is constant, k is constant, and d is grain size (mm). It is deduced that smaller the grain size the higher is the yield strength. Meanwhile the relationship between hardness and yield strength is described by Tabor empirical formula which can be given by,

$$HV= C \times \sigma_s \quad (13)$$

Where HV is hardness (Vickers scale), C is a constant and σ_s is yield strength (MPa). So the relationship between hardness and grain size can be written as,

$$HV= C (\sigma_0+kd^{-1/2}) \quad (14)$$

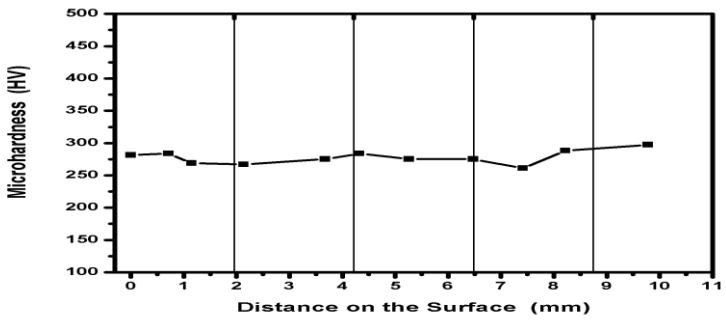

Figure 3.5 Micro hardness of base material

3.4. Results and Discussion

3.4.1. Validation of simulated weld bead geometries with experimental study

3.4.1.1. Temperature distribution for different welding speed (simulation model)

The temperature contour of weld pool and mushy zone for different scanning speeds are shown in Figure 3.6 (a-d), where 1673 K-1773 K is considered as the temperature range of the mushy zone. In this work, the weld pool is defined as plate heated to the material liquidus temperature (1773 K) and above.

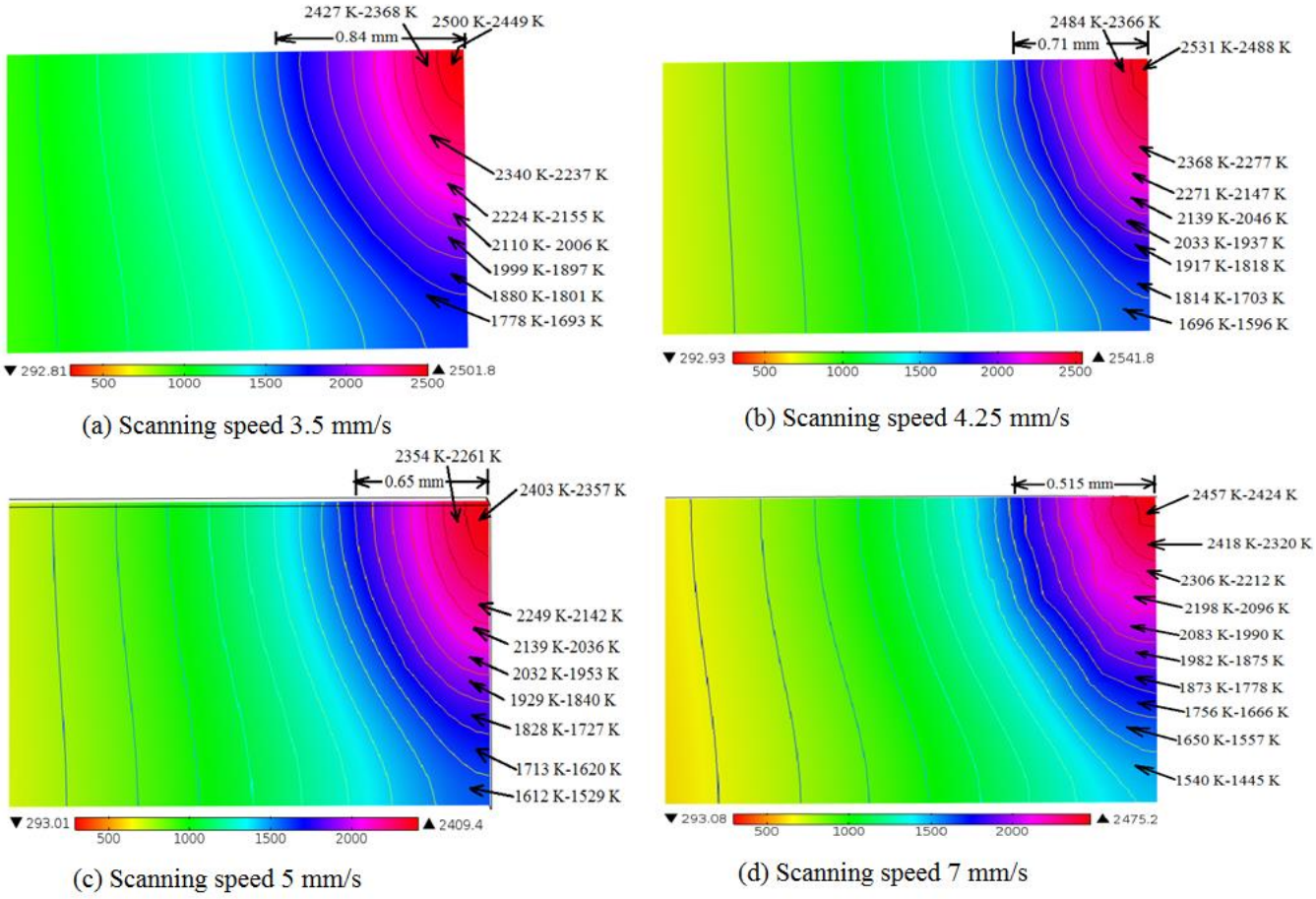

Figure 3.6 Simulated temperature contour and distributions for different scanning speed

The dimensions of the weld pool (breadth and depth of weld), which spans the laser beam path and passes through the plate thickness, are computed based on temperature values and distances along the x and z axes. It is observed from these results that the dimension of weld pool decreases with increase in scanning speed. From these figures, it is observed that the temperature at the interface of the two plates reaches a maximum range of 2550 K – 2450 K, which indicates the attainment of boiling point (~2500 K) of the material resulting in a tiny

amount of material removal on the top surface of the plate. The substrate damage can be seen from micrographic views of experimental samples.

3.4.1.1.1. Effect of Welding Speed on Microstructure

The welding quality varied with different welding speed. It can be presented that distance between beam center increases and overlapping factors Q_f decreases when the speed will increase remaining other parameters constant. Q_f (%) can be calculated by,

$$Q_f = [1 - \frac{\left(v/f\right)}{(D + vT)}] \times 100 \quad (15)$$

Where v is welding speed, f is frequency, D is beam diameter and T is pulse duration. Overlapping factors for each experiment with different speeds has been tabulated in table 3.6, which is 81.7 % in speed 3.5 mm/s and declined to 64 % in 7 mm/s speed. Depth of penetration and bead width both depends on welding speed. With increase of speed, overlapping factor decreased and thus average heat input will be decreased that result less penetration and bead width. In the weld, the degree of dilution and cooling rate are said to be determined by the quantity of heat input. Limited melting between the surface and the heat source during the welding process caused a higher cooling rate, which in turn led to insufficient penetration. Changes in the welding settings can control the heat input, which is crucial in determining the shape of the junction. The two most remarkable factors influencing the heat input among these are the laser welding speed and the laser beam overlapping factor. According to the following equation, the heat input for this investigation was determined.

$$\frac{P}{\pi(\frac{D-Q_f}{2})^2 \times v} \quad (16)$$

Where P is laser power, D is beam diameter, Q_f is overlapping factor, v is welding speed. The above equation shows that raising the overlapping factor and lowering the laser welding speed will result in a rise in the amount of heat input on the work piece.

The depth of penetrations and bead widths were determined from microstructures of weld cross-sections using Image J software and are given in table 3.6. No visible cracks were observed during and after welding. There were no significant grain size changes observed at the base regions for all weld samples. With increase in scanning speed, DOP and Bead width both were decreasing due to less interaction time between heat source and weld surface even

when power increases from 425 W to 525 W, both DOP and Bead width were continuously decreasing, this was also due to reducing pulse width from 5 ms to 4 ms.

Table 3.6 Variation of overlapping factor, depth of penetration and bead width for different welding speed

Exp. No.	Frequency (Hz)	Pulse width (ms)	Speed (mm/s)	Power (W)	Beam diameter (mm)	Overlapping factor (%)	Depth of penetration (mm)	Bead width (mm)
1	25	5	3.5	425	0.75	81.7	1.16	1.45
2	25	5	4.25	425	0.75	77.9	1.15	1.39
3	25	5	5	425	0.75	74.1	1.12	1.2
4	25	5	7	425	0.75	64.3	1.04	1.14
5	25	4	7	525	0.75	64	0.7	1.05
6	25	4	6	525	0.75	68.9	1	1.12

The optical micrograph of welded samples taken on optical and scanning electron microscope are given in figure 3.7 and 3.8, showing weld zone, base and HAZ. At weld zone, in figure 3.7 and 3.8 due to repeated recrystallization, the maximum deformation and extremely fine grains were produced. The weld zone in figure 3.8, of almost all weld samples featured a narrow and regular shape. All fusion zone microstructures of optical micrographs revealed the presence of both ferrite and austenite. The dark region shows ferrite portion and lighter region shows austenite portion. The whole weld zone was in the liquidus phase when the temperature hit the liquidus point during welding. Ferrite was the first phase to develop directly from the liquid at a temperature just below the melting point when solidification began. Austenite (γ) has developed when the temperature progressively dropped to about 900 ^{0}C. After cooling, δ ferrite will change into α ferrite, thus both the ferrite and austenite phases will persist. The cooling rate increased as a result of the discrepancy between the ambient temperature and the greatest temperature reached in the weld zone [30]. The predominant ferrite structure in the weld zone resulted from the diffusional change to austenite phase being restricted upon cooling [33].

$L \rightarrow L+\delta \rightarrow \delta+\gamma \rightarrow \alpha+\gamma$

Ferrite to austenite ratio at weld zone for all samples can vary. In some experiments this ratio has been decreased and in some it has been increased. From the view of Weld-HAZ-Base junction the occurrence of a significant modification of the grain size is clearly visible. An amazing transformation was seen at the high temperature heat impacted zone near the fusion

line, where there was confirmation of the austenite phase's early breakup across the area. very close from weld zone. Optical micrographs, taken at higher magnification showed that the corresponding structure for all weld samples was made up of small sized globular grains except experiment number 2 and 4 where elongated and comparatively coarse grains were formed. The grain boundaries at weld zone are quite thick that reveals there are some carbide precipitates over the boundaries. The grain orientation roughly followed the heat flux direction during welding. From the junction of weld-haz-base, it is seen that HAZ portion was very narrow. From SEM micrographs, for experiment number 5, there is a deep undercut at weld zone from both sides. This can be due to exceed the optimum range of power, speed and pulse width. For other weld samples, a slightly under tapped top surface has been found at weld zone which is common problem for laser welding as immense energy is directly applied to the top surface. For these welding, laser beam was starts from one end of the weld line to other. If a minimum distance can be maintained between the starting point of beam and weld line then these types of problems can be overcome to some extent. Variation of process parameters can also be the reason.

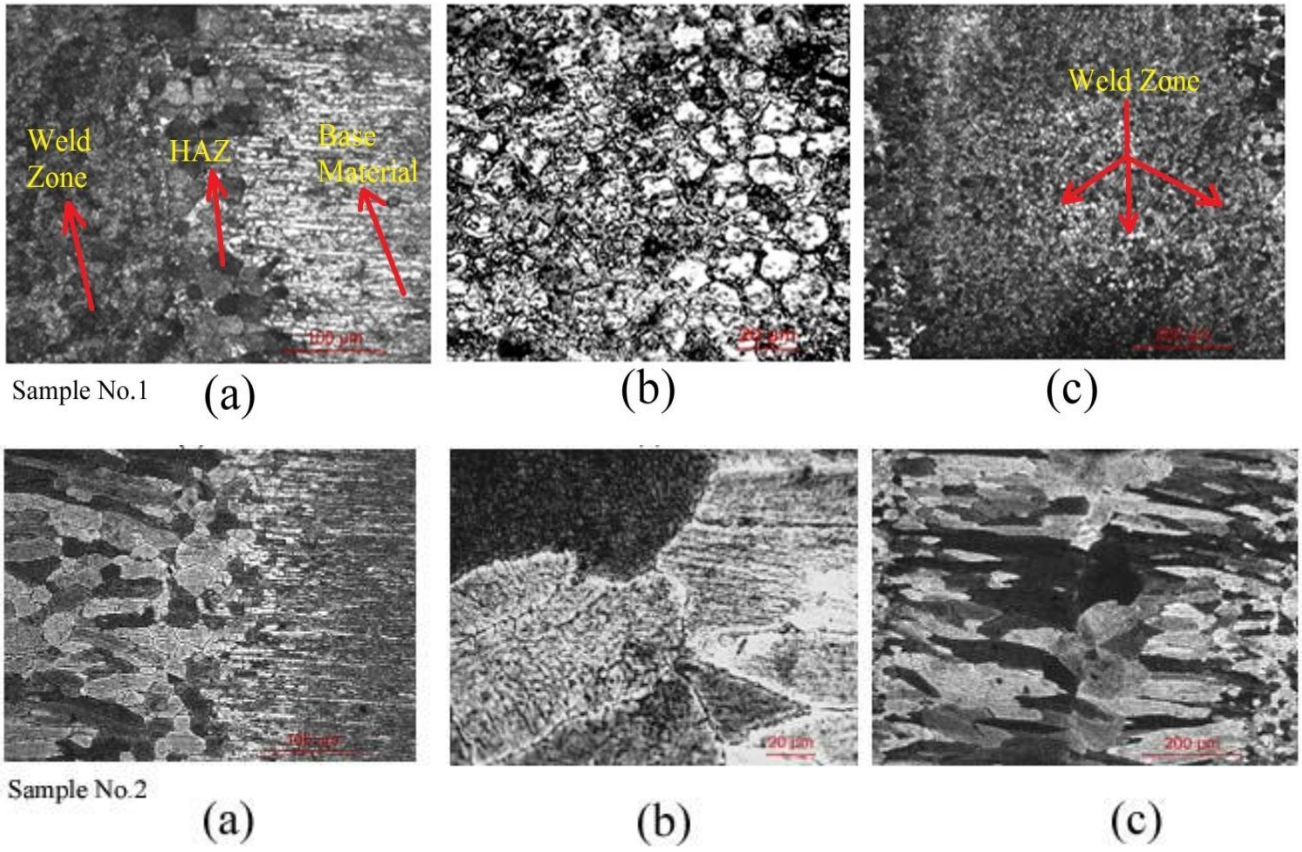

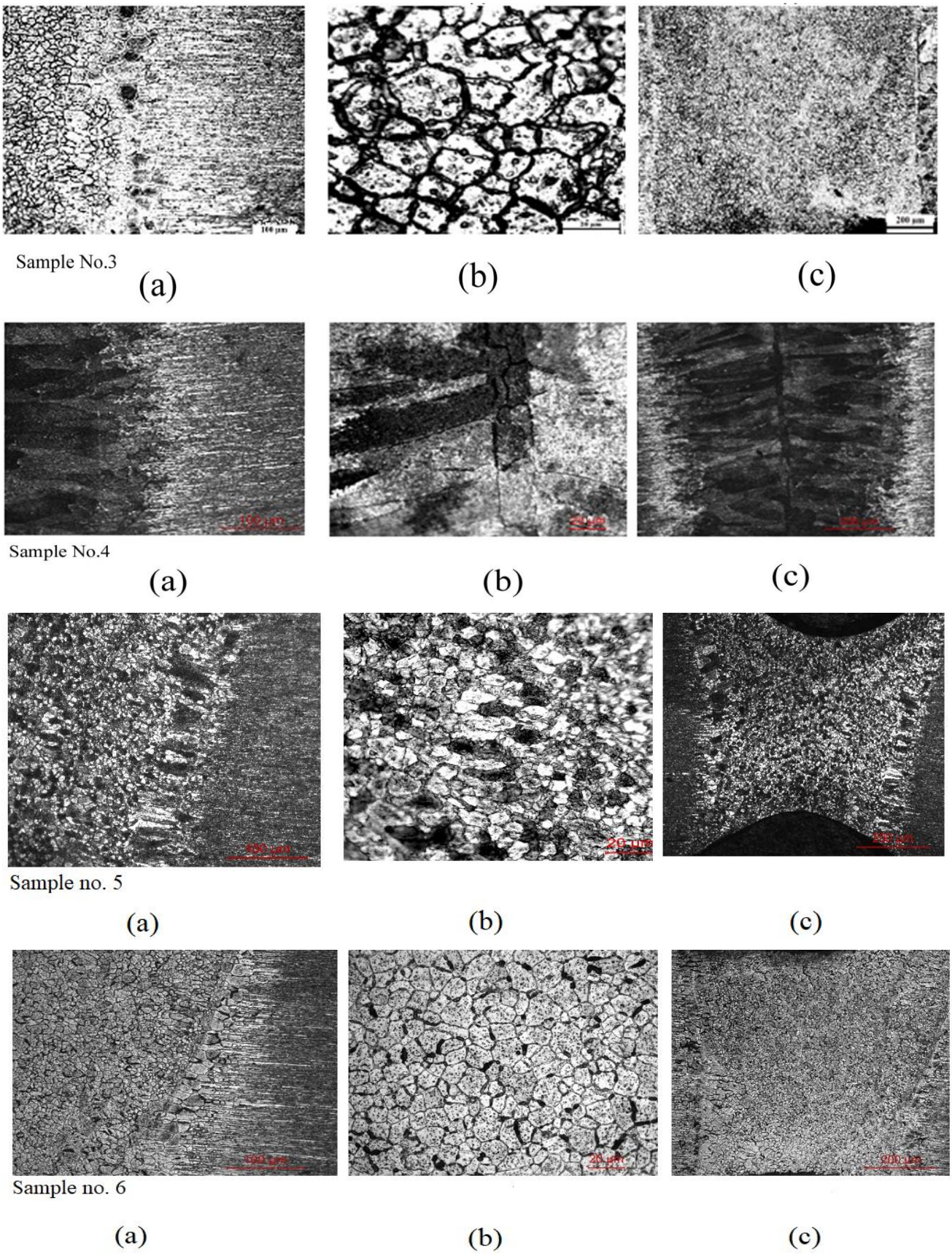

Figure 3.7 Optical micrographs of all welded samples: (a) Weld-HAZ-Base junction, (b) Weld zone (higher magnification) and (c) Fusion zone

Next zone to it was heat affected zone, shown in figure 3.8 (b), which is between weld zone and base material. In HAZ, a lower temperature beyond the fusion zone was reached. In this instance, grain size increased as a result of recrystallization and grain expansion. Fusion or mixing zone is a transition region from the weld metal to HAZ. Here also the grain boundaries are thick due to carbide precipitation, except experiment number 5 where grains cannot be identified clearly. Some voids have been formed in grain boundary for experiment number 6. Figure 3.11(a) shows the full welding.

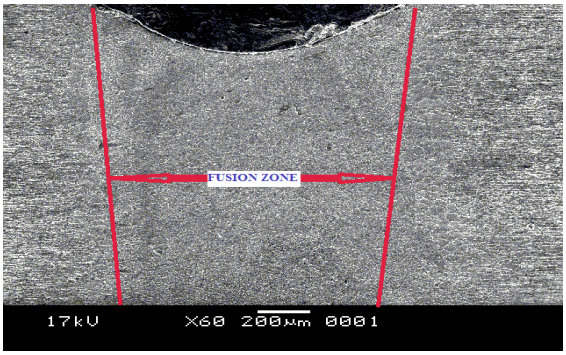

#1 (a)

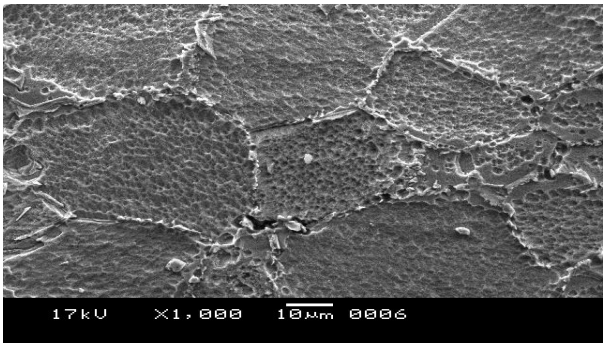

(b)

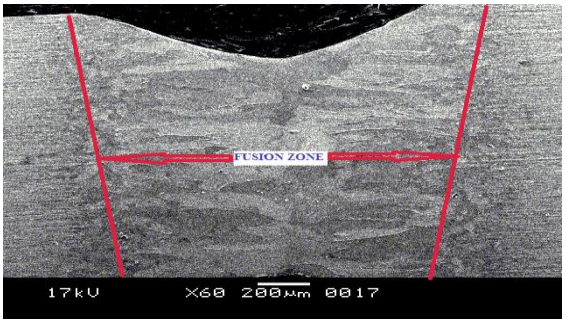

#2 (a)

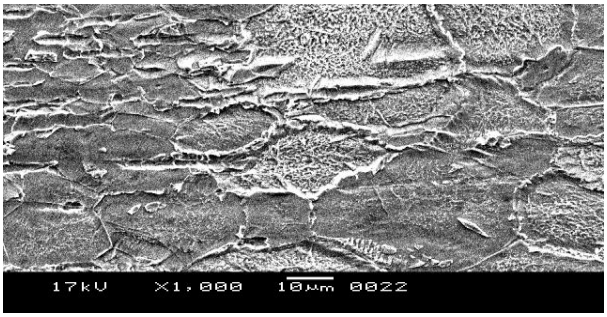

(b)

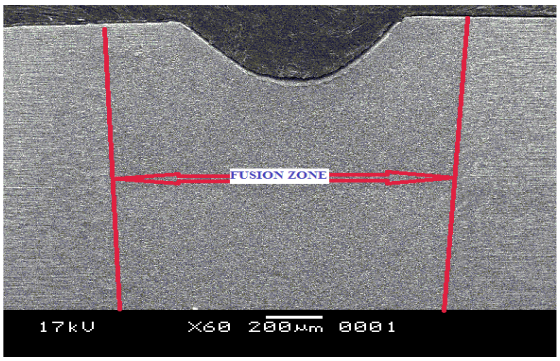

#3 (a)

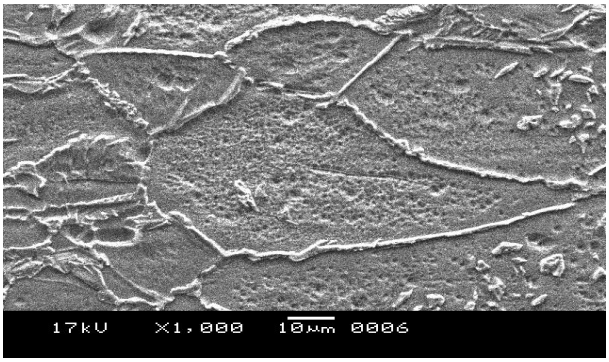

(b)

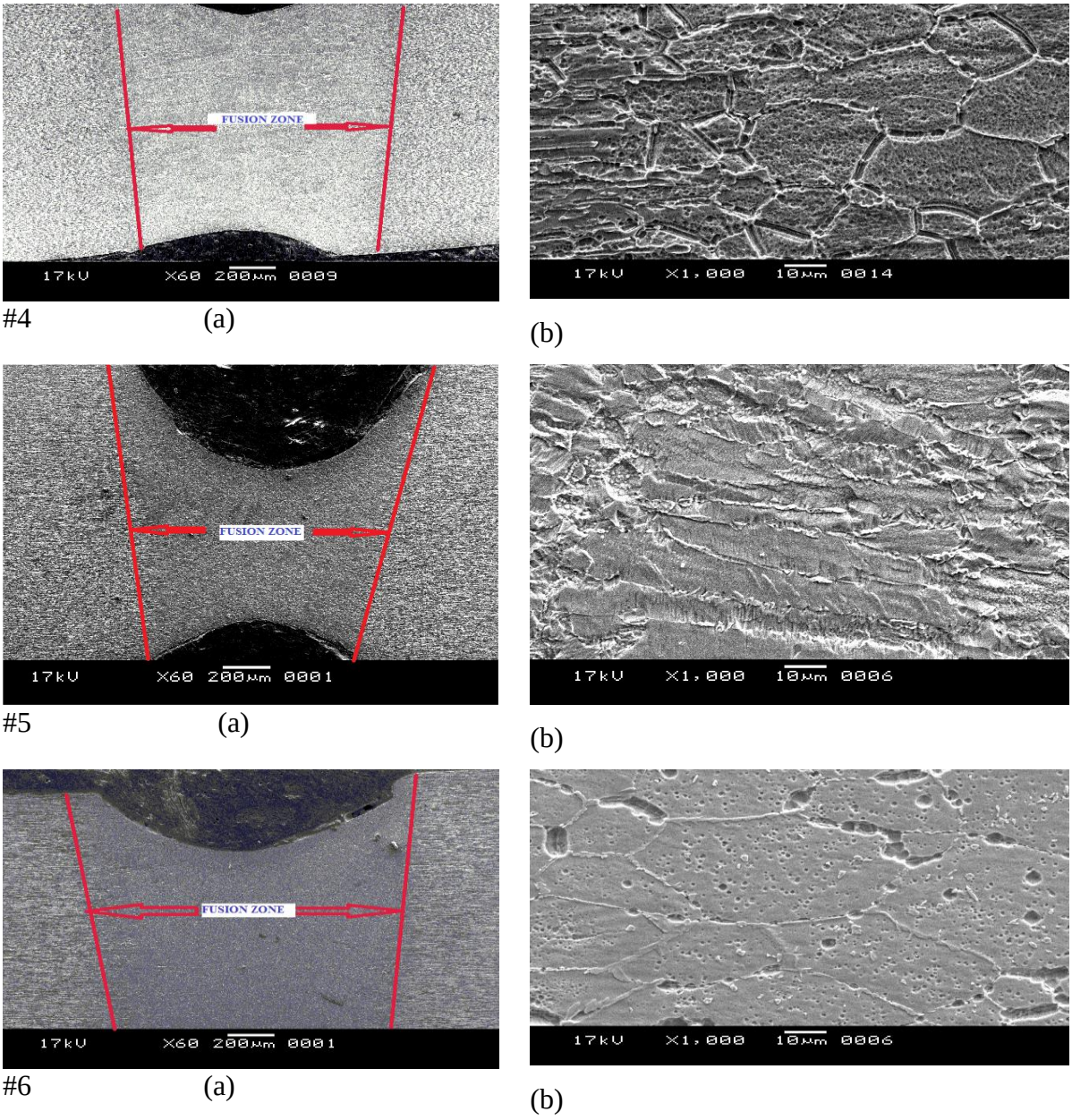

#4 (a) (b)

#5 (a) (b)

#6 (a) (b)

Figure 3.8 SEM micrographs of all welded samples: (a) Full welding, (b) HAZ zone

Validation of the effect of scanning speeds for both experimental and numerical study, on weld bead geometry is studied and summarised in Table 3.7. The weld bead geometry of sample 5 and 6 reveals poor joints, so we considered first 4 samples for validation and further characterizations. The results are achieved from the present numerical models are found to be in good agreement with experimental results. As can be seen from Table 3.7 that depth of penetration and bead width, for both experimental and numerical study, decreases with increase of scanning speed since, with increase of speed, interaction time between the laser beam and the work piece decreases, resulting in less amount of heat is delivered to the plate.

Table 3.7 Laser input parameters and the validation of weld bead dimensions

Exp. No.	Pulse Width (ms)	Speed (mm/s)	Power (W)	From Experiment Depth of Penetration (mm)	From Simulation Depth of Penetration (mm)	Error %	From Experiment Bead Width (mm)	From Simulation Bead Width (mm)	Error %
1	5	3.5	425	1.16	1.31	-0.1293	1.45	1.68	-0.1586
2	5	4.25	425	1.15	1.2	-0.0435	1.39	1.42	-0.0215
3	5	5	425	1.12	1.12	0	1.2	1.3	-0.0833
4	5	7	425	1.04	0.97	0.06731	1.14	1.03	0.09649

3.4.1.1.2. Effect of welding speed on tensile strength

Tensile testing of welded joint and base material has been conducted in Instron 5582 Machines according to ASTM E-8 using rectangular specimens. All welded samples were cut in a size of 200×12.5×1.5 mm. The effect of welding speed on tensile strength of the welded sample is studied and discussed. Table 3.8 summarises the input parameters, the experimental results of mechanical properties of the welded sample. Beam diameter is kept constant at 0.75 mm. Mechanical characteristics like ultimate strength, yield strength, and strength at breaking point advance with scanning speed until they reach a specific point, at which point they begin to decrease. When a medium welding speed is employed, this behaviour is seen. It is noted from the table 3.8 that for a laser power (P=425W); pulse width (P_w=5ms); increasing the welding speed (V=3.5 - 5 mm/s) increases the mechanical properties. This may happen due to degradation of the material due to high energy input. That is why mechanical properties initially improves with scanning speed and the trend differs when a relatively higher laser welding speed (V=7 mm/s) is used. In this case, mechanical properties degrade for same laser power (P=425W) and pulse width (P_w=5ms). This could occur because inadequate energy leads to insufficient heat transfer, insufficient penetration, and improper material mixing, all of which may outcome in a weak weld [21]. In case of sample 5 and 6 we use higher power (525 W) with welding speed of 7 and 6 mm/s keeping the pulse width at 4 ms and both experiments offer poor strength than others. The fracture location is at weld zone for all

experiment. Regarding the responses listed in table 4.3, the suitable combination of laser power, welding speed and pulse width to acquire improved tensile strength is 425 W, 5 mm/s and 5 ms, respectively. Figures 3.9 shows tensile stress-strain curves of the welded samples with steady power (425 W) and pulse width (5 ms) for different welding speed. Figure 3.10 shows the samples used for the tensile testing.

Table 3.8 Laser input parameters and the experimental results of mechanical properties of the welded sample

Exp No.	Process Parameters			Response Parameters						Fracture location
	P (W)	V (mm/s)	P_w (ms)	Ultimate Tensile strength (MPa)	Yield strength (MPa)	Elongation (%)	Young's modulus (MPa)	Load at break point (kN)	Strength at break point (MPa)	
1.	425	3.5	5	780	600	7	261.26	14.55	739.55	Weld
2.	425	4.25	5	810	650	13.4	255.26	14.7	747.6	Weld
3.	425	5	5	845	700	16.2	265.9	15.33	806.6	Weld
4.	425	7	5	655	590	0.84	259.2	11.48	594.15	Weld
5	525	7	4	575	500	0.6	256.4	10.63	547.9	Weld
6	525	6	4	590	510	0.65	248.8	11.24	569.1	Weld

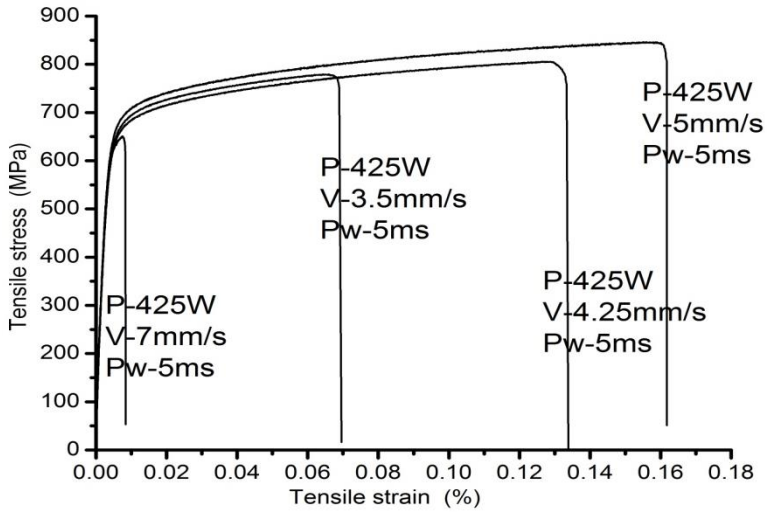

Figure 3.9 Tensile stress-strain curve of the welded samples

Figure 3.10 Photographs of samples used for the tensile testing

The maximum tensile strength and elongation of welded samples has been decreased compared to the base material, so it can be said that the weldability was degraded for these experiments. The fracture location was at weld zone for all experiment. With increase of welding speed from 3.5 mm/s to 5mm/s, maximum tensile strength and elongation has been increased respectively, when speed exceed 5 mm/s and reached 7 mm/s both maximum tensile strength and elongation has been decreased. So, among these six experiments we can conclude, welding at 5 mm/s speed with power, pulse width and beam diameter at 425 W, 5 ms and 0.75 mm respectively, gives better strength and elongation.

3.4.1.1.3. Effect of welding speed on microhardness

Equation 14 defines that hardness will increase if grain size decrease and vice versa. A decline in weld speed raises average power, which raises heat input and lowers cooling rate. This makes it possible to get the fusion zone's softer microstructure with reduced hardness. As a result of the micro structural alterations brought about by an upsurge in weld speed, it is possible to deduce from these data that the hardness in the fusion zone would rise.

Micro hardness distributions from the center of weld zone to base for six numbers of welded samples have been shown in figure 3.13. For all experiments, the weld region exhibited high hardness values than base material for all parameters. The hardness values in base metal for welded samples are observed to be nearly constant throughout the material. The average hardness values of base for welded samples are near 300 HV. For some of the welded samples a sharp fall of hardness value has been observed at region between base and weld zone. This region is heat affected zone. Microstructure of weld zone consist small grains, so here hardness will be high. Although for present experiments average hardness values nearly 380 HV, at weld zone for all welded samples with different weld speed, are found except experiment number 5. For this case average hardness value is 337 HV at weld zone which is

not so high like other experiments. From the graph for experiment number 5, it is seen that hardness of base and weld zone are nearly same. In spite of coarse grain size, at HAZ also hardness is high for some weld samples. This can be due to the carbide precipitates at grain boundaries of weld as well as Haz zone. The best part is after experiment also, the hardness and microstructure of base material have not been changed [20, 35].

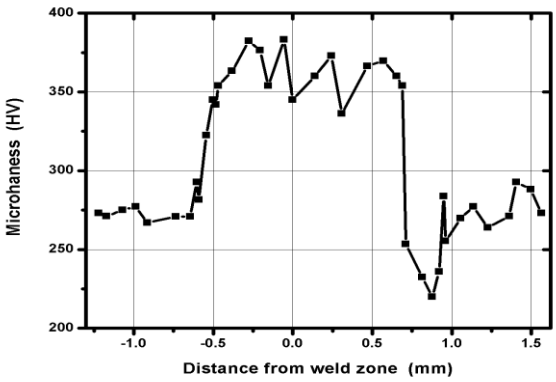

Experiment No. 1

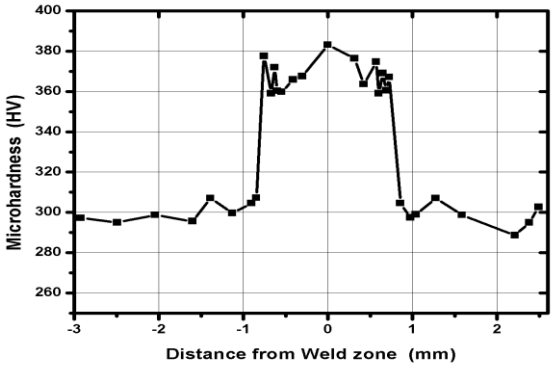

Experiment No. 2

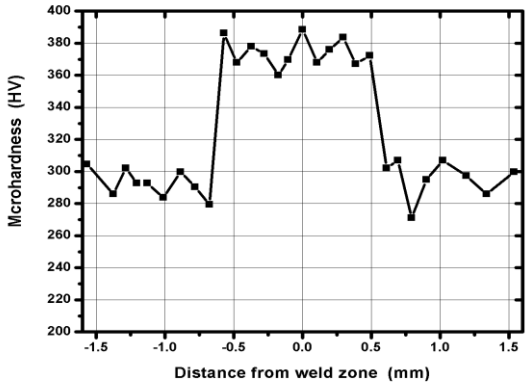

Experiment No. 3

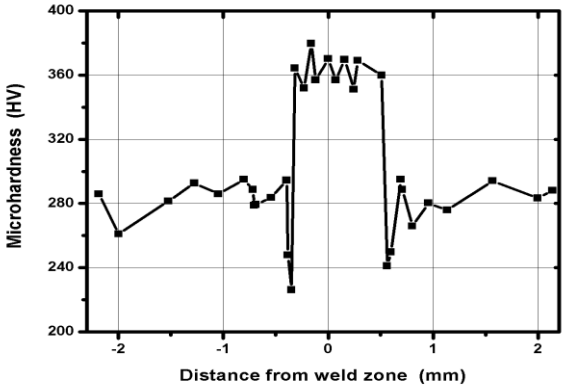

Experiment No. 4

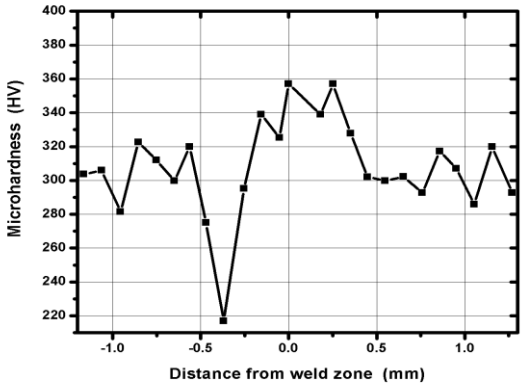

Experiment No. 5

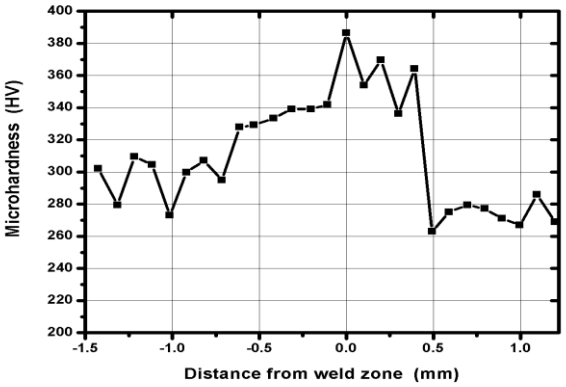

Experiment No. 6

Figure 3.11 Micro Hardness from weld centre to base for four numbers of experiments

3.4.1.1.4. Effect of welding speed on XRD

Figure 3.12 (a-d) shows X-Ray diffraction pattern for all welded samples. The plot for all welded samples showed there is ferrite content is relatively higher and subsequently, austenite content is lower. This implies that heat input, a consequence of the laser welding process, has a notable influence on the austenite volume fraction [16]. Since laser welding produces less heat input, the austenite content has decreased and the ferrite content has increased as a result. Support for this comes from the fact that the low heat input during laser welding leads to an increase in both solidification and cooling speeds. In slow cooling rate welding, the transformation from ferrite to austenite takes place very quickly by reason of slow cooling rate on account of high heat input might resultant microstructure includes the majority of austenite. When it comes to welding, quick cooling rates owing to minimal heat input may produce weld metal with a reduced austenite content than slow cooling rates [23, 34].

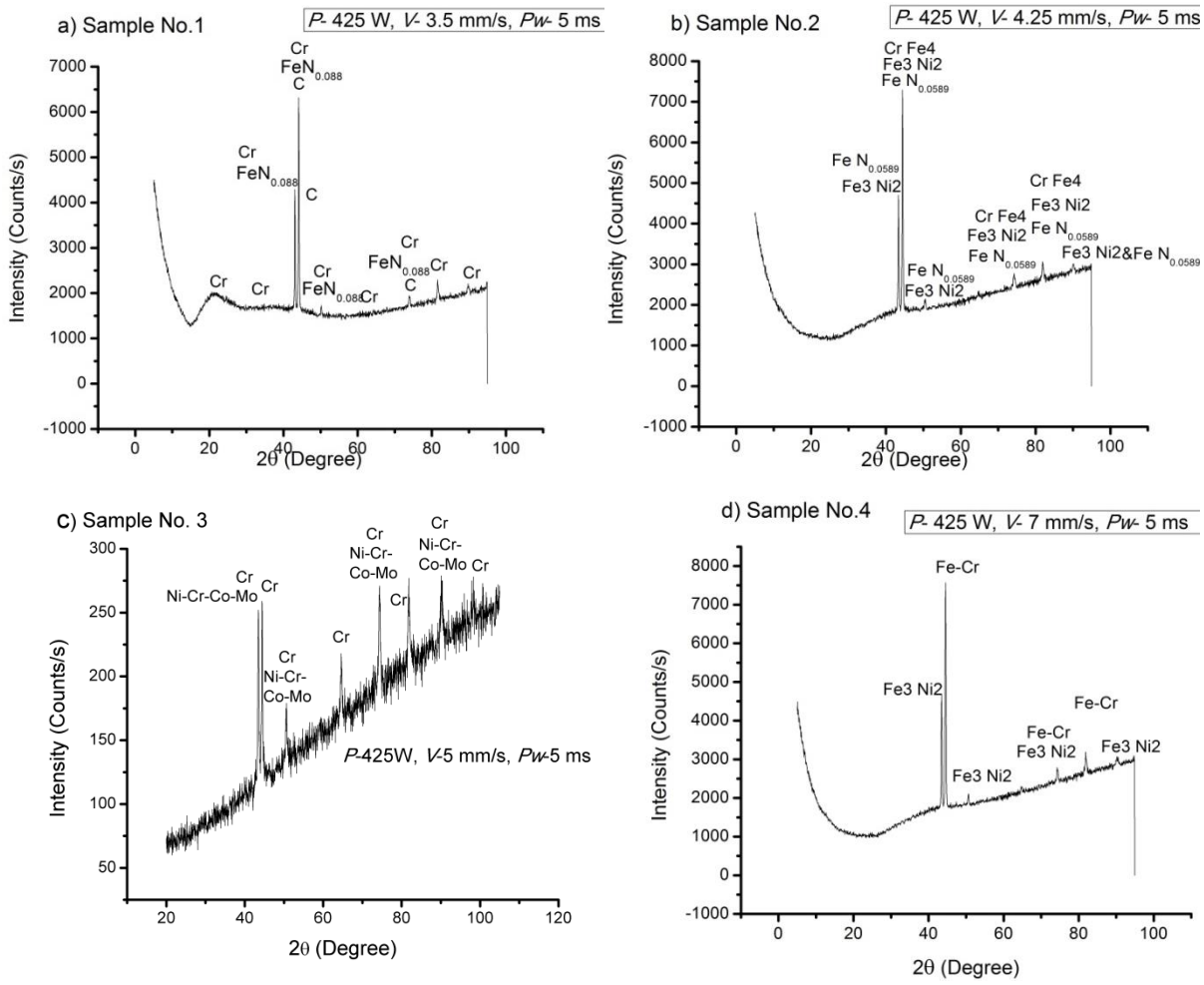

Figure 3.12 X-ray Diffraction pattern of all weld samples

3.5. Conclusion

The aim of this experimental study is to investigate effects of welding speed and other parameters on the quality of the butt weld while laser power and pulse width are kept as constant. Tensile characteristics, microstructure, and microhardness have all been evaluated in relation to the butt joint and base material quality. Anisotropic increased thermal conductivity technique is used to predict the impact of welding speed on laser melt pool shape, i.e., penetration depth and bead width, and the results correlate well with the experimental data. The following conclusions can be drawn from above investigations:

1. The butt joints without cracks and porosities are obtained for 2205 duplex stainless steel using laser beam welding method. The weld bead geometry i.e., depth of penetration and bead width increases with the decrease in scanning speed.

2. The mechanical properties such as ultimate strength, yield strength and strength at breaking point improve with scanning speed. However, due to lack of penetration, poor heat

transfer and poor mixing of materials, the lowest mechanical strength is obtained to sample number 4 which involves higher scanning speed.

3. Microstructure analysis indicates that scanning speeds have remarkable effect on fusion zone during laser beam welding. Microstructures show significant changes in the fusion region for sample no. 1 to sample no. 4. It is demonstrated that the high heat input could contribute the coarse grain size and high content of the austenite phase during laser welding.

4. Microhardness continuously decreasing from the welded zone (350-380 HV) to the unaffected area (275-280 HV) due to changes in metallurgical phase constituents and formation of more amounts of intermetallic compounds inside the melt pool. In addition, formation of bainite structure because of the higher cooling rate is also one of the reasons to have higher hardness in the fusion zone.

CHAPTER 4

Experimental study on weld pool dimensions and mechanical properties of laser-welded 2205 duplex stainless steel with multiobjective optimization

Chapter 4

4.1. Introduction

Initially optimisation of laser process parameters was done based on best bead geometry (depth and width) as objective function. FE simulated results were used to predict bead geometry for a given set of laser process parameters. The quality of the welded joint was assessed based on desired bead geometry. Desired mechanical properties of the welded joint have not been used in objective of the optimisation. But with the observations obtained from tensile testing of optimum graded welded joints it is found that those fail to qualify sufficient strength. Hence it is necessary to plan for optimisation of laser process parameters including the desired mechanical properties as another objective function along with bead geometry. So, it will be in the class of multi-objective optimisation problem. For optimisation input-output relationship between laser process parameters (speed, power, pulse width) and mechanical properties (Ultimate strength, yield strength) is necessary. This relationship is established using Response surface method based on experimental results already available. Once the relationship is obtained multi-objective optimisation is done to identify optimum process parameters to ensure qualified bead geometry and mechanical properties.

Weld quality are primarily determined by the strength of joints, along with flexibility or % of elongation of welded materials, where these two main properties are extremely influenced by the ratio of depth of penetration and bead width of fusion zone. Bead width can categorize the heat affected zone (HAZ), less HAZ defines superior joint quality whereas depth of penetration has quite first-rate control on strength of weld joints, as less penetration can cause deprived joints follow-on poor strength which makes weld joints brittle and with enhancement of penetration, weld joints turn out to be stronger ensuing weld joints which can tolerate much load for quite a long time and be ductile in nature. For current investigation, the consequences of laser welding process parameters together with laser power, scanning or welding speed alongside pulse width were analytically scrutinized upon the depth of penetration, bead width, ultimate tensile strength and elongation for laser butt welding method of duplex 2205 stainless steel. We carried out these laser welding experiments on the basis of central composite design with response surface methodology for constructing numerous mathematical regression models to determine the key possessions of process parameters along with their impressions on depth of penetration, bead width, ultimate tensile strength and elongation of laser welded butt joints of 1.5 mm thick 2205

duplex stainless-steel sheets. Accuracy of mathematical regression models were evaluated to ensure the competence by using analysis of variance for formulating correlations linking process parameters and response parameters. Moreover, an evaluation was prepared among the envisaged and authentic outcomes. The actual intention was to build up high-quality welds by means of least deficiency together with elevated penetration intensity taking on arithmetical schemes. Earlier, identifying process parameters were unavoidable in case of each latest creation for achieving the favoured provisions in welded joint, which as well consumed a soaring extent of period. So, in favour of conquering this predicament, plentiful of optimization techniques has been practiced a route for establishing the correlation involving the key parameters and response parameters. For past few times, design of experiment (DoE) methods turned out to be incredibly positive towards forming such optimizations. With the process of alternating laser process parameters, such as power, pulse width and scanning speed, it is possible to procure optimum parameters in fulfilment of achieving superior quality weld joints with minimal expenses. The microstructure of the weld zone, HAZ, and base zone are examined under an optical microscope (Leica DM 2700 M).

4.2. Experimental procedure

In this study, a three factor five-level central composite design is employed for the experimental design. The statistical software Design-Expert 7.0 is used to construct the design matrix, and response surface methodology is also applied using the same software. 2205 duplex stainless steel sheets with dimensions of 100 mm × 20 mm × 1.5 mm are used for butt welding in the study. The experiments are conducted at the Central Mechanical Engineering Research Institute (CMERI), Durgapur, using a pulsed Nd:YAG Laser, which has a maximum average power of 600 W and operates at a wavelength of 1064 nm. Figure 4.1 shows the schematic diagram of the laser butt welding process, and Figure 4.2 displays the setup, including the JK-600 HP Nd: YAG Laser. The work piece is placed on the holding fixture and clamped at both ends to prevent any misalignment during the welding process. In experiments, the process parameters such as power, scanning speed, and pulse width are varied while maintaining a constant laser frequency of 25 Hz and beam diameter of 0.75 mm. Argon gas is utilized as a shielding gas at a flow rate of 7

L/min. Prior to the welding process, the samples are cleaned with acetone to eliminate any oil contamination or oxide film.

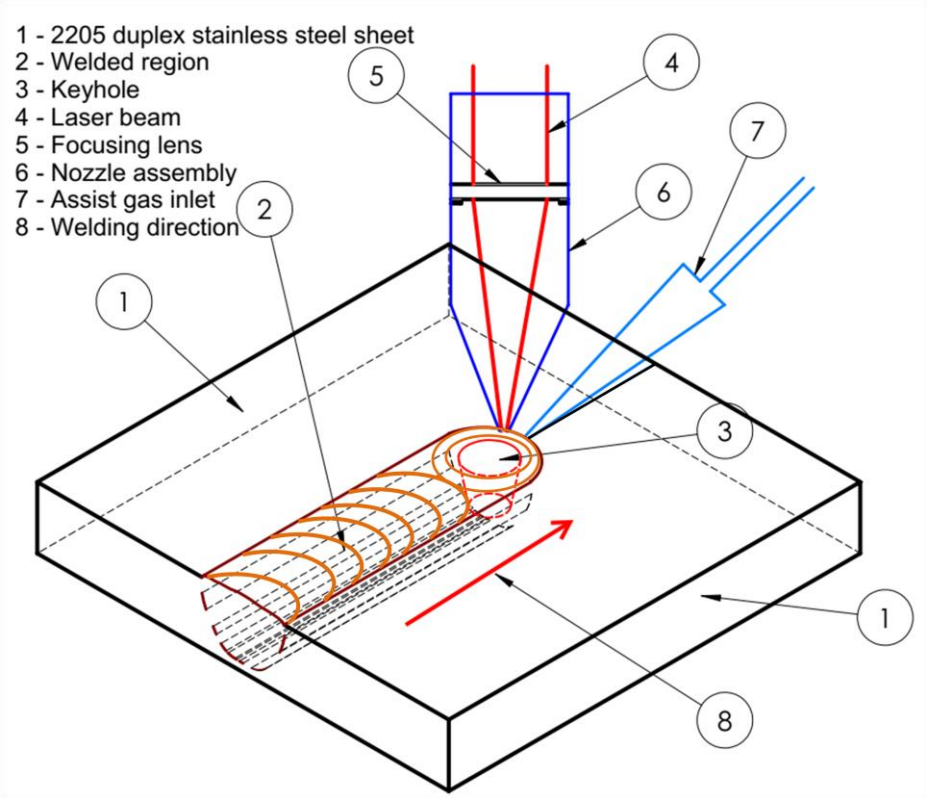

Figure 4.1 Schematic diagram of the laser butt welding process

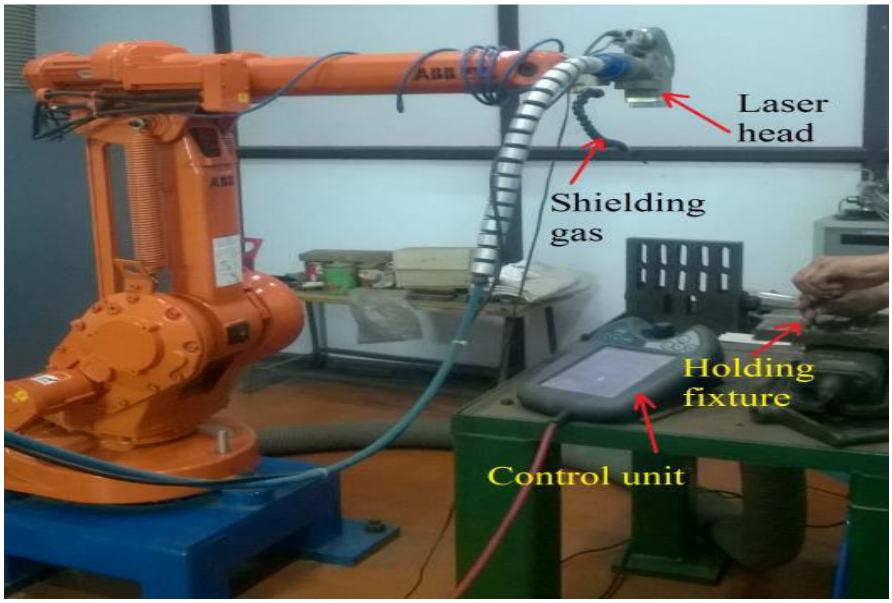

Figure 4.2 Experimental set-up for laser welding

The Leica DM 2700 M optical microscope is used to examine the microstructure, depth of penetration, and bead width of the fusion zone. The welded samples are engraved to a size of 10 mm × 3 mm × 1.5 mm and then mounted by a metallographic mosaic machine. The samples are then polished using emery sheets ranging in fineness from 100 to 2000 grit, followed by a light cloth polish with alumina solution. Glycergia, a solution consisting of 30 ml Glycerin, 30 ml HCL, and 10 ml HNO3, is used as an etchant to reveal the microstructure. Tensile test is performed following the ASTM E8 standards and are tested using an INSTRON-8801 (Force rating = 100 kN) with a strain rate of 10^{-3}/s. Figures 4.3 and 4.4 demonstrate the metallographic mosaic mounter and INSTRON-8801 set up, while Figure 4.5 (a-b) illustrates the dimensions of the tensile test specimen as per ASTM E8 standards and the butt-welded specimen for the tensile test.

Figure 4.3 Mounted samples for microstructural inspection after welding

Figure 4.4 Experimental set up of INSTRON- 8801 for tensile test

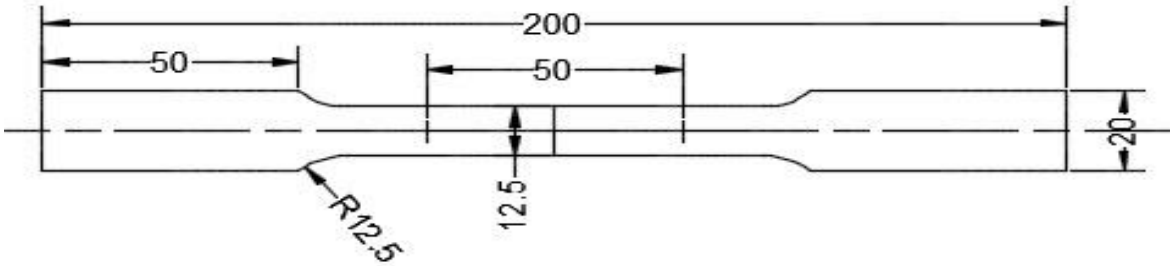

(a)

(b)

Figure 4.5 Tensile test sample (a) Dimensions (in mm) as per ASTM E8 standard, (b) Actual view of welded sample

4.3. Response surface methodology (RSM) and design matrix

Response surface methodology comprises mathematical and statistical techniques that aid in developing empirical models and optimizing them. Conducting experiments and applying regression analysis can result in a model that predicts the response against independent input variables. Assuming that all variables are measurable, the response surface can be expressed in the following manner.

$$y = f(x_1, x_2, x_3, ...x_n) \pm \varepsilon \quad (1)$$

where, y is the response which is a function of independent parameters $(x_1, x_2, x_3, ...x_n)$ and ε is the regression error. In order to derive an approximative relationship between a true response and several design parameters from the data collected from observations of the procedure, the response surface approach is applied through a series of planned experiments.

Table 4.1 contains the process parameters, including their notation, units, ranges, and low/high levels. A central composite design matrix is used with three factors (laser power, scanning speed, and pulse width) and five levels (-α, -1, 0, +1, +α). The response surface method is applied to

generate regression equations and statistical response plots. Experiments are conducted based on this matrix, and the process parameters and their corresponding responses are listed in Table 4.2.

Table 4.1 Process parameters and their units and limits

Parameter	**Notation**	**Unit**	**Low actual**	**High actual**
Laser power	P	W	400	450
Pulse width	P_W	ms	4.8	5.2
Scanning speed	V	mm/s	4.5	5.5

Table 4.2 Design matrix with experimentally obtained responses

Sl. No.	Process Parameters			Responses			
	Power, P (W)	Pulse width, P_W (ms)	Scanning speed, V (mm/s)	Bead width, B_W (mm)	Depth of penetration, D_P (mm)	UTS, T_S (MPa)	Elongation, E_L (%)
1	425	4.6	5	1.315	1.417	791	5.4
2	425	5	5	1.331	1.429	814	5.51
3	475	5	5	1.387	1.491	932	13.3
4	400	4.8	5.5	1.281	1.377	655	0.81
5	400	5.2	4.5	1.329	1.431	849	7.3
6	425	5	5	1.323	1.421	849	6.21
7	425	5	5	1.327	1.427	855	7.74
8	425	5	6	1.311	1.414	685	1.35
9	400	4.8	4.5	1.297	1.403	796	5.43
10	450	5.2	5.5	1.351	1.449	876	8.69
11	425	5.4	5	1.355	1.453	885	8.92
12	400	5.2	5.5	1.319	1.421	762	4.81
13	450	4.8	4.5	1.371	1.474	895	11.1
14	425	5	4	1.347	1.449	889	9.24
15	450	4.8	5.5	1.339	1.443	848	6.79
16	450	5.2	4.5	1.368	1.469	912	11.3
17	375	5	5	1.293	1.391	689	2.27
18	425	5	5	1.321	1.419	831	5.7
19	425	5	5	1.326	1.424	846	6.17
20	425	5	5	1.335	1.431	833	5.81

4.4. Results and Discussion

4.4.1. Microstructure analysis and tensile strength of the base material

Figure 4.6 (a-b) displays optical and SEM images of the microstructure of the base material DSS 2205. It can be observed that the base material microstructure has an equivalent phase ratio of austenite and ferrite. The white and black regions correspond to the austenite phase and the ferrite phase, respectively. The stripe type austenite phase, which is surrounded by the continuous ferrite phase matrix with no other precipitates, is also noticeable. The mechanical properties of the base material are specified in Table 4.3, and the stress-strain curve for the base material is demonstrated in Figure 4.7. As reported in the table, the maximum ultimate tensile strength and elongation are 870 MPa and 37.8%, respectively.

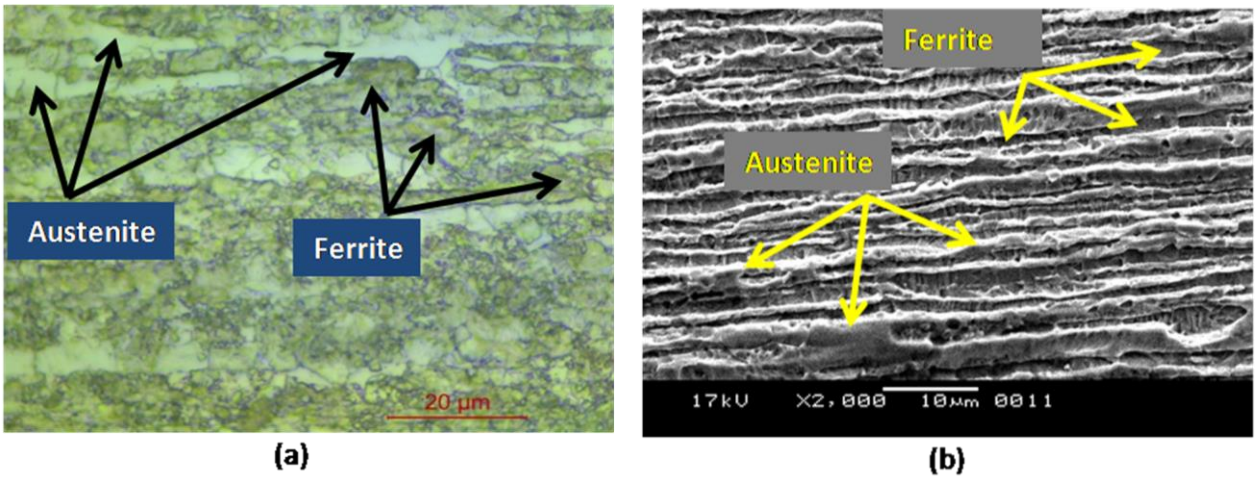

Figure 4.6 Base material microstructure: (a) optical micrograph image, (b) SEM micrograph image

Table 4.3 Mechanical properties of the base material

UTS (MPa)	Yield Strength (MPa)	Elongation (%)
870	700	37.8

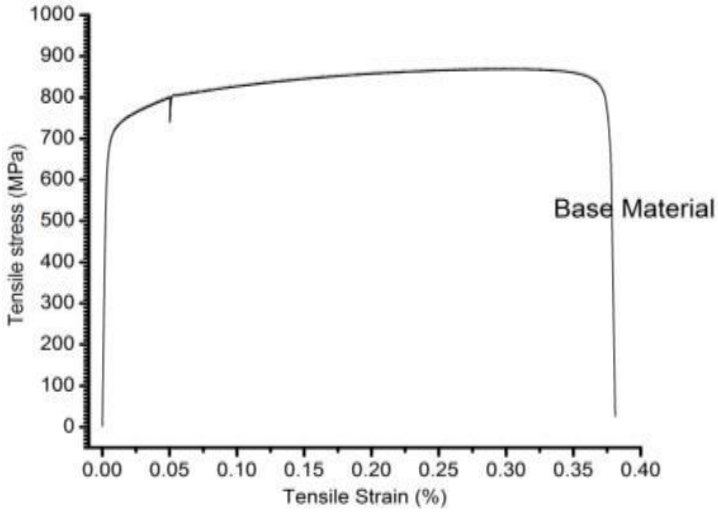

Figure 4.7 Stress-strain curve of the base material

4.4.2. Microstructure analysis and tensile strength of the welded samples

The microstructure of the weld zone, heat affected zone (HAZ), and base zone are examined under an optical microscope after the welding process and are presented in figures 4.8 (a-f). Figure 4.8 (a) shows that the weld zone of the weld sample is narrow and regular in shape. Figure 4.8 (b) displays the interface between the weld zone and HAZ. The repetitive recrystallization and high deformation during the welding process resulted in very fine and small globular grains in the weld zone, while elongated and coarse grains are formed gradually towards the fusion line due to the orientation of grain following the heat flux direction. A narrow HAZ width is observed from the weld-HAZ junction.

The temperature in HAZ is lower than that of the fusion zone. This area experienced an increase in grain size due to recrystallization and grain growth. The fusion zone serves as a transition region from the parent metal to HAZ. Figure 4.8 (c) shows a closer view of the weld zone with broad grain boundaries due to carbide precipitation. No voids, porosity or visible cracks are found in the fusion zone after welding. Figure 4.8 (d) depicts the HAZ-base junction interface, where no significant change in grain orientation is observed in the base zone after the welding process. The high-intensity heat from the laser heat source did not significantly impact the base region.

The micrographs of the weld zone showed both ferrite and austenite, as seen in figure 4.8 (e). The dark areas indicate ferrite, while the lighter areas indicate austenite. A significant change in grain size is observed in the heat affected zone near the fusion line, as shown in figure 4.8 (f). The austenite phase began to decompose in this region close to the weld zone. The depth of penetration and bead width are measured using Image J software and are shown in Figure 4.9.

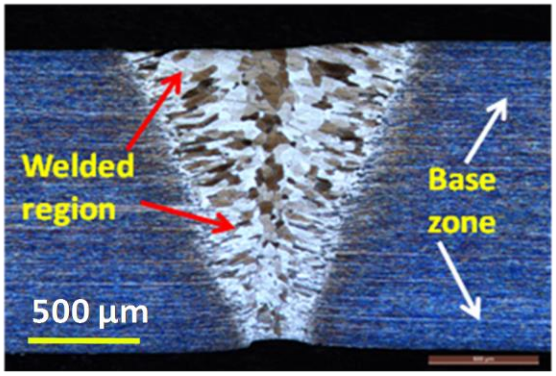

(a) welded zone of the sample

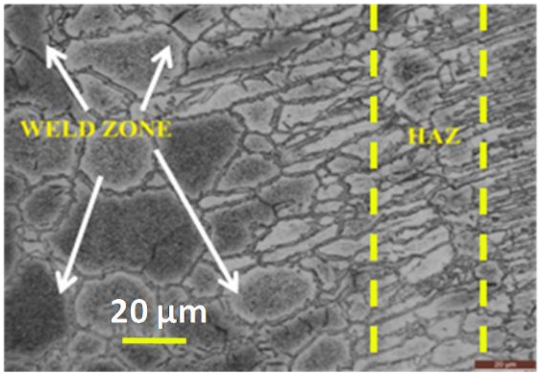

(b) Interface between the welded zone and HAZ

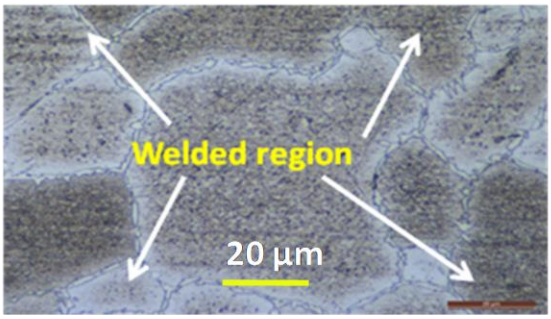

(c) Closer view of the welded zone

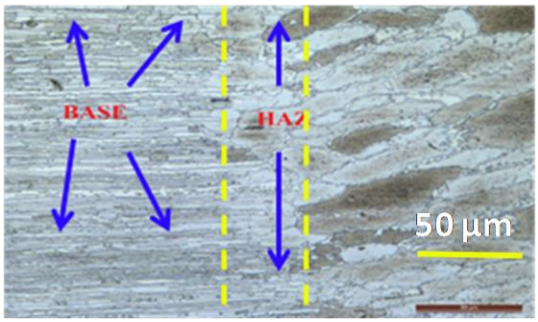

(d) Base-HAZ junction interface

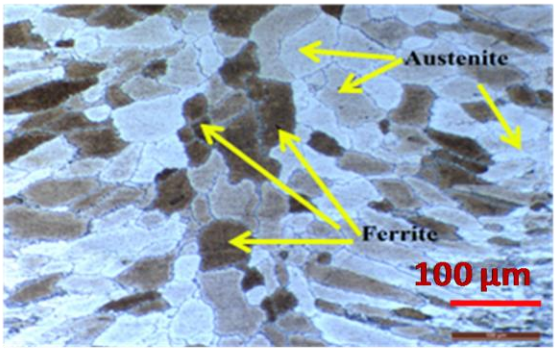

(e) Welded zone with austenite and ferrite characteristics

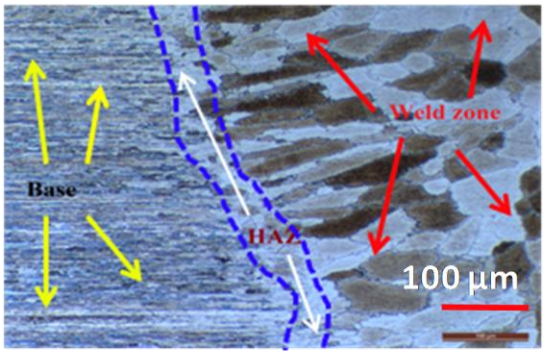

(f) Base-HAZ-Welded zone interface

Figure 4.8 Optical micrograph of welded sample (Laser power = 450 W, pulse width = 4.8 ms, scanning speed = 4.5 mm/s)

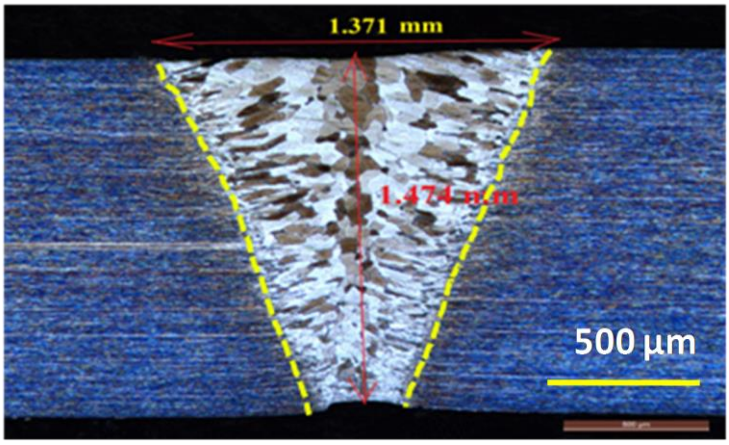

Figure 4.9 Measurement of bead width and depth of penetration using Image J software (Laser power = 450 W, pulse width = 4.8 ms, scanning speed = 4.5 mm/s)

In Figure 4.10, a stress-strain curve for all the welded samples is displayed. The stress-strain graph shows that the highest value is achieved with a laser power of 475 W, pulse width of 5 ms, and scanning speed of 5 mm/s. Furthermore, it is evident from the curves that an increase in power and pulse width led to higher stress and strain values, while a higher scanning speed resulted in lower stress and strain values.

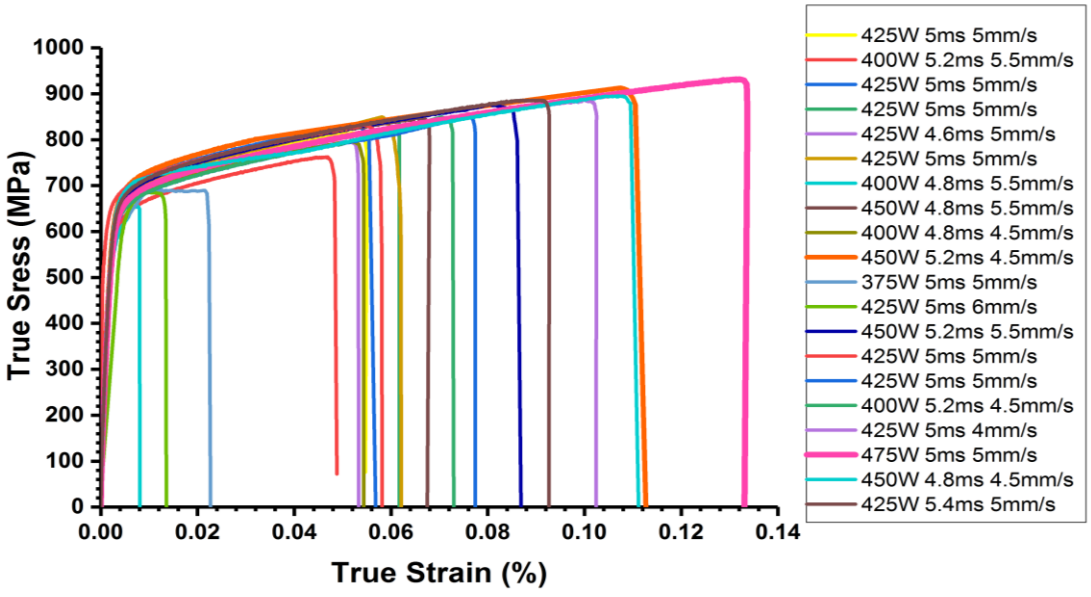

Figure 4.10 Stress-strain curve of all the welded samples

4.4.2.1. Analysis of bead width using ANNOVA

The results for bead width for different laser input parameters are measured using optical microscope and listed in table 4.2. The corelation between *Bead width and input parameters is developed using ANNOVA.*The ANOVA table 4.4 displays the quadratic model and its adequacy measures, including R^2, adjusted R^2, and predicted R^2, which are all close to 1 and is in reasonable agreement. The Model F-value of 92.04 indicates the significance of model. Here is a probability of only 0.01% so that a 'model F-value' being huge might happen owing to noise. With a p-value of less than 0.05, the model terms are significant. A signal to noise ratio larger than 4 is considered to be indicative of adequate precision. With a signal to noise ratio of 37.654, the signal is acceptable. The ANOVA analysis indicates that the bead width is most significantly affected by laser power (P), pulse width (P_W), and scanning speed (V), as well as the quadratic effects of laser power (P^2) and pulse width (P_W). Additionally, the two-factor interaction between laser power (P) and pulse width (P_W) is also significant, while the other factors have no significant impact. The F-value of 0.21 for the lack of fit suggests that it is not significant compared to the pure error, and there is a 94.18% chance that this value could be due to noise.

Table 4.4 ANOVA for response surface quadratic model of bead width

Source	**Sum of Squares**	**df**	**Mean Square**	**F Value**	**p-value Prob > F**	
Model	0.013363	9	0.001485	92.04279	< 0.0001	significant
P	0.009555	1	0.009555	592.3324	< 0.0001	
P_W	0.00158	1	0.00158	97.95041	< 0.0001	
V	0.001351	1	0.001351	83.72336	< 0.0001	
$P \times P_W$	0.000465	1	0.000465	28.83379	0.0003	
$P \times V$	6.61E-05	1	6.61E-05	4.099186	0.0704	
$P_W^2 \times V$	5.51E-05	1	5.51E-05	3.41728	0.0943	
P^2	0.000246	1	0.000246	15.22112	0.0030	
P_W^2	8.84E-05	1	8.84E-05	5.479604	0.0413	
V^2	3.54E-06	1	3.54E-06	0.219184	0.6497	
Residual	0.000161	10	1.61E-05			
Lack of Fit	2.85E-05	5	5.7E-06	0.214398	0.9418	not significant
Pure Error	0.000133	5	2.66E-05			
Cor Total	0.013524	19				

Standard deviation = 4.016E-003 Mean= 1.33 Coefficient of variation (%) = 0.30 Predicted residual error of sum of squares (PRESS) = 4.098E-004	R^2= 0.9881 Adjusted R^2= 0.9773 Predicted R^2= 0.9697 Adequate precision= 37.654

The final mathematical model for bead width (B_W) based on the actual factors determined by Design-Expert® 7.0 software is provided below:

$$B_W = -0.20563 + 5.50250\times10^{-3}\times P + 0.097813\times P_w - 0.066875\times V - 1.52500\times10^{-3}\times P\times P_w - 2.30000\times10^{-4}\times P\times V + 0.026250\times P_w\times V + 5.00000\times10^{-6}\times P^2 + 0.046875\times P_w^2 + 1.50000\times10^{-3}\times V^2 \quad (2)$$

4.4.2.2. Analysis of depth of penetration using ANNOVA

The Model F-value of 120.83 suggests that the model is significant, with a very low probability (0.01%) of such a large value occurring due to noise. A p-value of less than 0.05 indicates that the model terms are significant. A signal to noise ratio larger than 4 is considered to be indicative of adequate precision. With a signal to noise ratio of 37.654, the signal is acceptable. The ANOVA table 4.5 presents the quadratic model, which includes adequacy measures R^2, adjusted R^2, and predicted R^2. These measures are in close agreement and are mostly close to 1, indicating that the model is accurate.

Table 4.5 ANOVA for response surface quadratic model of depth of penetration

Source	**Sum of Squares**	**df**	**Mean Square**	**F Value**	**p-value Prob > F**	
Model	0.014228	9	0.001581	120.8281	< 0.0001	Significant
P	0.010151	1	0.010151	775.8279	< 0.0001	
P_W	0.001314	1	0.001314	100.4364	< 0.0001	
V	0.001541	1	0.001541	117.7483	< 0.0001	
$P\times P_W$	0.00063	1	0.00063	48.16172	< 0.0001	
$P\times V$	2.81E-05	1	2.81E-05	2.14965	0.1733	
$P_W\times V$	9.11E-05	1	9.11E-05	6.964867	0.0248	
P^2	0.000398	1	0.000398	30.3991	0.0003	
P_W^2	0.000154	1	0.000154	11.79336	0.0064	
V^2	6.45E-05	1	6.45E-05	4.933587	0.0506	
Residual	0.000131	10	1.31E-05			

Lack of Fit	2.2E-05	5	4.4E-06	0.202161	0.9480	not significant
Pure Error	0.000109	5	2.18E-05			
Cor Total	0.014359	19				
Standard deviation = 3.617E-003 Mean= 1.43 Coefficient of variation (%) = 0.25 Predicted residual error of sum of squares (PRESS) = 3.337E-004				R^2= 0.9909 Adjusted R^2= 0.9827 Predicted R^2= 0.9768 Adequate precision= 44.049		

The result of the ANOVA indicates that the laser power (P), pulse width (P_W), and scanning speed (V) have significant effects on the depth of penetration. The quadratic effects of the square of laser power (P) and pulse width (P_W), as well as the two-level interaction of laser power (P) and pulse width (P_W) and pulse width (P_W) and scanning speed (V) are also significant. The lack of fit F-value of 0.20 suggests that the lack of fit is not significant in comparison to the pure error, and there is a 94.80% chance that this could be due to noise. A non-significant lack of fit is good, as it means that the model has adequately fitted the data. The final mathematical model for depth of penetration (D_P) in terms of actual factors as determined by Design expert software is furnished below:

$$\begin{aligned} D_P = {} & +0.47966 + 5.22341\times10^{-3}\times P + 0.011619\times P_W - 0.18872\times V - 1.77500\times10^{-3}\times P\times P_W \\ & -1.50000\times10^{-4}\times P\times V + 0.033750\times P_W\times V + 6.3636\times10^{-6}\times P^2 + 0.061932\times P_W^2 \\ & +6.40909\times10^{-3}\times V^2 \end{aligned} \quad (3)$$

4.4.2.3. Analysis of ultimate tensile strength using ANNOVA

The ANOVA table 4.6 shows the quadratic model and its adequacy measures R^2, adjusted R^2, and predicted R^2, which are all close to 1. The signal to noise ratio is 27.351, indicating an adequate signal, and the ANOVA result shows that certain model terms are significant while others are not. The model terms with the greatest significance in relation to ultimate tensile strength are the effects of laser power (P), pulse width (P_W), and scanning speed (V), the quadratic effects of the square of scanning speed (V), and the two level interaction of laser power (P) and pulse width (P_W) and laser power (P) and scanning speed (V). The lack of fit F-value is 0.89, revealing that the model fits the data well and that the lack of fit is insignificant. The final

mathematical model for ultimate tensile strength is provided below, as determined by Design expert software.

Table 4.6 ANOVA for response surface quadratic model of ultimate tensile strength

Source	**Sum of Squares**	**df**	**Mean Square**	**F Value**	**p-value Prob > F**	
Model	108293.2	9	12032.58	56.66163	< 0.0001	significant
P	57001.56	1	57001.56	268.4214	< 0.0001	
P_W	9653.062	1	9653.062	45.45644	< 0.0001	
V	32310.06	1	32310.06	152.1486	< 0.0001	
$P \times P_W$	1653.125	1	1653.125	7.784595	0.0191	
$P \times V$	2628.125	1	2628.125	12.37589	0.0056	
$P_W \times V$	528.125	1	528.125	2.48695	0.1459	
P^2	1014.549	1	1014.549	4.777528	0.0537	
P_W^2	6.87013	1	6.87013	0.032352	0.8609	
V^2	3759.013	1	3759.013	17.70126	0.0018	
Residual	2123.585	10	212.3585			
Lack of Fit	999.5852	5	199.917	0.889311	0.5496	not significant
Pure Error	1124	5	224.8			
Cor Total	110416.8	19				
Standard deviation = 14.57 Mean= 824.60 Coefficient of variation (%) = 1.77 Predicted residual error of sum of squares (PRESS) = 9555.97				R^2= 0.9808 Adjusted R^2= 0.9635 Predicted R^2= 0.9135 Adequate precision= 27.351		

The final mathematical model for ultimate tensile strength is provided below, as determined by Design expert software.

$$T_S = -4069.03409 + 18.15159 \times P + 807.75568 \times P_W - 623.28409 \times V - 2.87500 \times P \times P_W + 1.45000 \times P \times V + 81.25000 \times P_W \times V - 0.010164 \times P^2 + 13.06818 \times P_W^2 - 48.90909 \times V^2 \quad (4)$$

4.4.2.4. Analysis of elongation using ANNOVA.

The significance of the model is indicated by the Model F-value of 44.92, which has only a 0.01% chance of occurring due to noise. The ANOVA Table 4.7 displays other measures of adequacy, including R^2, adjusted R^2, and predicted R^2, for the quadratic model. The model shows that laser power, pulse width, scanning speed, and the quadratic effects of the square of laser

power are the most significant model terms associated with ultimate tensile strength. The lack of fit F-value of 0.44 designates that the lack of fit is non-significant.

Table 4.7 ANOVA for response surface quadratic model of elongation

Source	**Sum of Squares**	**df**	**Mean Square**	**F Value**	**p-value Prob > F**	
Model	189.72	9	21.08	44.92	< 0.0001	significant
P	108.11	1	108.11	230.35	< 0.0001	
P_W	14.08	1	14.08	30.00	0.0003	
V	55.54	1	55.54	118.34	< 0.0001	
$P \times P_W$	1.78	1	1.78	3.79	0.0803	
$P \times V$	0.0045	1	0.0045	0.0096	0.9238	
$P_W \times V$	1.83	1	1.83	3.91	0.0763	
P^2	4.80	1	4.80	10.23	0.0095	
P_W^2	1.98	1	1.98	4.22	0.0669	
V^2	0.8647	1	0.8647	1.84	0.2045	
Residual	4.69	10	0.4693			
Lack of Fit	1.44	5	0.2886	0.4440	0.8032	not significant
Pure Error	3.25	5	0.6500			
Cor Total	194.41	19				
Standard deviation = 0.69 Mean= 6.69 Coefficient of variation (%) = 10.24 Predicted residual error of sum of squares (PRESS) = 16.26				R^2= 0.9759 Adjusted R^2= 0.9541 Predicted R^2= 0.9163 Adequate precision= 26.401		

The final mathematical model for elongation is provided below, as determined by Design expert software.

$$E_L = +163.95693 - 0.028657 \times P - 49.38949 \times P_W - 21.05307 \times V - 0.094250 \times P \times P_W + 1.90000 \times 10^{-3} \times P \times V + 4.78750 \times P_W \times V + 6.99 \times 10^{-4} \times P^2 + 7.01989 \times P_W^2 - 0.741818 \times V^2 \quad (5)$$

Figures 4.11 (a-d) show the relationship between the actual and predicted values of bead width, depth of penetration, ultimate tensile strength, and elongation. While the predicted results show excellent concordance with the measurements, the slopes of the lines are near to 450, indicating that the suggested models are adequate.

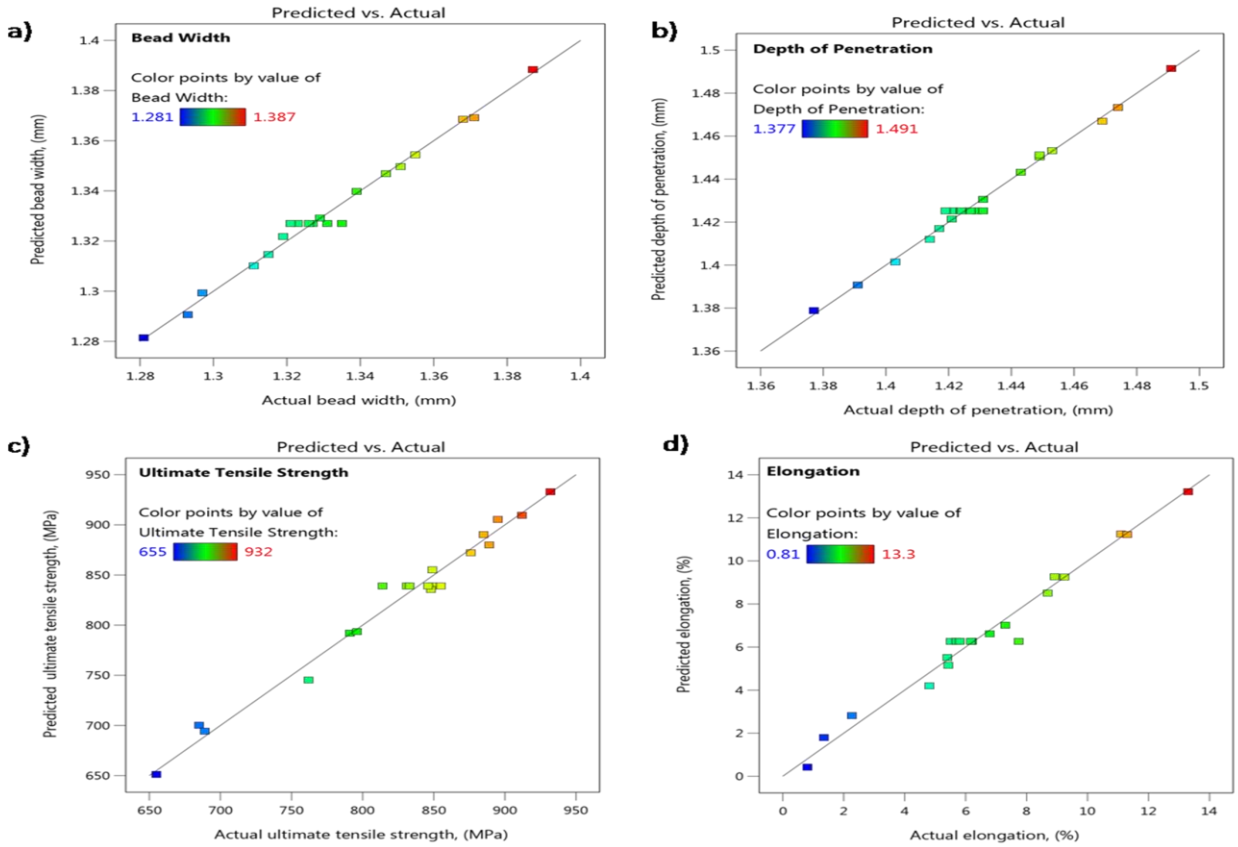

Figure 4.11 Plot of predicted vs. actual response of (a) bead width, (b) depth of penetration, (c) ultimate tensile strength, and (d) elongation.

4.4.2.5. Effect of process parameters on the bead width

The effects of process parameters on the response are acknowledged through the development of a response surface model. Figure 4.12 (a-b) display a response contour and 3-D surface plot depicting the effect of laser power and pulse width on bead width at a fixed scanning speed of 5 mm/s. It is evident from these figures that an increase in laser power and pulse width results in an increase in bead width due to the added energy contribution to the work piece. Pulse width is the duration of the laser pulse for each phase, and an increase in pulse width leads to an increase in interaction time and heat absorption by the work piece, resulting in an increase in bead width. Figure 4.12 (c-d) outlines the impact of laser power and scanning speed on bead width at a fixed pulse width of 5 ms, where an increase in laser power leads to an increase in bead width and an increase in scanning speed leads to a decrease in bead width due to reduced interaction time between the laser energy and the work piece. Figure 4.12 (e-f) shows the effect of scanning

speed and pulse width on bead width at a fixed power of 425 W, where an increase in pulse width leads to an increase in bead width, while an increase in scanning speed leads to a decrease in bead width.

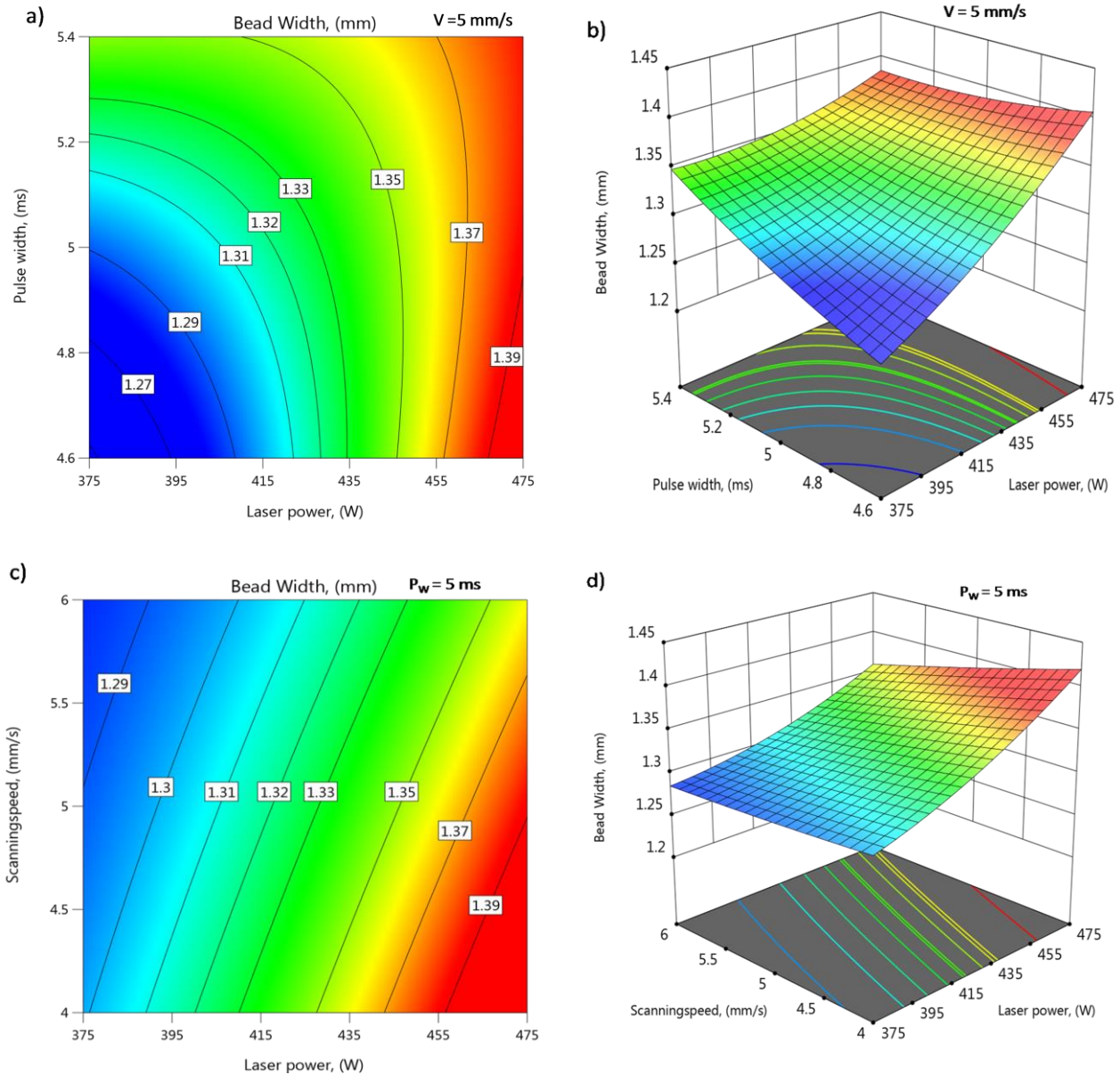

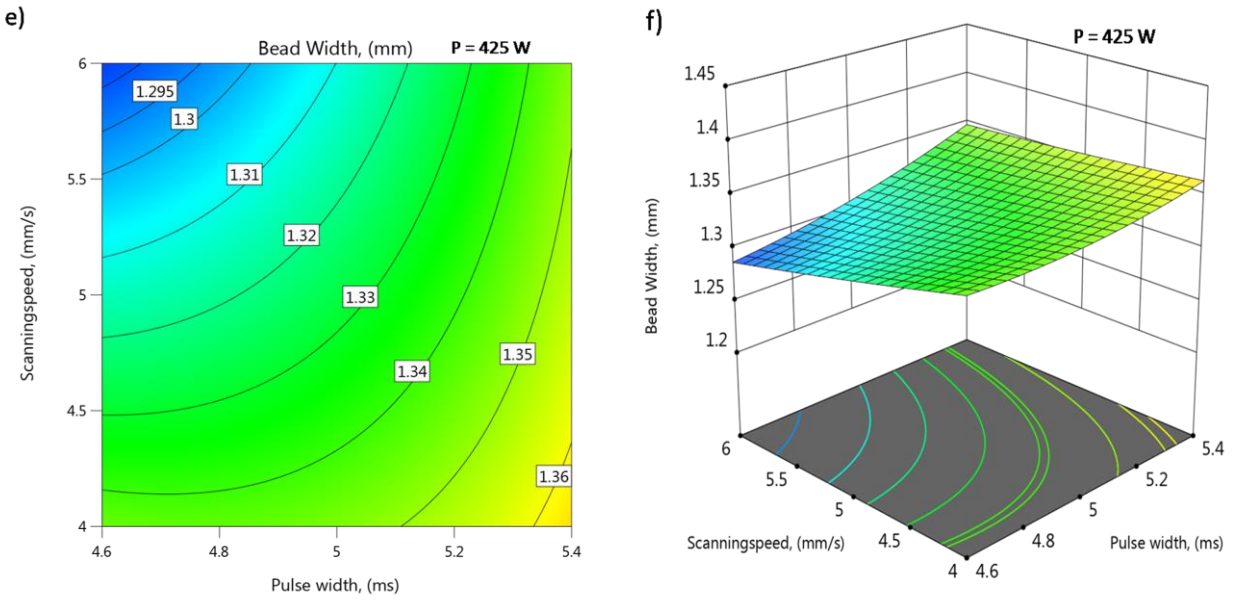

Figures 4.12 (a-f): Contours and 3-D response surface plots showing the effects of input parameters on the bead width

4.4.2.6. Effect of process parameters on the depth of penetration

Figure 4.13 (a-b) illustrates the impact of laser power and pulse width, at a constant scanning speed, on depth of penetration through a response contour and 3-D surface plot. These figures demonstrate that when laser power is increased, there is a greater energy penetration on the work piece resulting in an increased depth of penetration. Pulse width also impacts depth of penetration as an increase in pulse width increases the interaction time between the laser energy and work piece, resulting in greater heat penetration and depth of penetration. Figure 4.13 (c-d) shows that when laser power increases, depth of penetration also increases, but when scanning speed increases, depth of penetration decreases due to decreased interaction time between the laser energy and work piece. Figure 4.13 (e-f) demonstrates the effect of pulse width and scanning speed on depth of penetration at a fixed laser power of 425 W. It shows that an increase in pulse width results in greater depth of penetration, while an increase in scanning speed results in decreased depth of penetration.

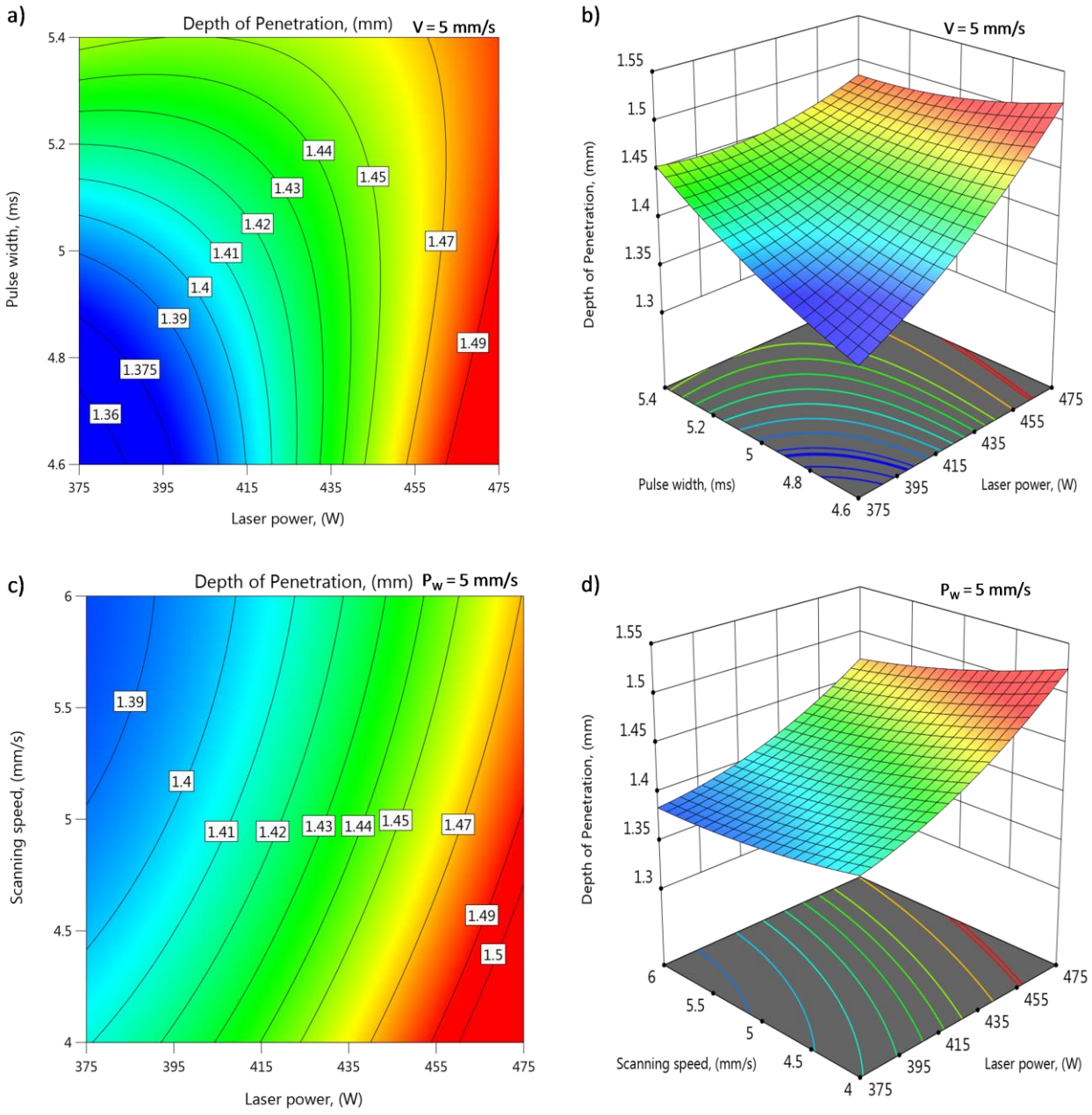
a)
Depth of Penetration, (mm)
V = 5 mm/s
Pulse width, (ms)
Laser power, (W)
1.36
1.375
1.39
1.4
1.41
1.42
1.43
1.44
1.45
1.47
1.49
b)
V = 5 mm/s
Depth of Penetration, (mm)
Pulse width, (ms)
Laser power, (W)
c)
Depth of Penetration, (mm)
Pw = 5 mm/s
Scanning speed, (mm/s)
Laser power, (W)
d)
Pw = 5 mm/s
Depth of Penetration, (mm)
Scanning speed, (mm/s)
Laser power, (W)

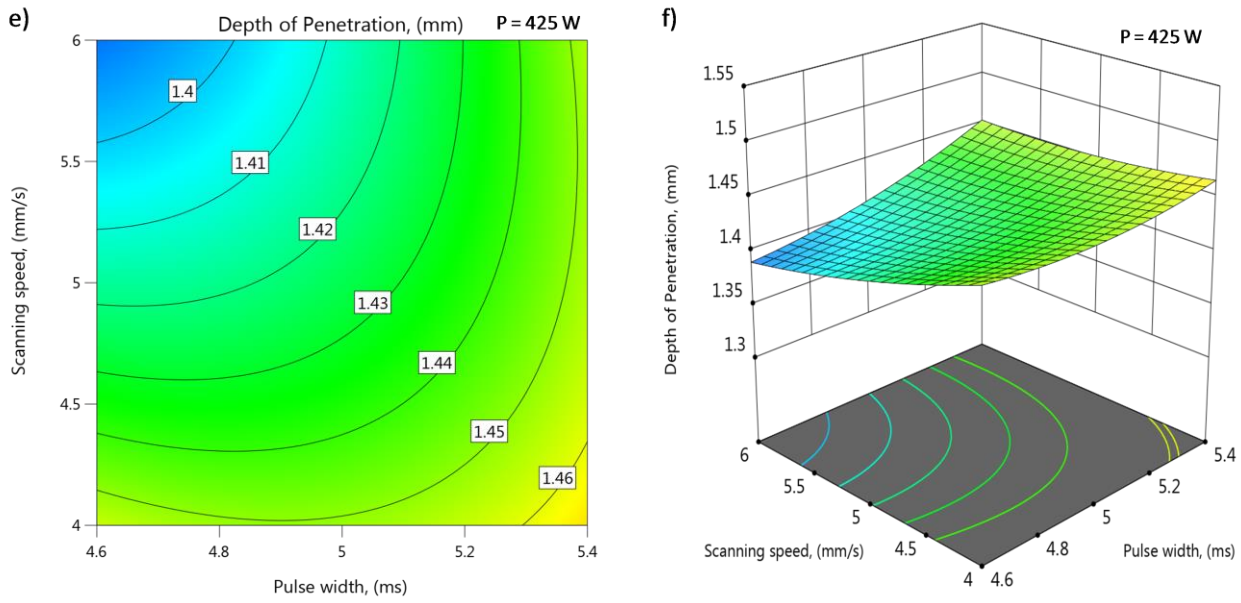

Figures 4.13 (a-f): Contours and response surface plot show the effects of input parameters on the depth of penetration

4.4.2.7. Effect of process parameters on the ultimate tensile strength (UTS)

Figure 4.14 (a-b) displays the response contour and 3-D surface plot of the effect of laser power and pulse width on UTS, at a fixed scanning speed. It can be observed from these figures that the ultimate tensile strength increases with an increase in laser power and pulse width. When power is increased, more energy penetrates the workpiece, resulting in sufficient heat and a deep depth of penetration, leading to a strong joint with high strength. Increasing the pulse width raises the temperature of the fusion zone and reduces the amount of martensite construction in the fusion zone, which directly increases the tensile strength and reduces the chance of cracking. With an increase in pulse width, the interaction time between laser energy and the workpiece increases, resulting in more heat penetration and higher strength. It is evident that a simultaneous increase in laser power and pulse duration considerably strengthens the tensile strength by expanding the temperature of the fusion zone and intensity of melt pool penetration. Figure 4.14 (c-d) outlines the response contour and 3-D surface plot to demonstrate the impact of laser power and scanning speed, at a fixed pulse width of 5 ms, on the UTS. It is revealed from the figure that ultimate tensile strength expands as laser power is increased and declines as scanning speed is increased. The impact of scanning speed and pulse width upon UTS, at a fixed power of 425 W, is

identified from the response contour and 3-D surface plot in figure 4.14 (e-f). It is clear from these figures that ultimate tensile strength increases with pulse width while decreasing with scanning speed.

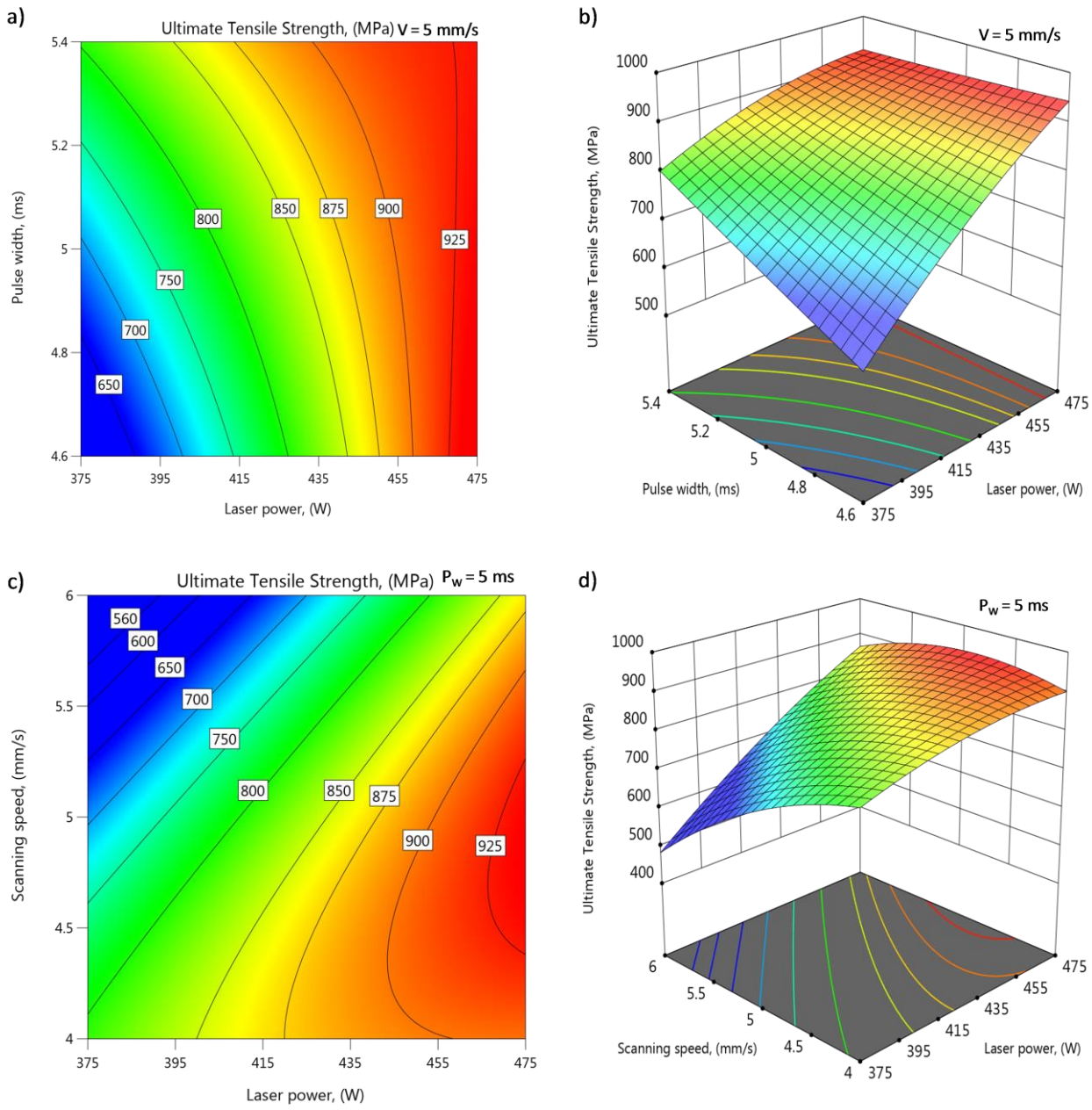

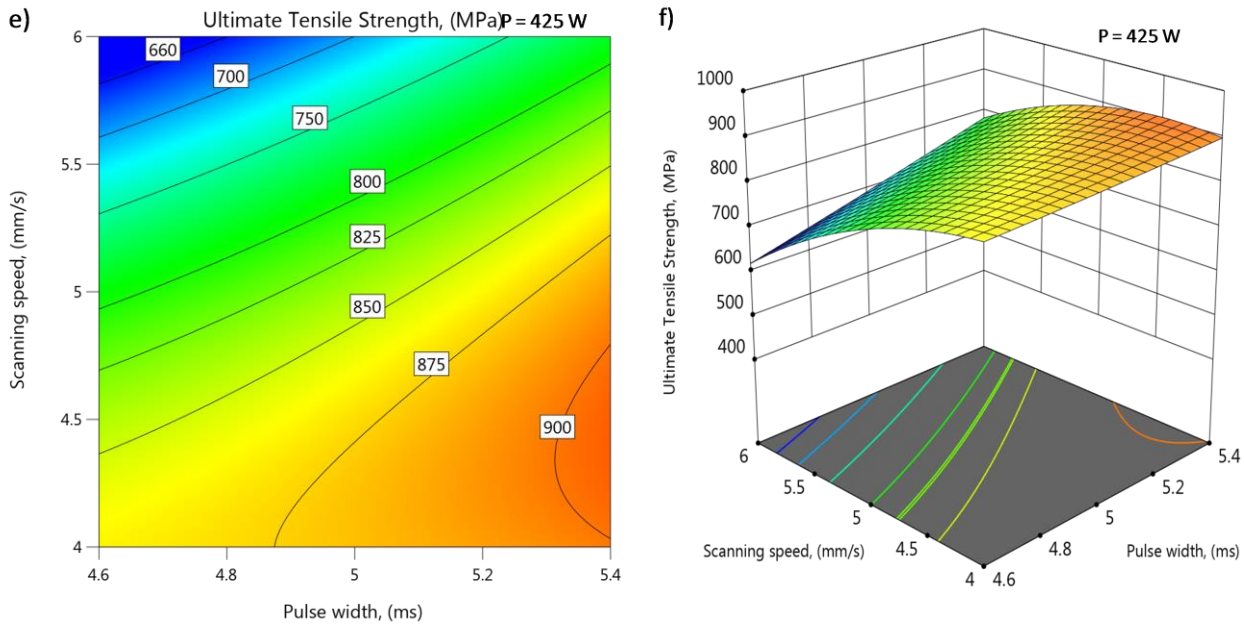

Figures 4.14 (a-f): Contours and response surface plot show the effects of input parameters on the ultimate tensile strength

4.4.2.8. Effect of process parameters on the % of elongation

Elongation is the primary quantity for determining flexibility performance in weld joints, when it comes to weld joints. Figure 4.15 (a-b) illustrates the impact of laser power and pulse width on elongation, at a fixed scanning speed of 5 mm/s, through response contour and 3-D surface plot. It is observed that elongation increases significantly with an increase in laser power and pulse width. Higher laser power results in more energy penetration and sufficient heat, creating a superior melt pool and stronger fusion zone, resulting in a ductile joint with prolonged elongation. Similarly, pulse width increases the interaction time between laser energy and work piece, ensuring a flexible joint and an extended elongation. Figure 4.15 (c-d) outlines the impact of laser power and scanning speed, at a fixed pulse width of 5 ms, on elongation, with an increase in laser power resulting in an increase in elongation, and an increase in scanning speed leading to a decrease in elongation due to inferior penetration and brittle joint. Figure 4.15 (e-f) shows the impact of scanning speed and pulse width on elongation, at a fixed power of 425 W, where elongation increases with pulse width and decreases with scanning speed.

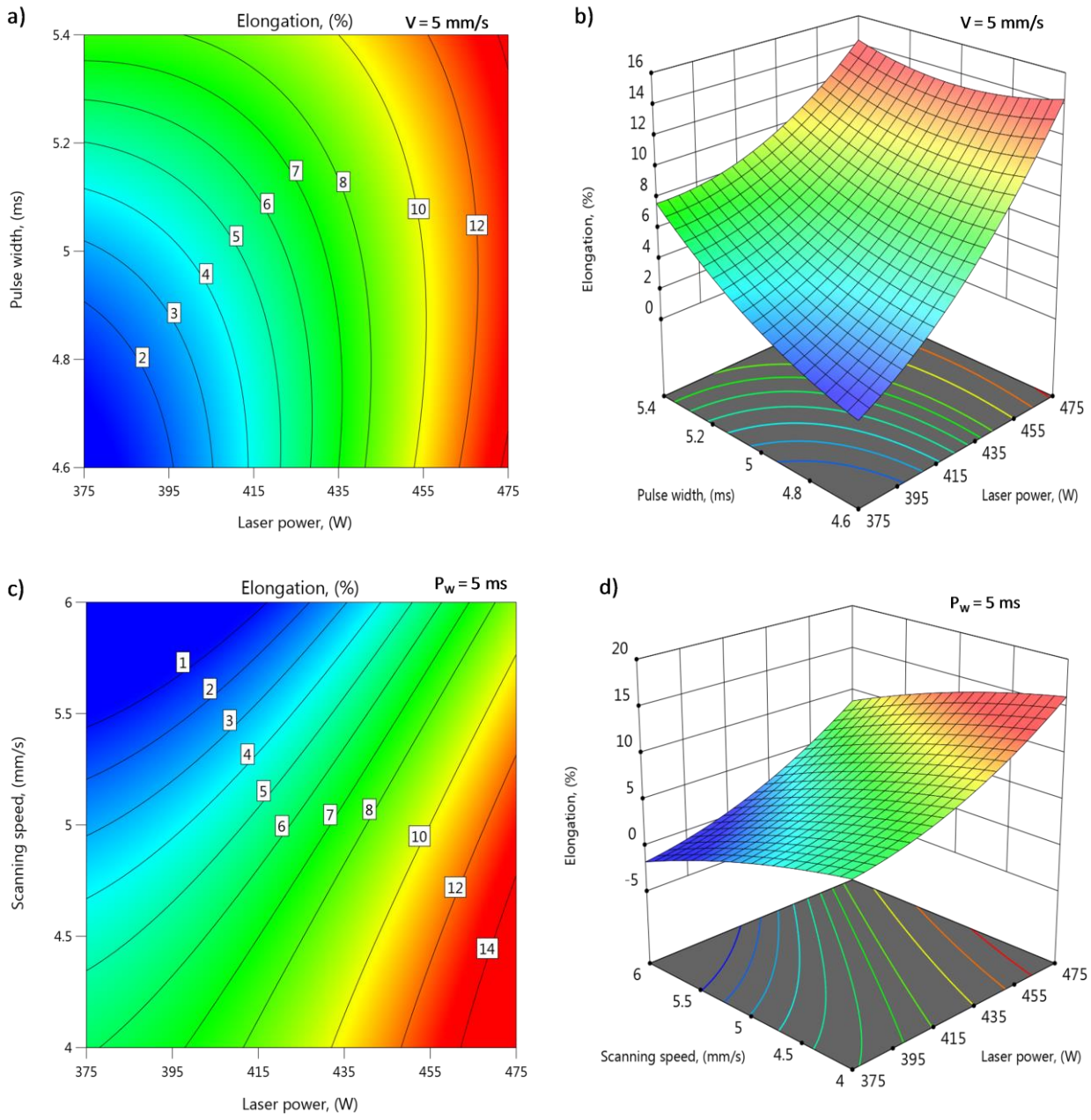
a)
Elongation, (%)
V = 5 mm/s
Pulse width, (ms)
Laser power, (W)
b)
V = 5 mm/s
Elongation, (%)
Pulse width, (ms)
Laser power, (W)
c)
Elongation, (%)
Pw = 5 ms
Scanning speed, (mm/s)
Laser power, (W)
d)
Pw = 5 ms
Elongation, (%)
Scanning speed, (mm/s)
Laser power, (W)

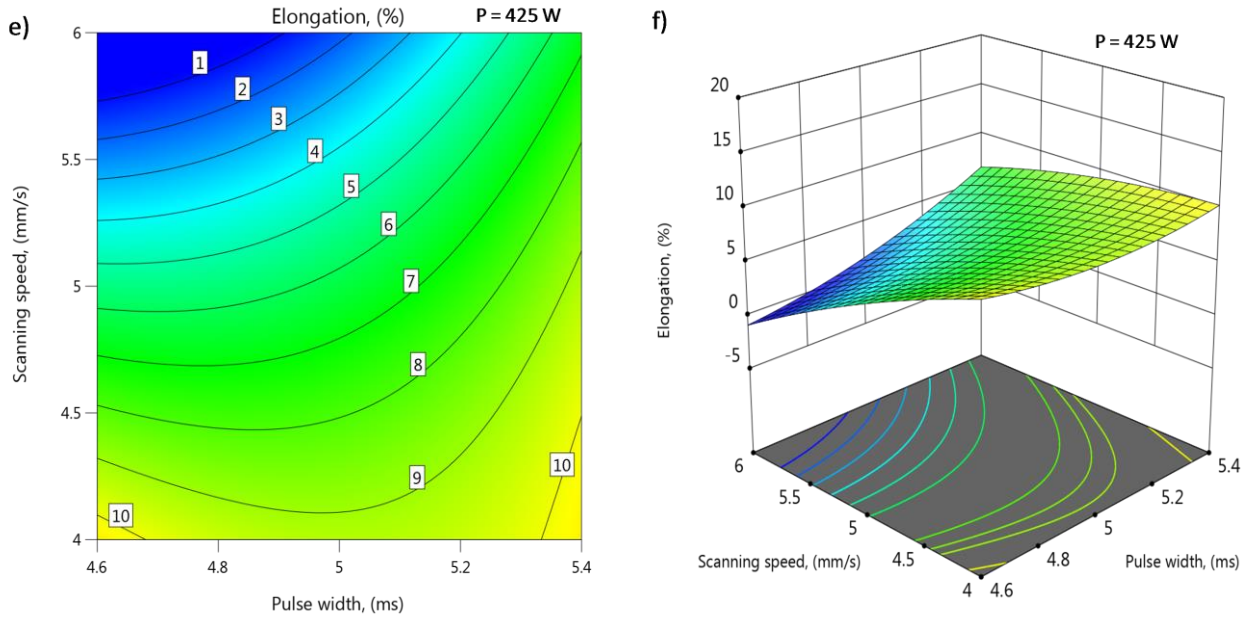

Figures 4.15 (a-f): Contours and response surface plot show the effects of input parameters on the elongation

4.4.3. Multi-objective Optimization

The objective of the numerical optimization is to achieve desirable bead width, maximum depth of penetration, ultimate tensile strength, and % of elongation while minimizing the cost of operating energy. This is accomplished by using the least amount of laser power and the highest welding speed within the design space. Table 4.8 shows the goals, lower and upper limits, and importance of each response for numerical optimization. The different input-output relationships obtained for bead width, depth of penetration UTS and % of elongation through ANNOVA are already incorporated in optimization software Design matrix and constraints described in table 4.8 are also given as input to the software for optimization. Table 4.9 presents the best welding parameter combinations based on the criteria in Table 4.8 obtained as optimum set of solutions from Design Expert® 7.0 software. These combinations will ensure that the desirable range of bead width, maximum depth of penetration, as well as maximum ultimate tensile strength and elongation is achieved while minimizing the cost of operating energy. The optimum values of UTS for the welded joint are about ~ 865 MPa, which is 99% of the ultimate tensile strength of

the base material. However, the elongation of the welded samples has significantly decreased compared to that of the base material. The optimal laser process parameters for obtaining a high-quality weld joint are a laser power between 423-425 W, scanning speed of 5.3 mm/s, and pulse width of 5.4 ms.

Table 4.8 Criteria of numerical optimization.

Parameter	**Goal**	**Lower Limit**	**Upper Limit**	**Importance**
P (W)	minimize	375	475	3
P_W (ms)	is in range	4.6	5.4	3
V (mm/s)	maximize	4.0	6.0	3
B_W (mm)	is in range	1.281	1.387	3
D_P (mm)	maximize	1.377	1.491	3
T_S (MPa)	maximize	655	932	3
E_L (%)	maximize	0.81	13.3	3

Table 4.9 Optimal welding condition based on the criterion

Sl. No.	P (W)	P_W (ms)	V (mm/s)	B_W (mm)	D_P (mm)	T_S (MPa)	E_L (%)	*Desirability*
1	425.406	5.400	5.337	1.352	1.452	866.096	8.599	0.635
2	425.381	5.400	5.338	1.352	1.452	865.977	8.596	0.635
3	425.224	5.400	5.340	1.352	1.452	865.525	8.580	0.635
4	425.979	5.400	5.340	1.352	1.452	866.809	8.631	0.635
5	426.121	5.400	5.349	1.352	1.452	866.204	8.619	0.635
6	424.636	5.400	5.325	1.352	1.452	865.806	8.574	0.635
7	426.346	5.400	5.358	1.352	1.452	865.759	8.613	0.635
8	427.145	5.400	5.353	1.352	1.452	867.641	8.682	0.635
9	423.757	5.400	5.315	1.352	1.452	865.247	8.541	0.635
10	423.182	5.400	5.330	1.351	1.451	862.824	8.468	0.635

4.5. Conclusions

The use of pulsed Nd: YAG laser for butt joint welding of 2205 duplex stainless steel is studied through experimental analysis and response surface methodology. Statistical regression models are employed to investigate the effects of laser power, pulse width, and scanning speed on weld bead characteristics such as depth of penetration, bead width, ultimate tensile strength, and

elongation of welded samples. Additionally, the process parameters are optimized to obtain a high-quality weld joint.

The study revealed that the laser power has a significant impact on the shape of the weld and the strength and flexibility of the joint. Increasing the power results in more heat energy being transferred to the work piece, which leads to larger melt pools at the fusion zone. This, in turn, creates wider and deeper weld beads, resulting in higher ultimate tensile strength and elongation. The control of weld bead geometry, as well as ultimate tensile strength and elongation, is greatly affected by pulse width. Increasing the pulse width results in longer duration of the laser pulse for each phase, leading to more heat energy being transferred to the work piece, causing high temperature in the fusion zone. This reduces the number of martensite structures and results in a larger melt pool, resulting in deeper penetration and wider bead width, which ultimately provides better strength and elongation at the weld joint.

Scanning speed also can greatly affect the shape of a weld, its strength, and its ability to stretch. Based on these observations, it is clear that increasing the scanning speed results in a decrease in the depth of the weld, the width of the bead, and the strength and elongation of the metal. There are no apparent cracks, voids, or porosity detected in the fusion zone following welding. However, a noticeable alteration in grain growth is observed in the fusion zone compared to the base zone. Despite the high level of heat applied, the grain structures in the base zone remained unaffected. The heat affected zone is minimal, indicating good quality weld joints. Both ferrite and austenite phases are clearly observed in the weld zone. For achieving a high-quality welded joint, it is recommended to use laser process parameters such as a laser power ranging between 423-425 W, scanning speed of 5.3 mm/s and a pulse width of 5.4 ms. This will result in optimal UTS values of approximately 865 MPa, which is 99% of the ultimate tensile strength of the base material.

CHAPTER 5

Comparison of Molten Pool Behaviour of Different Numerical Models (CFD) and validation with experimental study

Chapter 5

5.1. Introduction

So far for both simulation processes we only consider thermal conductivity in isotropic and anisotropic approach but it is obvious to consider fluid flow as in reality there is a situation of molten metals flows, so to achieve accurate simulation it is required to include the CFD in finite element method.

Understanding the flow characterisation inside the molten pool and formation of the weld shape has great theoretical and engineering value. To understand the flow behaviour inside the molten pool, numerical simulation is the best tool since it has greater flexibilities and cost competitiveness to explore such complex phenomena efficiently. In general, the dimensions of the geometry plays a vital role in the formation of the flow pattern in the molten pool. Marangoni convection due to variation of surface tension may take place in thin plates and buoyancy forces due to natural convection may dominateat the plate with higher thickness. It would be very interesting to know the flow pattern when the thin plates is processed with a smaller laser beam diameter. Three numerical models are developed using COMSOL Multiphysics for thin plates considering the flow in the molten pool to be laminar in the first model and turbulent(yPlus and k-ω model) in the two other models. A pulsed heat source is modeled using COMSOL's Events interface which maintains a finer time steps where the solution changes rapidly and larger time steps when solution changes slowly. The three models take into account the temperature dependent thermo-physical properties, tracking of solid-liquid phase interface with keyhole, Marangoni convection and buoyancy forces. The numerically calculated melt pool shapes from three models are compared with experimentally calculated melt pool. Moreover, the intensity of the flow in the molten pool have been described through nondimensional Marangoni number and Grashof number.

The high strength dual microstructure material may have complications when it is subjected to conventional machining or joining process. Aforementioned setbacks may be overcome when the advanced materials processing with an intense laser heat source which increases the temperature of the material beyond its melting or boiling point.Studying the flow pattern in the molten pool due to Marangoni and natural convections in this special class stainless steel would be an interesting research problem. Because, an intense laser beam will create very large temperature gradient at the surface and along the thickness of the materials than those in conventional processes. Explorations of such phenomena through computational modeling will help us to get a better insight of the laser welding process from a theoretical point of view.

In the past, most of the numerical models dealt with the formation of weld shape and keyhole behaviour in AISI 304 stainless steel, low carbon steel, titanium, aluminium etc. So far, a limited number of researchers have focused on the study of flow behaviour during laser beam welding of dual microstructure Duplex stainless steel. Moreover, the researchers are considering their molten pool as either laminar or turbulent flow while studying the laser beam welding. However, no one has reported anywhere the appropriate the fluid flow model which is appropriate for small size geometries. In the present study, three numerical models are explored to compare their weld shapes with experimental weld shape and investigate the variations in the flow patterns of three models. We will try to find the appropriate model among the three alternatives based on the criteria of satisfactory prediction of weld shape involving less computational time. Numerical models are computed with Intel Core i7-6700K CPU@4.00 GHz and RAM of 64 GB.

5.2. Methodology

5.2.1. Numerical modeling

The numerical modeling with COMSOL Multiphysics is done using Non-Isothermal Flow Interface (NITF) which combines Heat Transfer in Fluids (HT) with fluid flow for the calculation of the flow inside the melt pool and the temperature field. To validate the weld shape obtained numerically with that observed in experiment, three different numerical models have been proposed. In the first model, the molten pool is considered to be laminar. In the rest two, Reynolds-Averaged Navier-Stokes (RANS) yPlus and k-ω turbulent model are used in order to realise the effects of turbulence. Laminar and turbulent yPlus models are solved with the fully coupled solver. Turbulent k-ω model is solved with segregated solver. In k-ω model, a high performance Parallel Direct Sparse Solver (PARDISO) is used to calculate variables like velocity, pressure and temperature and iterative GMRES solver is used to calculate turbulence variables which helps in reducing the requirement of RAM [10]. The most important physical aspects such as solid-to-liquid phase change, Marangoni convection due to surface tension gradient and natural convection due to buoyancy forces are incorporated in this present numerical model. A solid-to-liquid phase change phenomenon is incorporated in the numerical model by apparent specific heat capacity method in the two phase zone. The properties in the two-phase zone are calculated in the following way.

$$k = k_{solid}\left(1 - \alpha(\mathrm{T})\right) + k_{liquid}\left(\alpha(T)\right) \quad (1)$$

$$\rho = \rho_{solid}\left(1 - \alpha(\mathrm{T})\right) + \rho_{liquid}\left(\alpha(T)\right) \tag{2}$$

$$C_p^{app} = c_{p_{solid}}\left(1 - \alpha(T)\right) + c_{p_{liquid}}\left(\alpha(T)\right) + L_f \frac{\partial \alpha}{\partial T} \tag{3}$$

$$\alpha(T) = \begin{cases} 1 & T \geq T_l \\ \dfrac{T - T_s}{T_l - T_s} & T_{sl} \leq T \leq T_l \\ 0 & T \leq T_{sl} \end{cases} \tag{4}$$

For the solid phase, $\alpha(T) = 0$, and for only liquid, $\alpha(T) = 1$. Latent heat of fusion is considered as L_f =500 kJ/kg. The material solidus (T_{sl}) and liquidus (T_l) temperatures are considered as 1658 K and 1773 Krespectively.

The movement of the solid-liquid interface (molten pool) is modeled through modifying the viscosity of the fluid. A high value of dynamic viscosity is assigned for solid material, whereas for the liquid zone, the viscosity of the liquid is assumed. Marangoni convection is applied on the free surface in order to consider the fluid flow due to temperature-dependent surface tension. A variation of surface tension may come from thermal or composition/concentration effects (Eqs. [5]), causes surface tension to vary significantly in space, exhibiting Marangoni stresses at the free surfaces. Because of the liquid metal's viscosity, shear stresses need to be used to counterbalance these stresses. The flow of the weld pool is primarily driven by shear stress from areas of high to low surface tension. The final shape of the weld can be significantly impacted by this Marangoni driven flow.

$$d\sigma = \frac{\partial \sigma}{\partial T} dT + \frac{\partial \sigma}{\partial c} dc \tag{5}$$

where T and c are temperature and concentration. A nondimensional value representing the ratio of the thermocapillary effect to the viscous forces indicates the significance of the surface tension gradient resulting from thermal influences.

$$\boldsymbol{M_a} = \left|\gamma\right| \boldsymbol{L} \Delta \boldsymbol{T} / \left(\mu \alpha\right) \tag{6}$$

where L is the characteristic length scale (m), ΔT is the maximum temperature difference across the interface (K), μ is the dynamic viscosity (Pa.s), α is the thermal diffusivity (m^2/s), $\gamma = \left|\dfrac{d\sigma}{dT}\right|$ is the thermal dependence of the surface tension in N/(m.K). The absolute value is used in the expression so that the nondimensional Marangoni number remains positive. The above dimensionless Marangoni number expression can be rearranged in the

following format since there is a similarity with the Rayleigh number that is relevant for conjugate heat transfer due to Archimedes' forces.

$$\boldsymbol{Ma} = \frac{\sqrt{\frac{\gamma \Delta \boldsymbol{T}}{\rho \boldsymbol{L}}}}{\left(\nu / \boldsymbol{L}\right)} \frac{\sqrt{\frac{\gamma \Delta \boldsymbol{T}}{\rho \boldsymbol{L}}}}{\left(\alpha / \boldsymbol{L}\right)} \tag{7}$$

where ν is the kinematic viscosity in (m^2/s), $\sqrt{\frac{\gamma \Delta T}{\rho L}}$ term is the thermocapillary velocity, $\left(\alpha / \boldsymbol{L}\right)$ term is the thermal diffusion velocity and $\left(\nu / L\right)$ term is the momentum diffusion velocity.

Typical orders of magnitude for flow characterisation with the Marangoni number depend highly on the geometry. However, a Marangoni number above 10^5 will usually develop unsteady flow.The wall conditions used in the model can be seen from Figure 3. The free surface deformation of the weld pool which also influences the internal weld pool flow and heat and mass transfers is neglected in the present numerical models.

The Grashof number is the ratio of buoyancy force to viscous force acting on a fluid and is defined as

$$Gr = \frac{g\beta(T - T_\infty)L^3}{\nu^2} \tag{8}$$

where g is the acceleration due to gravity, $\beta$is the coefficient of thermal expansion, L is the characteristic length of weld width, T is the keyhole surface temperature,T_α is the fluid temperature at the keyhole boundary surface and ν is the kinematic viscosity.

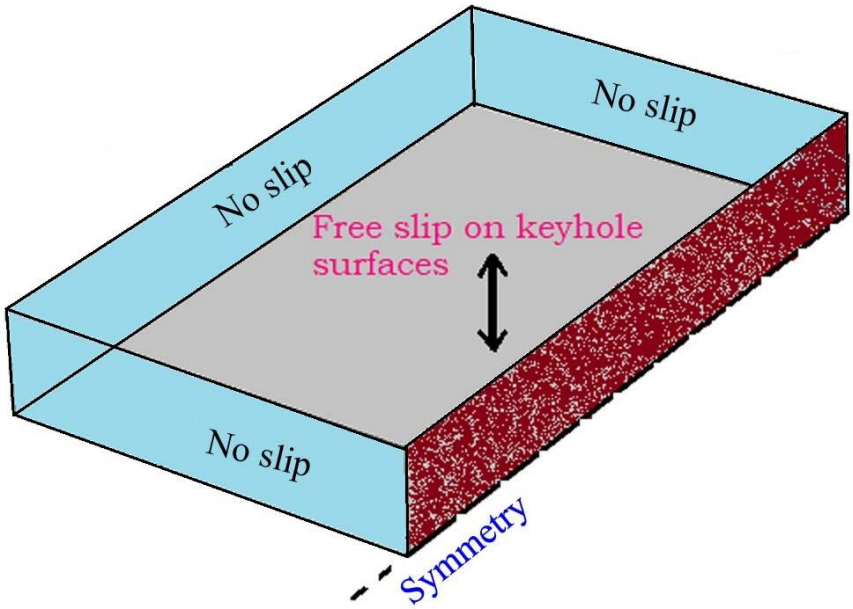

Figure 5.1 Computational domain and boundary conditions used in the present model

In the present model, the laser beam is modeled as rectangular pulsed profile and laser intensity is considered to have constant ON (4.8 ms) and OFF time as shown in Figure 5.2. So, a defined pulse load that turns on and off repeatedly at known times and it will heat the surface of the plate within the fraction of the time. Modeling such a situation efficiently is always difficult as maintaining the more number of time sub-steps within the pulse on time. This phenomenon is modeled with Events interface which allows COMSOL Multiphysics to take very fine time steps when there are rapid variations in the solution, whereas it maintains coarse time steps when there are gradual variations. In COMSOL Multiphysics, to solve a time–dependent problem the implicit time-stepping algorithm is used which choose a time step based upon a user-specified tolerance. The solution may completely ignore the change in heat load when the breadth of the load becomes extremely small if the tolerance is set too loosely. During pulse off time, the finer time steps are avoided by using Explicit Events which remind for instructing the solver to assess the answer at a predetermined time. Until the preceding occurrence is reached, the solver will proceed as previously from that point on. A time step variation for two pulses during events is shown in Figure 5.3. The spacing of the red spots shows the varying time steps used by the solver.

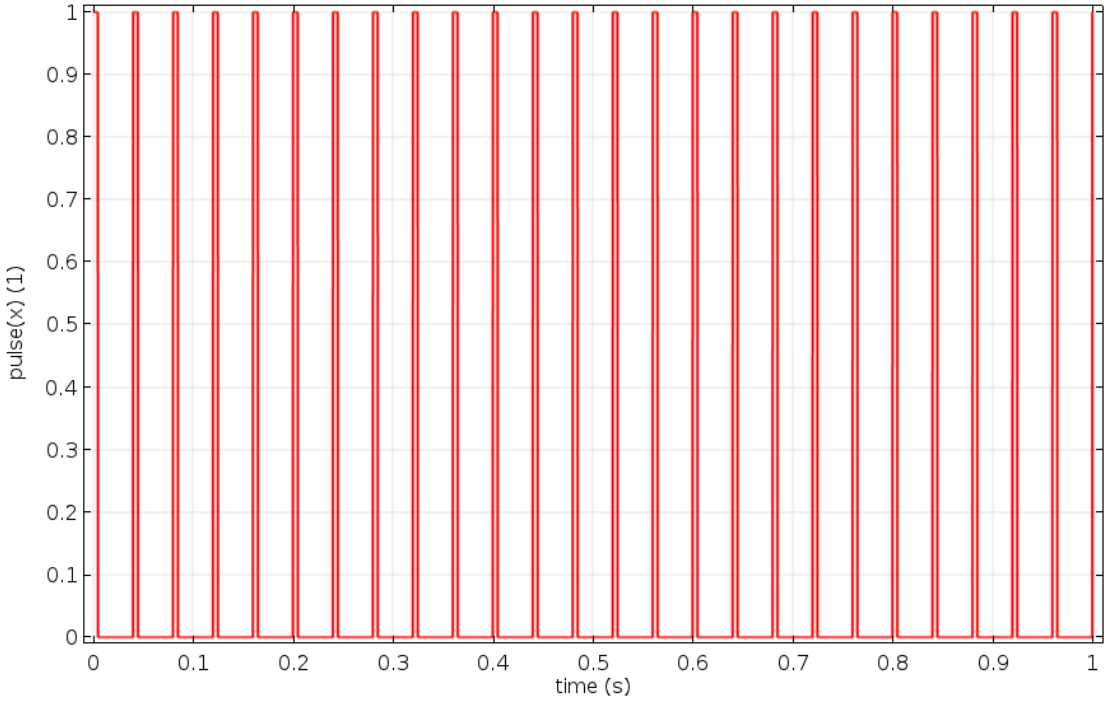

Figure 5.2 A defined pulse profile over time

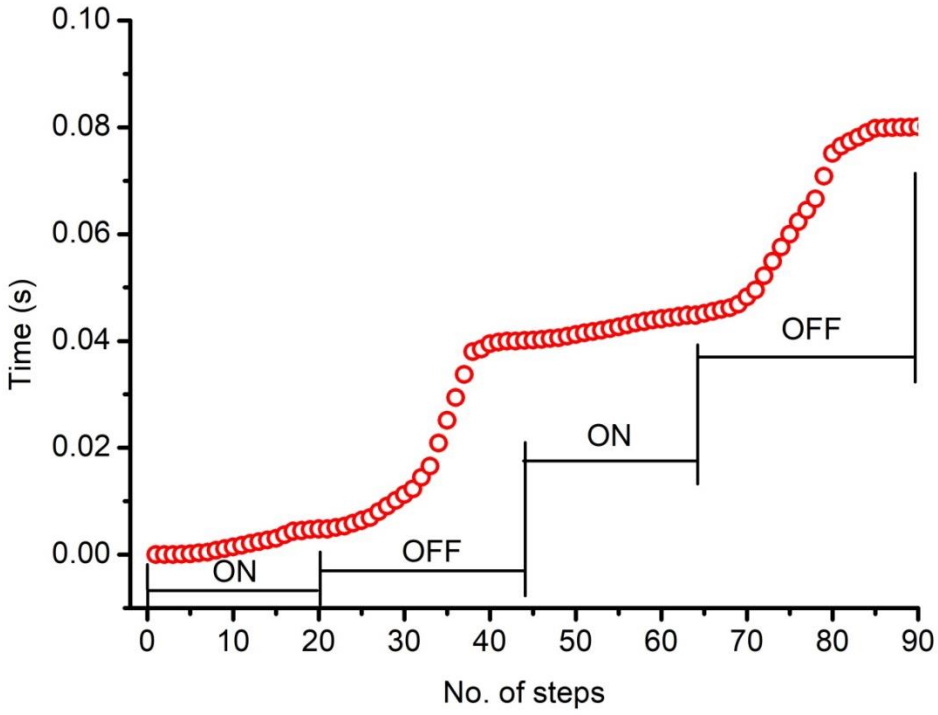

Figure 5.3 Time step variation during the events

The evolution of the solid-liquid interface in the workpiece is captured through the following analytical function [11].

$$h(T) = (T - T_s)H(T - T_s)H(T_l - T) + H(T - T_l) \quad (9)$$

where T_s is the solidus temperature of the material where the phase change starts, T_l is the liquidus temperature of the material where the phase change ends, and H is the Heaviside Step Function, h is the phase transformation tracking parameter that is zero when the material is solid and when the material reaches liquidus temperature h becomes 1. The above analytic expression is incorporated in COMSOL using its smoothed Heaviside function.

The laser, work piece parameters and some other important parameters used in the model are listed in Table 5.1. Moreover, normalised temperature-dependent material properties are also shown in Figure 5.4. The solved governing equations and boundary conditions used in the model are summarised in Table 5.2.

Table 5.1 Laser, geometric and material properties [12] used in the simulations

Laser parameters	**Unit**	**Value**
Laser peak power	kW	3.750
Beam diameter	mm	0.750
Scanning speed	mm/s	5.5
Pulse duration	ms	4.8
Frequency	Hz	25
Geometry parameters		
Length	mm	7
Width	mm	5
Thickness	mm	1.5
Material properties		
Phase change start temperature (T_s)	K	1658
Phase change end temperature (T_l)	K	1773
Solidus specific heat $\left(C_p\right)$	J/kg.K	500
Apparent specific heat $\left(C_p^{app}\right)$	J/kg.K	5084.6
Solidus density (ρ)	kg/m^3	7925

Solidus thermal conductivity	W/m.K	18
Latent heat of fusion (L_f)	kJ/kg	500
Marangoni coefficient	N/m.K	-4.3×10^{-4}
Dynamic viscosity	Pa.s	0.0085
Absorption coefficient		0.65
Ambient temperature (T_0)	K	303

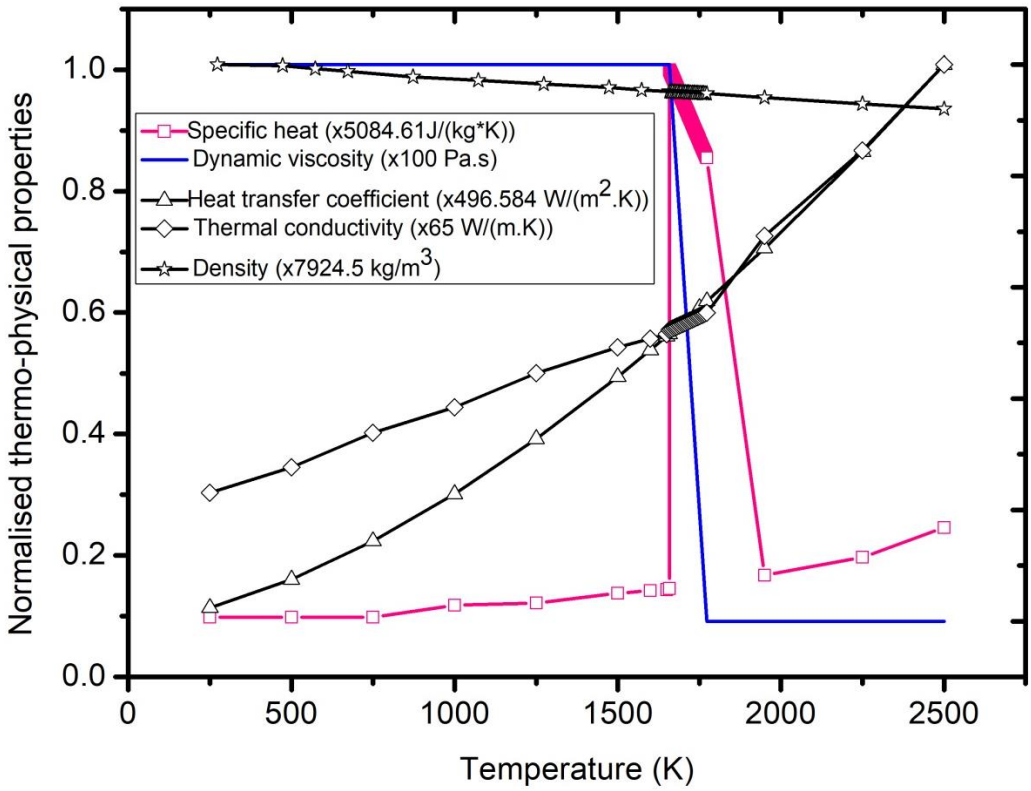

Figure 5.4 Normalised temperature-dependent material properties of 2205 DP stainless steel

Table 5.2 Solved governing equations and boundary conditions used in the model

Equations/ Conditions	**Laminar model**	**Algebraic yPlus turbulence model**	**K-ω turbulence model**
Governing equations for heat transfer in fluid model	$\rho C_p \frac{\partial T}{\partial t} + \rho C_p \mathbf{u}.\nabla T + \nabla.\mathbf{q} = Q + Q_p + Q_{vd}$ $\mathbf{q} = -k\nabla T$		ρ: solid density (kg/m^3) k: solid thermal conductivity (W/m·K) $\mathbf{u}$: velocity vector (m/s) **q:** heat flux by conduction (W/m^2) Q: voulmetric heat source (W/m^3) Q_p: work done by pressure change Q_{vd}: viscous dissipation in the fluid Cp: heat capacity at constant

<table>
<tr><td></td><td></td><td colspan="2">pressure (J/kg.K)
t: time (s), T: absolute temperature (K),
∇ : gradient operator</td></tr>
<tr><td>Boundary conditions for HT in fluid model
<u>3-D Conduction</u></td><td><u>Volumetric heat source</u>
$q_{applied} = \frac{3AP}{\pi abc}\exp\left(-\frac{3x^2}{a^2}\right)\exp\left(-\frac{3y^2}{b^2}\right)\exp\left(-\frac{3z^2}{c^2}\right) * pulse(t)$</td><td colspan="2">$q_{applied}$: heat source of the laser beam (W/m^3)
A:absorption coefficient
P:laser peak power (kW)
a and b: laser beam radius (mm)
c:depthof the volumetric heat sourceequalto the plate thickness (mm)
$pulse(t)$:laser pulse function of time</td></tr>
<tr><td><u>Convective heat flux</u></td><td>$q_{convection} = h\left(T_s - T_{amb}\right)$</td><td colspan="2">$T_s$-: surface temperature (K)
T_{amb}: ambient temperature (300K)
h: heat transfer coefficient ($W/m^2.K$)</td></tr>
<tr><td><u>Diffuse surface (Radiation)</u></td><td>$q_{radiation} = \varepsilon\sigma\left(T_s^4 - T_{amb}^4\right)$</td><td colspan="2">$\varepsilon$: emissivity
σ : Stefan Boltzmann constant (5.6703×10^{-8} W/m^2K^4)</td></tr>
<tr><td>Governing equations for CFD model</td><td>$\rho\frac{\partial \mathbf{u}}{\partial t} + \rho(\mathbf{u}.\nabla)\mathbf{u} = \nabla.\left[-p\mathbf{I} + \mu\left(\nabla\mathbf{u} + (\nabla\mathbf{u})^T\right)\right] + \mathbf{F} + \rho\mathbf{g}$
$\rho\nabla.(\mathbf{u}) = 0$
$\mathbf{u}$ - velocity vector (m/s)
p - fluid pressure (Pa)
μ - dynamic viscosity (Pa.s)
μ_T -turbulent viscosity (Pa.s)
$\mathbf{F}$ - external forces applied to the fluid(N/m^3)
$\mathbf{I}$ - identity matrix
$\mathbf{g}$ - acceleration due to gravity (m/s^2)
Re - Reynolds number
σ -Cauchy stress tensor (N/m^2)
G - reciprocal wall distance (m)
l_w - charactistics length of the fluid (m)
u_τ - friction velocity (m/s)</td><td>$\rho\frac{\partial \mathbf{u}}{\partial t} + \rho(\mathbf{u}.\nabla)\mathbf{u} = \nabla.\left[-p\mathbf{I} + (\mu+\mu_T)\left(\nabla\mathbf{u} + (\nabla\mathbf{u})^T\right)\right] + \mathbf{F} + \rho\mathbf{g}$
$\rho\nabla.(\mathbf{u}) = 0$
$\mathrm{Re}_w = \frac{\rho\lvert\mathbf{u}\rvert l_w}{\mu} = \frac{\lvert\mathbf{u}\rvert}{u_\tau}.\frac{\rho u_\tau l_w}{\mu} = u^+ l_w^+,$
$u^+ = f\left(l_w^+\right) = \frac{U}{u_\tau}$
$\nabla G.\nabla G + \sigma_w G(\nabla.\nabla G) = (1+2\sigma_w)G^4,$
$l_w = \frac{1}{G} - \frac{l_{ref}}{2}$
$\mu_T = \mu\left(\left(\frac{df}{dl_w^+}\right)^{-1} - 1\right)$
U - Local flow velocity (m/s); u_τ - friction velocity (m/s); u^+ - dimensionless friction velocity;</td><td>$\rho\frac{\partial \mathbf{u}}{\partial t} + \rho(\mathbf{u}.\nabla)\mathbf{u} = \nabla.\left[-p\mathbf{I} + (\mu+\mu_T)\left(\nabla\mathbf{u} + (\nabla\mathbf{u})^T\right)\right] + \mathbf{F} + \rho\mathbf{g}$
$\rho\nabla.(\mathbf{u}) = 0$
$\rho\frac{\partial k}{\partial t} + \rho(\mathbf{u}.\nabla)k = \nabla.\left[\left(\mu + \mu_T\sigma_k^*\right)\nabla k\right] + P_k - \beta_0^*\rho\omega k$
$\rho\frac{\partial \omega}{\partial t} + \rho(\mathbf{u}.\nabla)\omega = \nabla.\left[(\mu + \mu_T\sigma_\omega)\nabla\omega\right] + \alpha\frac{\omega}{k}P_k - \rho\beta_0\omega^2$
$\mu_T = \rho\frac{k}{\omega}$
$P_k = \mu_T\left[\nabla\mathbf{u} : \left(\nabla\mathbf{u} + (\nabla\mathbf{u})^T\right)\right]$
k : turbulent kinetic energy (m^2/s^2); ω : specific dissipation rate (1/s); α , σ_k^* , σ_ω , β_0 , β_0^* : turbulence model parameters;</td></tr>
</table>

	l_{ref} - fluid reference length (m)		
Momentum in x and y-directions	$F_x = -\frac{C(1-f_l)^2}{b+f_l^3}u$ $F_y = -\frac{C(1-f_l)^2}{b+f_l^3}v + \rho g\beta(T-T_{ref})$		*C*:mushy zone constant10e5kg/(m^3.s); *b*:small number (0.001) to avoid division by zero; f_l: liquid fraction; g : gravitational constant (9.8067 m/s^2) β : coefficient of thermal expansion(1/K); T_{ref} : liquidus temperature (K) $\rho g\beta(T-T_{ref})$: boussinesq approximation for the buoyancy forces
Marangoni	$\left[-p\mathbf{I}+\mu\left(\nabla\mathbf{u}+(\nabla\mathbf{u})^T\right)-\frac{2}{3}\mu(\nabla.\mathbf{u})\mathbf{I}\right]\mathbf{n}=\gamma\nabla_{\mathbf{t}}T$		γ : temperature derivative of the surface tension N/(m.K) $\nabla_{\mathbf{t}}T$: surface temperature gradient

5.2.2. Experimental setup

The experiment on Nd:YAG laser keyhole welding is carried out at CMERI Durgapur, on a 1.5 mm thick Duplex stainless steel with pulsed wave. The experiments are carried out on a 2205 DSS sheet of dimensions 100 mm × 20 mm × 1.5 mm. In the present study, only one experiment is conducted with a peak power of 3.750 kW, scanning speed of 5.5 mm/s, beam radius of 0.75 mm, pulse duration of 4.8 ms and laser frequency of 25 Hz in order to compare the weld shape of three numerical models with the experimental one. Argon gas is used as the shielding gas at a flow rate of 7 L/min. The scheme of phenomena in laser welding is shown in Figure 5.5. The welding sample is cleaned with acetone before the process to remove the oil and oxide films. The Nd:YAG laser machine which is used to conduct the experiment is shown in Figure 5.6.

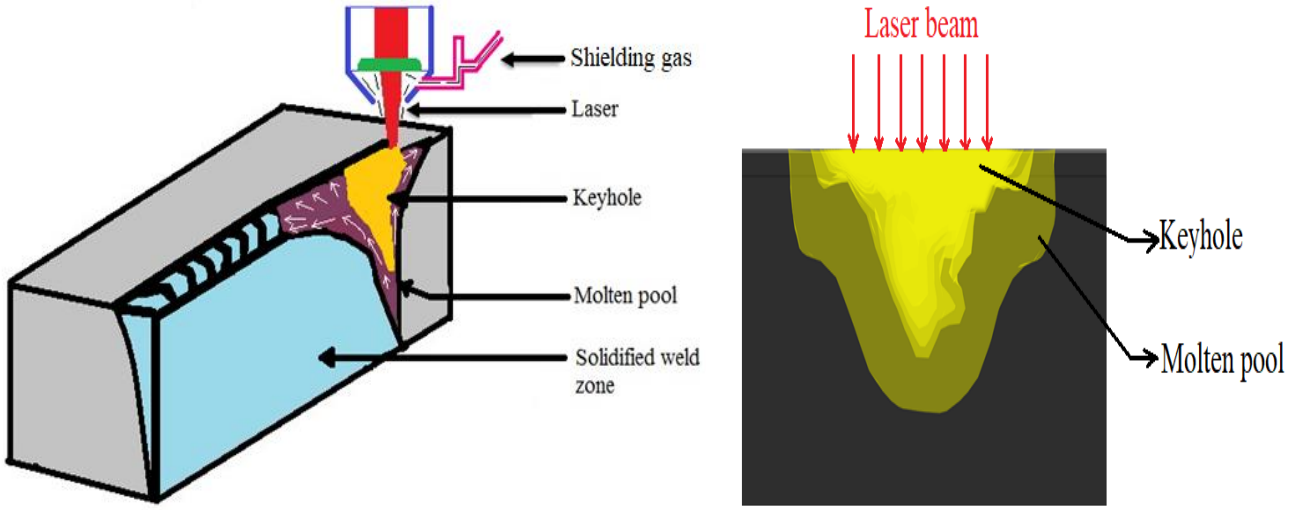

Figure 5.5 Scheme of phenomena in laser welding

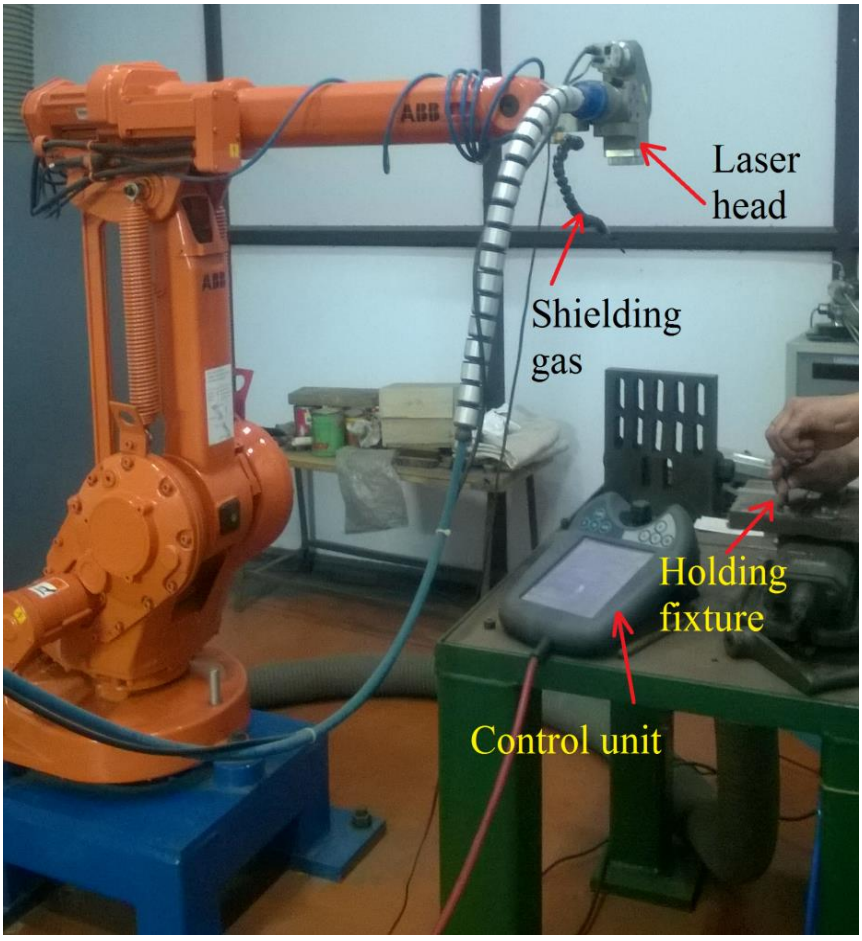

Figure 5.6 Nd:YAG laser machine setup for laser welding

5.3. Results and Discussion

In the results and discussion section, contours of temperature with total heat flux field, the width of the weld, the depth of the weld, the volume of the molten pool, formation of the keyhole and velocity field in the molten pool are presented for the three simulated models along with experimental results at t= 0.6848 s during pulsed laser welding of 2205 duplex stainless steel.

5.3.1. Temperature iso-surfaces and heat flux vectors in the molten pool

Figures 5.7 (a-d) show the contours of temperature at different locations on the plate for the three selected models, and the arrows indicate the velocity vector.

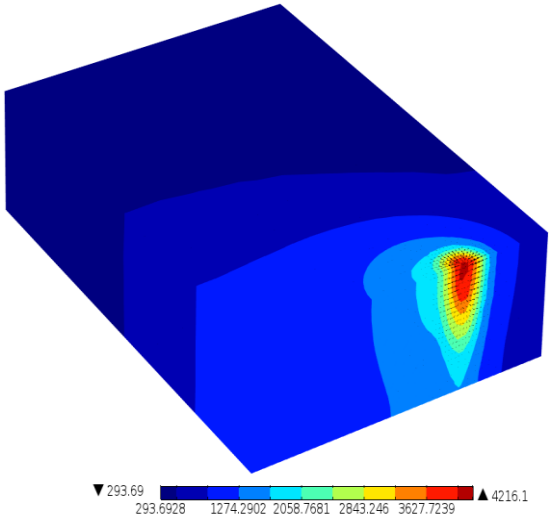

(a) Unmagnified view of Laminar model

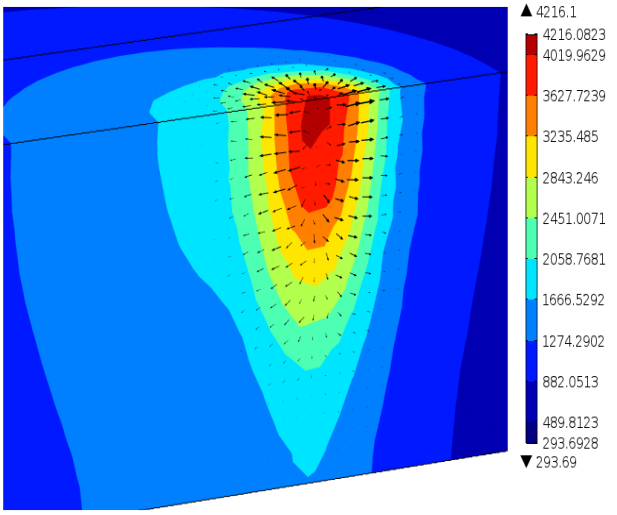

(b) Magnified view of Laminar model

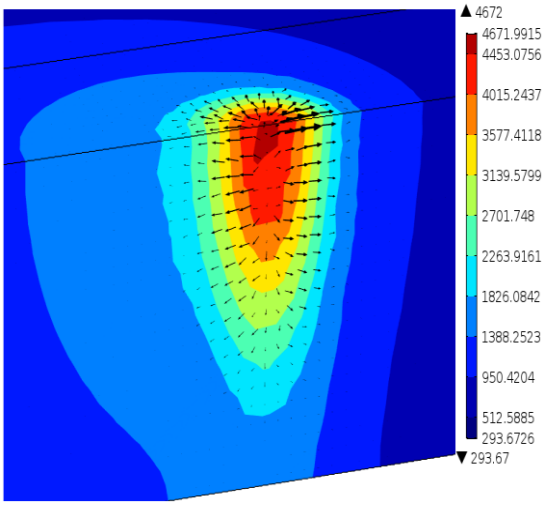

(c) Magnified view of yPlus model

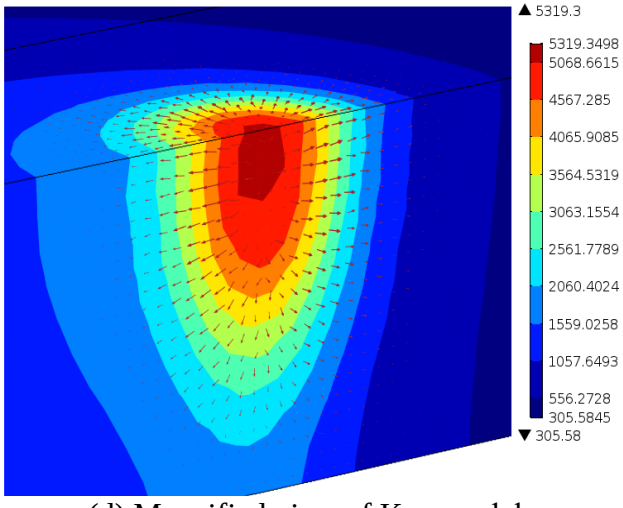

(d) Magnified view of K-ω model

Figure 5.7 Contours of temperature and total heat flux vectors in the molten pool

5.3.2. Width of the weld

Figure 5.8(a) shows the cross-sectional (front view) profiles of the experimental workpiece and the same for the three numerical models are shown in figures 5.8(b-d). Since the model is considered symmetric, only half of the weld width is shown in these figures. The width of the weld is measured at five equi-spaced locations from the top to the bottom of the plate surface. It can be observed from figures that there is a considerable difference in the width of weld for laminar and yPlus models than that obtained from the experimental result. On the contrary, the closest agreementof weld width is obtained from turbulent k-ω model.It is also seenthat the calculated widths of the weld from laminar and yPlus models indicate almost identical to each other. Table 5.4 summarises the weld width at five locations obtained from experimental observations and numerical models and their percentage deviation.

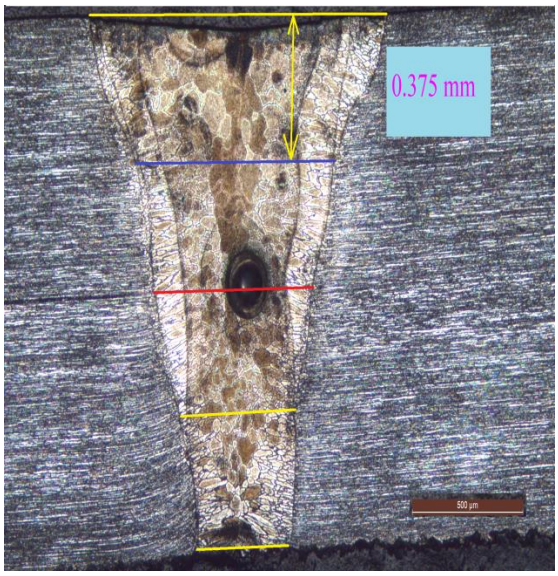

a) Locations of the measured experimental weld width

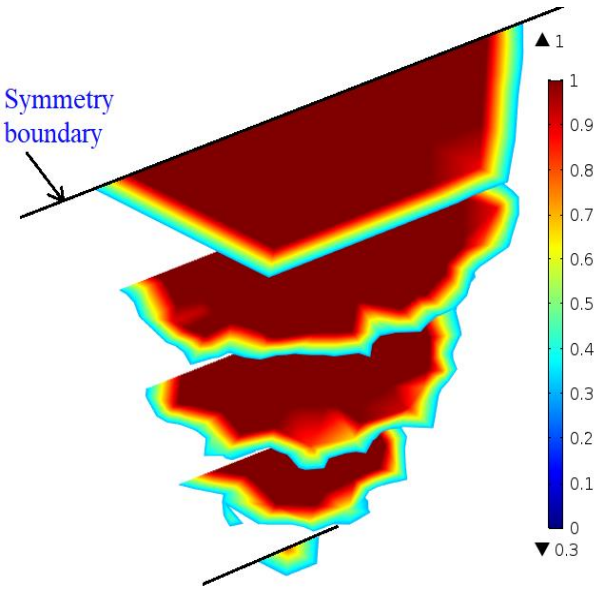

b) Laminar model weld width

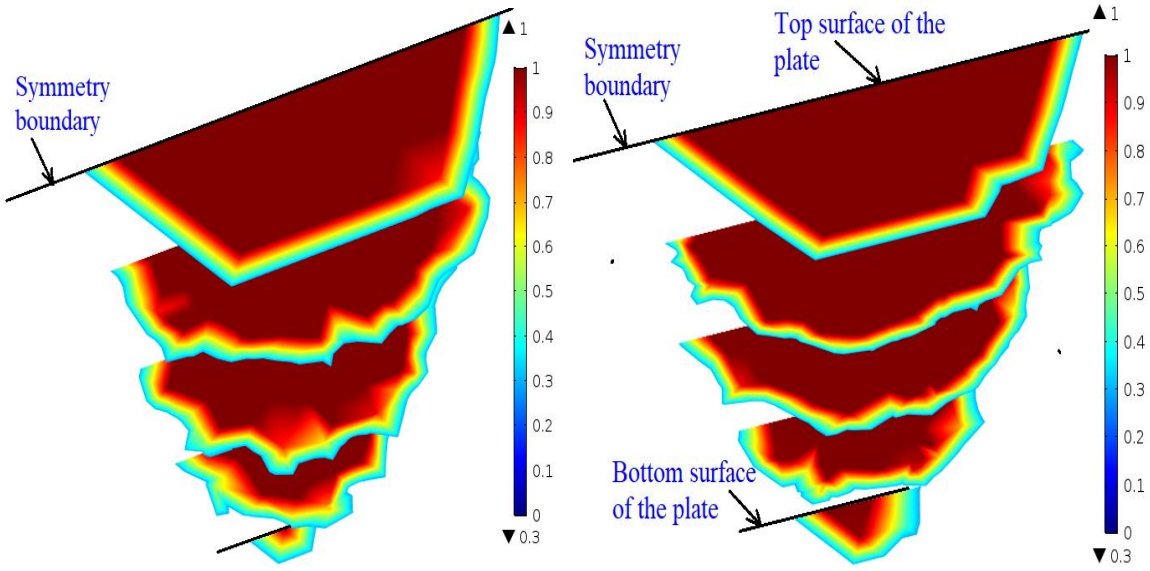

c) yPlus model weld width d) k-ω model weld width

Figure 5.8 Comparison of the numerically obtained weld width with experiment

Table 5.3 Comparison of experimental and simulation results for width of the weld

Sl. No	Experimental		Laminar model		yPlus model		k-ω model	
	Total width (mm)	Half width (mm) Ex_w	La_w (mm)	% Error $\frac{(Ex_w - La_w)}{Ex_w} \times 100$	yP_w (mm)	% Error $\frac{(Ex_w - yP_w)}{Ex_w} \times 100$	$k\omega_w$ (mm)	%Error $\frac{(Ex_w - k\omega_w)}{Ex_w} \times 100$
1	1.362	0.681	0.42	38.07636	0.424	37.76799	0.637	6.417034
2	0.927	0.464	0.4	14.64941	0.396	14.51996	0.566	-22.1359
3	0.735	0.368	0.37	-1.06122	0.367	0.081633	0.456	-23.9728
4	0.537	0.269	0.24	12.32775	0.254	5.437616	0.308	-14.5624
5	0.435	0.218	0.02	89.6092	0.036	83.49425	0.174	20

5.3.3. Depth of the weld

Figures 5.9 (a-c) show the cross-sectional (ZX-Plane) depth of the weld during laser welding of DP steel. It is observed that turbulent k-ω model predicts a wider and deeper weld fusion zone than other two models considered. Even so, the predicted weld pool shapeof these two othermodels also approaches the bottom of the plate surface which can be noticed from figures 5.10 (a) and (b).Therefore, using turbulent k-ω model which solves additional transport equations, it is feasible to find the appropriate the weld pool dimensions which matches fairly well with those obtained fromthe experimental weld pool geometry.

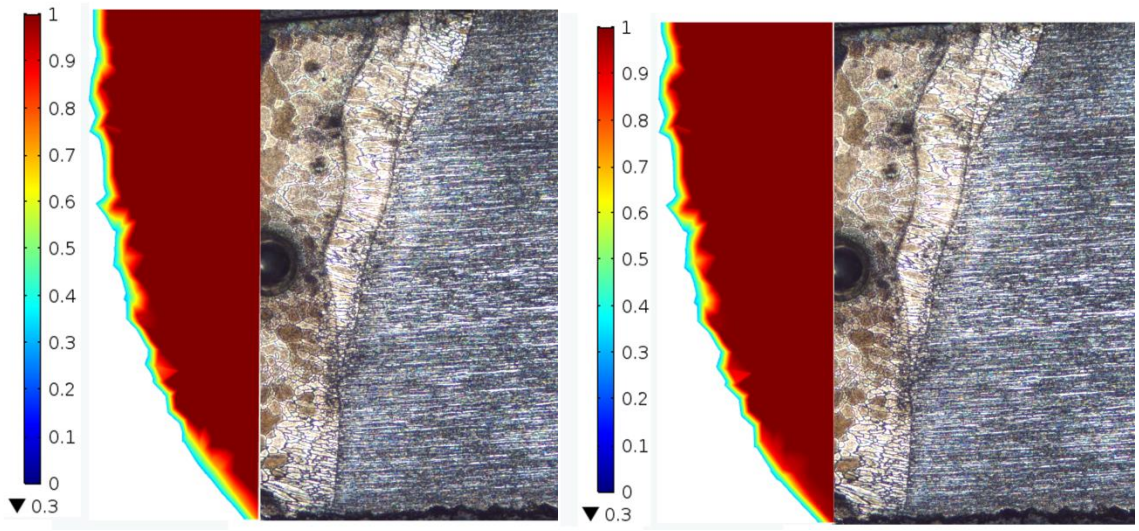

(a) Experiment Vs Laminar model weld depth

(b) Experiment Vs yPlus model weld depth

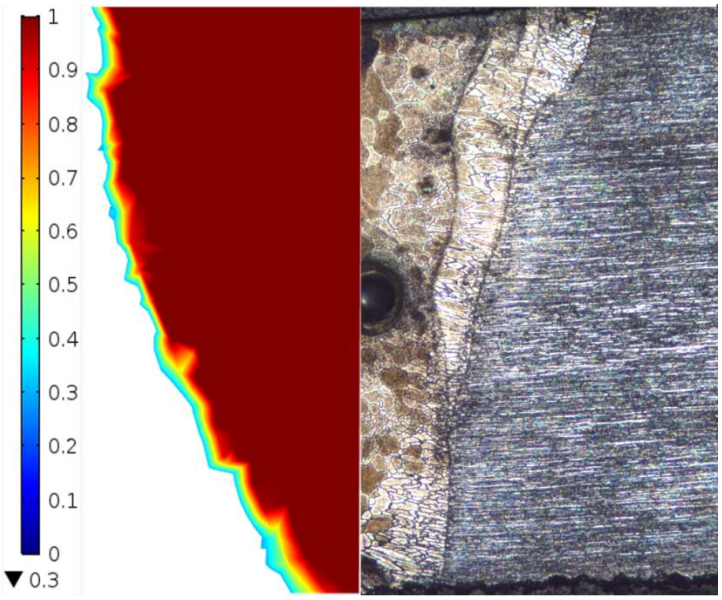

(c) Experiment Vs k-ω model weld depth

Figure 5.9 Comparison of the numerically obtained weld depth with experiment

5.3.4. Volume of the molten pool

Figures 5.10 (a-c) show the volume of the molten pool with a surface arrow plot which indicate the velocity vectors during the process. It is noticed that the liquid moves from the center of the fusion zone to its edge in the three models. Generally, steel plates used have negative surface tension gradient since it containsless sulphur (S < 30 ppm), thus, flow is taking place in-to-out in the molten pool. However, the turbulent k-ω model predicts a little

intense flow at the bottom of the plate surface compared to other two models.This intense flow leads to achieve a betterprediction of the weld bead geometries with the experimental results, although the direction of the liquid flow is nearly identical among the three models. It is better to avoid the laminar model to investigate the flow behaviour inside the molten pool although ittakes minimum computational time. The k-ω model, predicts a molten pool volume of 0.739 mm^3 whereas the laminar and yPlus models predict 0.410 mm^3 and 0.412 mm^3, respectively, as can be seen in figure 5.11.

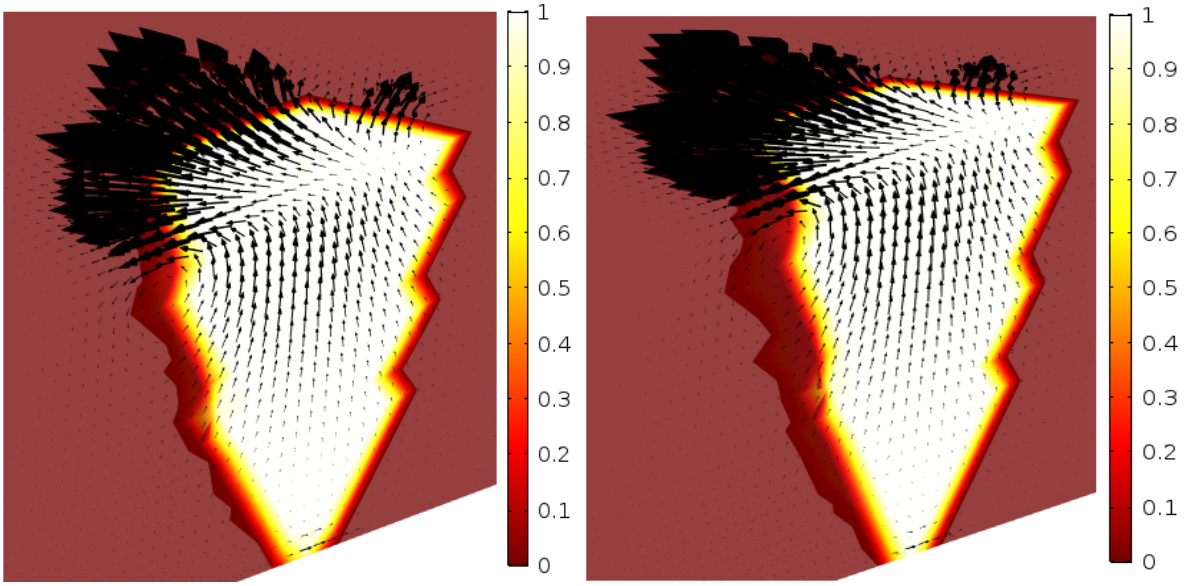

(a) Volume of the molten pool (Laminar) (b) Volume of the molten pool (yPlus)

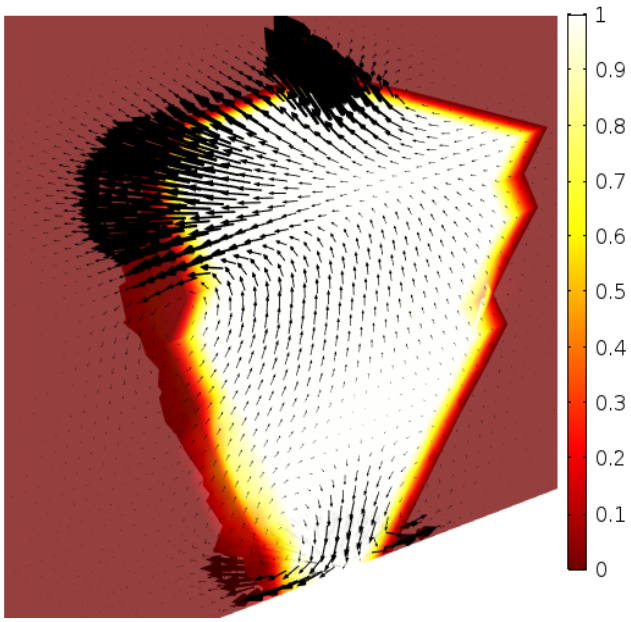

(c) Volume of the molten pool (k-ω model)

Figure 5.10 Comparison of the numerically obtained volume of the molten pool

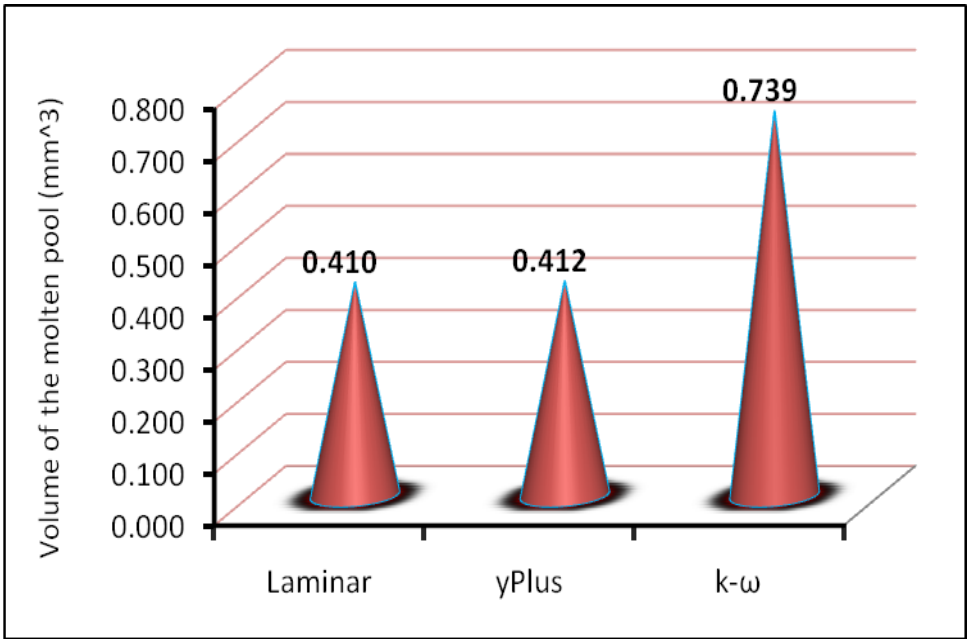

Figure 5.11 Volume of the molten pool for three models

5.3.5. Keyhole formation

Figures 5.12(a-c) depict the developed keyhole along with molten pool for the three models at t=0.6848 s. Till date, most of the literature suggests a large number of studies has been conducted on the development of keyhole with time during the welding process. However, the present study mostly deals with the selection of the suitable numerical model which can be used to investigate the flow behaviour in the molten pool. So, the study of the evlutionof the keyhole with time is not discussed here.However, the shape of the keyhole at a particular time instant is discussed here. From the simulation results, it is observed that the depth and volume of the keyhole also varyfromnumerical model to model. The maximum depth of the keyhole is obtained for the k-ω model followed by yPlus and laminar models. This is because of the fact that maximum temperature is achieved usingthe plate for K-ω model in comparison to those fromthe other two models.

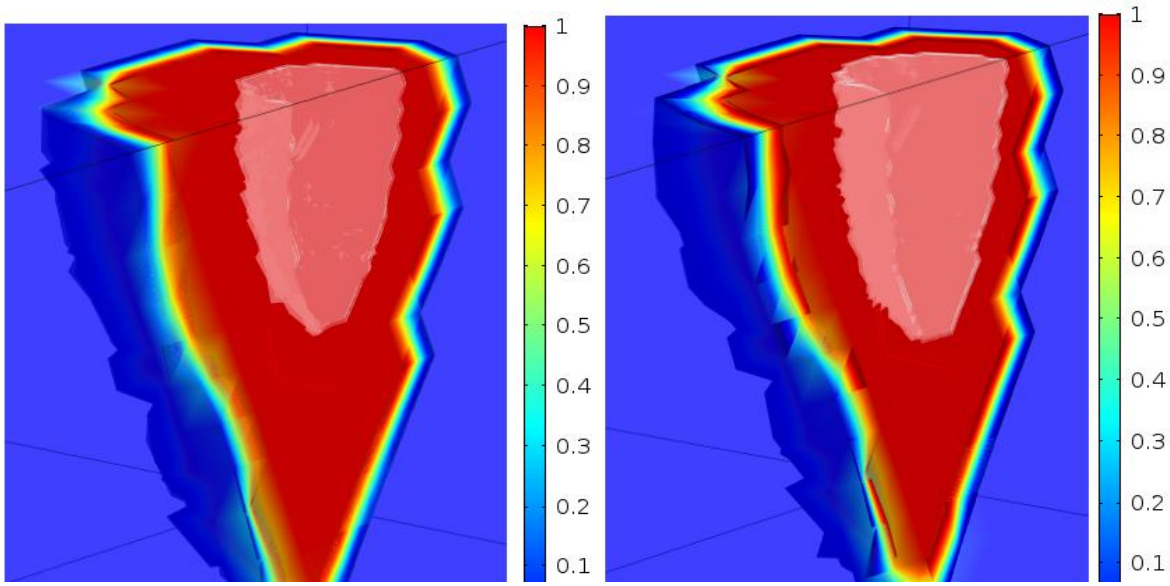

(a) Molten pool with keyhole (Laminar) (b) Molten pool with keyhole (yPlus)

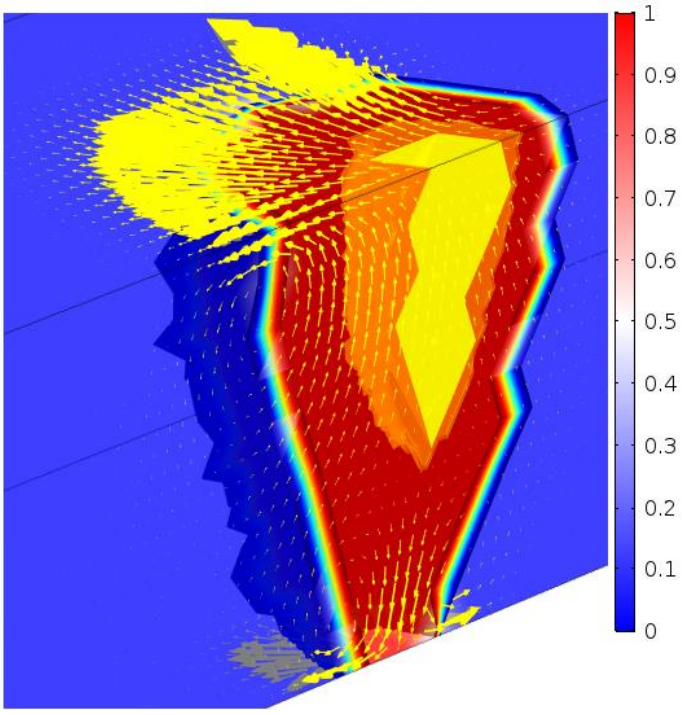

(c) Molten pool with keyhole (k-ω model)

Figure 5.12 Comparison of the numerically obtained keyhole

5.3.6. Velocity field in the molten pool

Figures 5.13(a-c) show the iso-surfaces of velocity with velocity vectors in the symmetry plane of the weld pool along the welding line. It is observed that the flow behaviour at the top surface is mainly influenced by Marangoni convection due to a high surface tension gradient.

Because, the flow is directed from the hot center region to the boundaries which are atmelting temperature. Moreover, due to lift force caused by buoyancy, the liquid moves towards to the top surface from the bottom of the weld pool. However, compared to Marangoni effect, buoyancy has much little influencefor thecase ofthe thin plates. That is why, the peak values in the velocity magnitude are located at the free edge of the molten pool and moves towards the edge of the weld pool for all models. The maximum fluid velocity is obtained at about 0.3602 m/s fromthe k-ω model. The maximum fluid velocities for laminar and yPlus models are obtainedas 0.2049 m/s and 0.237 m/s, respectively.Moreover, the dimensionless numbers (Marangoni, Grashof) are calculated to describe the intensity of the flow within the molten pool. The Marangoni number is one of the determining numbers that characterise the flow in laser molten pools. Generally, Marangoni numbers in laser molten pools vary between 10^2-10^5.The flow becomes turbulent if Marangoni number exceeds the value of 10^5.In the present study, the values of Marangoni numbers obtained from laminar, yPlus and k-ω models are 9.37×10^3, 1.03×10^4, and 1.89×10^4 respectively. The obtained values indicate that the flow in the molten pool may be a steady one. The obtained Marangoni numbers are shown in figure 5.14. Moreover, the characteristics of the flow in laser molten pools is determined by one more dimensionless number, that isGrashof number. The calculated value of the Grashof number from figure 5.15 shows that the fluid flow inside the melt pool is dominated by the surface tension force (Marangoni convection), while Buoyancy force plays a negligible role.The time taken for each computational model is listed in Table 5.5.

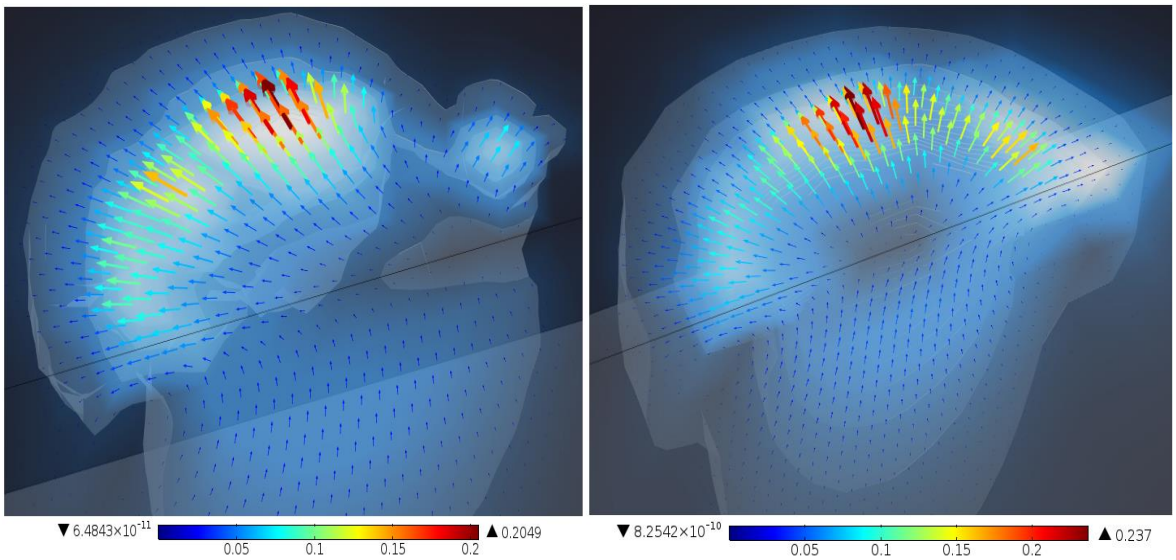

(a) Velocity magnitude(Laminar) (b) Velocity magnitude(yPlus)

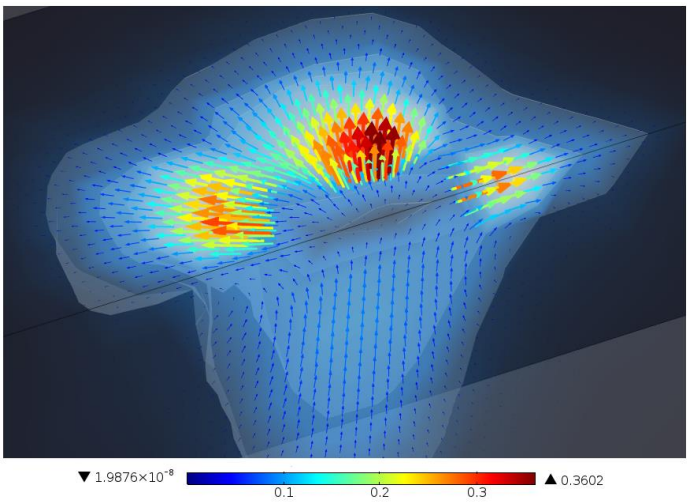

(c) Velocity magnitude(K-ω model)

Figure 5.13 Comparison of the numerically obtained velocity magnitude distribution

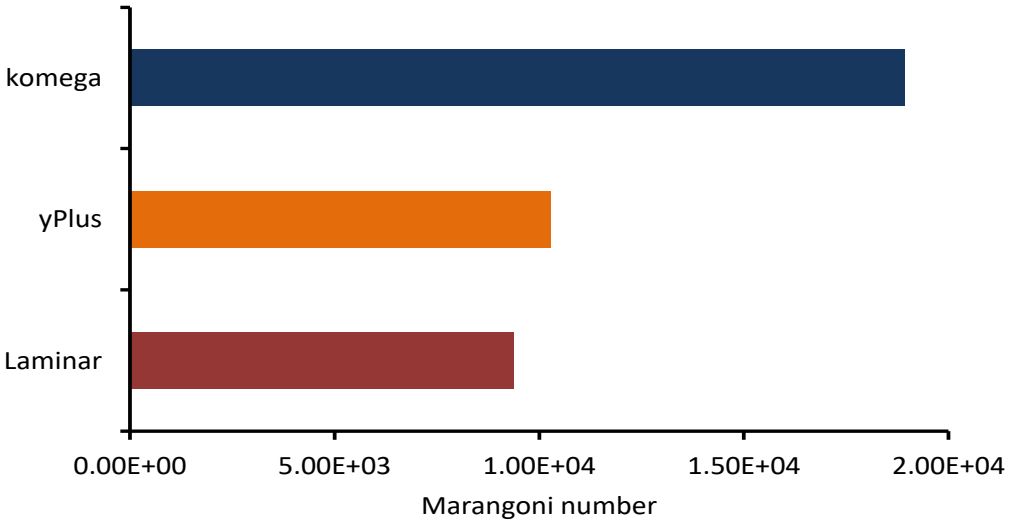

Figure 5.14 Numerically calculated Marangoni numbers

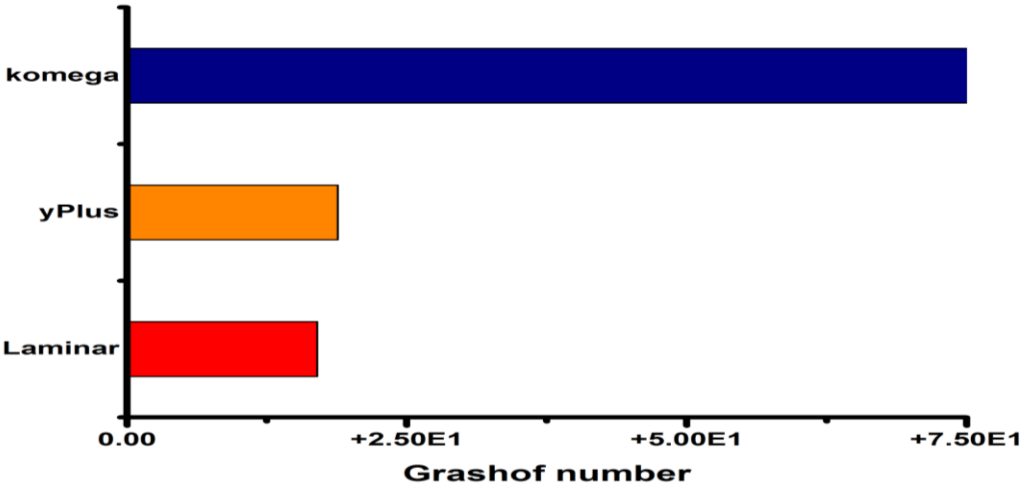

Figure 5.15 Numerically calculated Grashof numbers

Table 5.4 Performance of the computational domains

Numerical models	No of elements	Computational time
Laminar	42,866 tetrahedral 3-D elements	8 hrs, 53 min, 28 s
yPlus		14 hrs, 59 min, 32 s
k-ω		4 days, 15 hrs, 20 min

5.3.7. Comparison of experimental results with all simulation models(CFD, Anisotropic, Isotropic)

We have compared the experimental results for bead width and depth of penetration of welding and listed in table 5.5 (bead width) and table 5.6 (depth of penetration). It is evident from both the tables that experimental result matches best with CFD model in comparison to anisotropic and isotropic model.

Figures 5.16 (a-c) show the comparative view of experimental cross-sectional area with CFD, anisotropic and isotropic model (ZX-Plane) cross-sectional area for the weld during laser welding of Duplex steel. It is observed that using CFD turbulent k-ω model, it is feasible to find the appropriate weld pool dimensions which matches fairly well with those obtained from the experimental weld pool geometry than anisotropic and isotropic model.

Table 5.5 Comparison of experimental, CFD model simulation, Anisotropic model simulation and Isotropic model simulation results for Bead width of the weld

Sl. No.	Experimental	k-ω model (CFD)	Anisotropic model	Isotropic model
1	1.362	1.274	1	0.8
2	0.927	1.132	0.76	0.6
3	0.735	0.912	0.4	0.3
4	0.537	0.616	0	0
5	0.435	0.348	0	0

Table 5.6 Comparison of experimental, CFD model simulation, Anisotropic model simulation and Isotropic model simulation results for Depth of penetration of the weld

Experimental	k-ω model (CFD)	Anisotropic model	Isotropic model
1.5	1.5	1.1	0.82

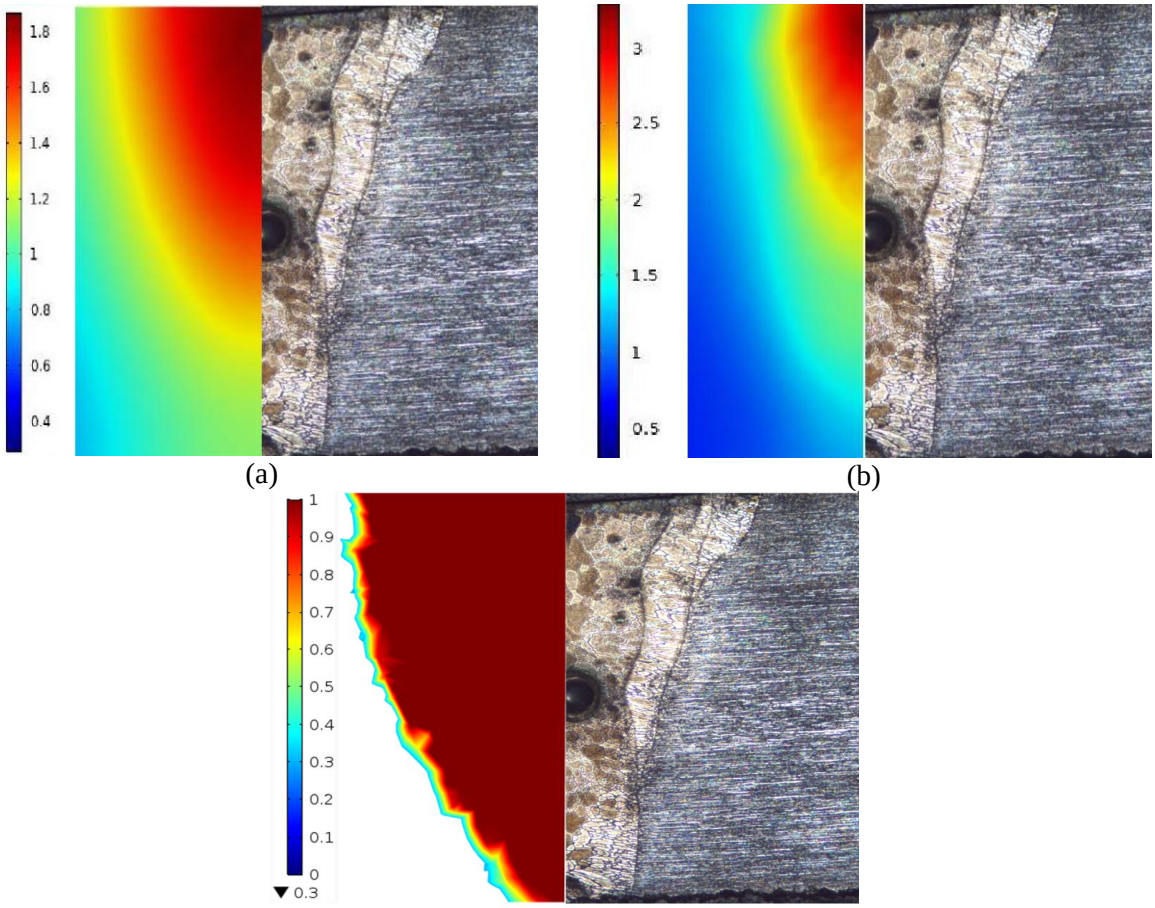

Figure 5.16 Comparison of the numerically obtained weld depth with experiment: (a) Isotropic model vs experimental result, (b) Anisotropic model vs experimental result, (c) CFD model vs experimental result

5.4. Conclusion

Flow behaviour during pulsed laser beam welding of 2205 duplex stainless steel is investigated through three numerical models such as laminar, yPlus and turbulent k-ω. The temperature and velocity fields in the molten pool are simulated through the considered models. The numerically calculated weld bead geometries are validated with experimental results and fair agreements are obtained. The following conclusions can be drawn from the present study.

1. The obtained Peclet numbers from three models confirms that the convective heat transfer rate is more dominant one over conductive heat transfer rate in the molten pool.
2. Laminar and algebraic yPlus turbulence models are robust and least computationally intensive compared to the other turbulence model. Moreover, it does not require to solve any additional transport equation. Since they are generally the least accurate

models, the weld bead geometries obtained from these two models are not very close to the experimental observations. On the other hand, the turbulent k-ω model provides a wider and deeper weld fusion zone which is closer to the experimental findings than othertwo considered models.

3. The k-ω model predicts amolten pool volume of 0.739 mm^3 whereas the laminar and yPlus yield 0.410 mm^3 and 0.412 mm^3, respectively. However, by comparing three models, the direction of the liquid flow and the flow patterns are almost identical. So, one can choose the laminar model to investigate the flow behaviour inside the molten pool, since it requires the least computational time and the k-ω model can be used to predictthe appropriate weld bead geometries and dimensions.
4. The liquid flow is directed from the hot center region to the boundaries of the molten pool. The peak values in the velocity magnitude are located at the free edge of the molten pool and moves towards the edge of the weld pool for all models which indicates that flow is mainly influenced by Marangoni convection due to surface tension forces.
5. The value of Marangoni numbers obtained from thelaminar, yPlus and k-ω models are 9.37×10^3, 1.03×10^4, and 1.89×10^4 respectively. Similarly, Grashofnumbers obtained from the laminar, yPlus and k-ω models are 16.9815, 18.8088, and 78.1247, respectively. The obtained dimensionless numbers indicatethat the flow is steady in the molten pool during pulsed laser beam welding of 2205 duplex stainless steel.
6. The comparison between experimental result with Isotropic, Anisotropic and CFD model reveals that CFD model offeres best match with experiment in terms of bead width and depth of penetration.

Chapter 5

CHAPTER 6

General Conclusions and Future Scope

6.1 General Conclusions

A comparative investigation among numerical and experimental procedure of laser welding of 2205 duplex stainless steel for but joint is carried out in present research to realize optimum process parameters for achieving satisfactory weld joint properties. In this laser welding process, laser power, welding speed, beam diameter and pulse width are considered as process parameters to obtain full depth of penetration, narrow bead width, maximum ultimate tensile strength (UTS) and maximum ductility or elongation as response parameters. The observations and findings in the present thesis can be concluded as follows:

1. A three-dimensional thermal analysis of laser welding, with transient heat source, is performed through designing a numerical model using finite element method, considering phase change, employing COMSOL MULTIPHYSICS software. The model is developed considering conduction mode heat transfer, to classify constraining standards of process parameters for acquiring desirable response values. At the beginning we considered isotropic approach and primarily compared the simulated results with published work of Batahgy (2011) and Shanmugam (2012) and observed that though the results from present numerical model are in good agreement with published results, it needs improvement.
2. Applying this method, we completed an array of simulations and developed correlation among process and response parameters employing response surface methodology and depending on multiobjective optimisation criterion optimum process parameters are identified through Design Expert 7.0 software to get a safe operating window.
3. Optimum solution obtained as: At power 400 W, welding speed 683.82 mm/min and beam diameter 0.7 mm minimum bead width and maximum depth of penetration is achieved.
4. In the next step we decided to apply anisotropic approach in simulation model to get more accuracy in results as isotropic properties are not exactly followed in actual heat transfer method. We have completed a number of experimental studies with same process parameters and validated experimental results with anisotropic based simulation model. The comparison shows an improved match between simulation and experimental results in respect to bead width and depth of penetration. Microstructure of welds are inspected with the help of optical microscope and SEM to measure depth of penetration and bead width. Though in numerical method we can predict only

depth of penetration, bead width and maximum temperature but in reality, the quality of weld depends also on the strength and ductility of the joints. In experimental investigations we studied mechanical properties such as ultimate tensile strength, elongation, microhardness of weld joints as well as base metal. We noticed a clear change of strength and elongation in weld joints compared to the base metal. Based on simulated results from anisotropic approach the optimum condition which we found earlier in isotropic approach has been differed as mechanical property inclusion was done. In this case we acquire maximum depth of penetration, minimum bead width, maximum UTS, maximum elongation and maximum microhardness at Power 425 W, welding speed 5 mm/s and pulse width 5 ms.

5. Hence the inclusion of mechanical properties in output response while identifying the optimum process parameters is felt necessary. So, we have designed a matrix of varied process parameters for experimental investigations and evaluated the responses like depth of penetration, bead width along with ultimate tensile strength and elongation and to achieve an optimal set of process parameters. Besides, functional correlation between process and response parameters is developed using the same statistical analysis method named Response surface methodology employing design expert 7.0 software. Here we found again a different set of optimum conditions which ensures better mechanical properties along with better bead geometry for laser weld samples.
6. Optimum process parameters obtained are as: At power 427.145 W, welding speed 5.353 mm/s and pulse width 5.4 ms desired bead width, maximum depth of penetration, maximum UTS and maximum elongation is achieved.
7. Only considering anisotropic approach for simulation of welding process is not enough because it is obvious to consider fluid flow as in reality there is a situation where molten metals flow. Hence to achieve more accurate simulation it is required to include the CFD in finite element method for simulation. Three numerical models are employed using COMSOL Multiphysics for thin plates considering the flow in the molten pool to be laminar in the first model and turbulent (yPlus and k-ω model) in the two other models. The simulated results for bead width and depth of penetration, of these three models are compared with experimental investigation for one set of process parameters and it is identified that bead geometry obtained from k-ω model is closer to the experimental findings than other two models. With CFD approach,

optimization of process parameters is not accomplished as it is a long process, so we decided to explore this in future.

8. We also designed two simulation programs with same process parameters in anisotropic and isotropic model to compare the results i.e., bead width and depth of penetration, with CFD model and experimental study. The comparative study reveals that the bead geometry of CFD model offers best match with experiment than the bead geometry of anisotropic and isotropic model.

6.2 Future Scope

The present research is restricted in thermal analysis for numerical model which is capable of predicting bead width and depth of penetration only. In experimental study we have done one kind of joints where in diverse industries different types of joints are extensively used. We compared experimental and numerical investigations for one set of process parameters while every set of input can produce diverse outcomes. Moreover, in present research only depth of penetration and bead width was compared while mechanical deformation is also very much important in welding process. So future work can be explored in subsequent guidelines.

1. In future, we will try to incorporate mechanical analysis in this model to evaluate mechanical deformation of weld joints.
2. After incorporating CFD approach we did not done optimization of process parameters, in future we will find optimum condition for this approach and observe the difference from other simulation model and experiments. In next step we will correlate CFD simulations with experiments and will try to develop mathematical equations to predict other mechanical responses.
3. Additionally, we can compare every set of experiments with simulation model (CFD) and we will evaluate a detailed comparative study not only among depth of penetration and bead width but also for mechanical properties like ultimate tensile strength and elongation.
4. In further research other types of weld joints such as T, lap can be explored considering numerical and experimental investigations for getting better insight of the process and to be used more extensively in various industry applications.

Bibliography

1. Sathiya P., Abdul Jaleel M.Y., Katherasan D. and Shanmugarajan B. Optimization of laser butt welding parameters with multiple performance characteristics. Optics & Laser Technology 43(3) (2011), 660–673.
2. Frewin M. and Scott D. Finite element model of pulsed laser welding. Welding Research Supplement (1999), 15–22.
3. De A., Maiti S., Walsh C. and Bhadeshia H. Finite element simulation of laser spot welding. Science and Technology of Welding and Joining 8(5) (2003), 377–384.
4. Benyounis K. and Olabi A. Optimization of different welding processes using statistical and numerical approaches – A reference guide. Advances in Engineering Software 39(6) (2008), 483–496.
5. Ming H.G., Jian Z. and Qang L.J. Dynamic simulation of the temperature field of stainless steel laser welding. Materials & Design 28(1) (2007), 240–245.
6. Anawa E.M. and Olabi A.G. Using Taguchi method to optimize welding pool of dissimilar laser-welded components. Optics & Laser Technology 40(2) (2008), 379–388.
7. Abderrazak K., Bannour S., Mhiri H., Lepalec G. and Autric M. Numerical and experimental study of molten pool formation during continuous laser welding of AZ91 magnesium alloy. Computational Materials Science 44(3) (2009), 858–866.
8. Belhadja A., Bessroura J., Masseb J.E., Bouhafsa M. and Barrallier L. Finite element simulation of magnesium alloys laser beam welding. Journal of Materials Processing Technology 210(9) (2010), 1131–1137.
9. Abhilash A.P. and Sathiya P. Finite element simulation of laser welding of 904L super austenitic stainless steel, Transactions of the Indian Institute of Metals 64(4-5) (2011), 409–416.
10. Batahgy A.M., Khourshid A.F. and Sharef T. “Effect of laser beam welding parameters on microstructure and properties of Duplex stainless steel”. Materials Sciences and Applications 2(10) (2011), 1443-1451.
11. Kumar C., Das M. and Biswas P. A 3-D finite element analysis of transient temperature profile of laser welded Ti-6Al-4V alloy. 5th International & 26th All

India Manufacturing Technology, Design and Research Conference (AIMTDR 2014). 12-14 December 2014, Guwahati, Assam, India.

12. Akbari M., Saedodin S., Toghraie D., Razavi R.S. and Kowsari F. Experimental and numerical investigation of temperature distribution and melt pool geometry during pulsed laser welding of Ti6Al4V alloy. Optics & Laser Technology 59 (2014), 52–59.
13. Azizpour M., Ghoreishi M. and Khorram A. Numerical simulation of laser beam welding of Ti6Al4V sheet. Journal of Computational and Applied Research 4(2) (2015), 145-154.
14. Kumar S. Numerical modeling and simulation of a butt joint welding of AISI 316L stainless steels using a pulsed laser beam. Materials Today: Proceedings 2(4-5) (2015), 2256–2266.
15. Acherjee, B., Kuar, A.S., Mitra, S., Misra, D.: Effect of carbon black on temperature field and weld profile during laser transmission welding of polymers: a FEM study. Opt Laser Technol. 44, 514–521 (2012)
16. Daha, M.A., Nassef, G.A., Abdallah, I.A., AbouSeeda, H.M.: Three-dimensional thermal finite element modeling for keyhole plasma arc welding of 2205 duplex stainless steel plates. International Journal of Engineering and Technology. 2(4):720-728 (2012)
17. Daneshkhah, R., Najafi, M., Torabian, H.: Numerical simulation of weld pool shape during laser beam welding. International Research Journal of Applied and Basic Sciences. 3(8), 1624–1630 (2012)
18. Marimuthu, S., Eghlio, R.M., Pinkerton, A.J., Li, L.: Coupled computational fluid dynamic and finite element multiphase modeling of laser weld bead geometry formation and joint strengths. J Manuf Sci Eng. 135, 011004–011001 (2013)
19. Bannach N. (2014) Phase Change: Cooling and Solidification of Metal. Retrieved 12th June 2018, from https://uk.comsol.com/blogs/phase-change-cooling-solidification-metal/
20. Shanmugam N.S., Buvanashekaran G. and Sankaranarayanasamy K. Some studies on weld bead geometries for laser spot welding process using finite element analysis. Materials & Design 34 (2012), 412–426.
21. Acherjee, B., Kuar, A.S., Mitra, S., Misra, D., Acharyya, S.: Experimental investigation on laser transmission welding of PMMA to ABS via response surface modeling. Opt Laser Technol. 44, 1372–1383 (2012)

22. Montgomery D.C. Design and Analysis of Experiments. New York: Wiley. 2001.
23. Yang, Y., Yan, B., Li, J., Wang, J.: The effect of large heat input on the microstructure and corrosion behaviour of simulated heat affected zone in 2205 duplex stainless steel. Corros Sci. 53, 3756–3763 (2011)
24. Pekkarinen, J., Kujanpaa, V.: The effects of laser welding parameters on the microstructure of ferritic and duplex stainless steels welds. Phys Procedia. 5, 517–523 (2010)
25. Soltysiak, R.: Effect of laser welding parameters of duplex 2205 steel welds on fatigue life. Solid State Phenom. 223, 11–18 (2015)
26. Hu, S., Yang, B., Zeng, B., Zheng, D., Yang, Z.: Experimental study of laser welding process and properties of 2205 duplex stainless sheet steels. Mater Sci Forum. 861, 141–146 (2016)
27. Soltysiak, R., Gietka, T., Soltysiak, A.: The effect of laser welding power on the properties of the joint made of 1.4462 duplex stainless steel. Advances in Mechanical Engineering. 10(1), 1–12 (2018)
28. Hosseini, V.A., Bermejo, M.A.V., Gardstam, J., Hurtig, K., Karlsson, L.: Influence of multiple thermal cycles on microstructure of heat-affected zone in TIG-welded super duplex stainless steel. Weld World. 60, 233–245 (2016)
29. Zhang, Z., Jing, H., Xu, L., Han, Y., Zhao, L.: Investigation on microstructure evolution and properties of duplex stainless steel joint multi-pass welded by using different methods. Mater Des. 109, 670–685 (2016)
30. Asif, M.M., Shrikrishnaa, K.A., Sathiya, P., Goel, S.: The impact of heat input on the strength, toughness, microhardness, microstructure and corrosion aspects of friction welded duplex stainless-steel joints. J Manuf Process. 18, 92–106 (2015)
31. Capello, E., Chiarello, P., Previtali, B., Vedani, M.: Laser welding and surface treatment of a 22Cr-5Ni-/3Mo duplex stainless steel. Mater Sci Eng. A351, 334–343 (2003)
32. Safdar, S., Pinkerton, J.A., Li, L., Sheikh, A.M., Withers, J.P.: An anisotropic enhanced thermal conductivity approach for modelling laser melt pools for Ni-base superalloys. Appl Math Model. 37, 1187–1195 (2013)

33. Badji, R., Bouabdallah, M., Bacroix, B., Kahloun, C., Belkessa, B., Maza, H.: Phase trans-formation and mechanical behaviour in annealed 2205 duplex stainless steel welds. Mater Charact. 59, 447–453 (2008)
34. Mourada, A.H.I., Khourshid, A., Sharef, T.: Gas tungsten arc and laser beam welding processes effects on duplex stainless steel 2205 properties. Mater Sci Eng A. 549, 105–113 (2012)
35. Mirshekari, G.R., Saatchi, A., Kermanpur, A., Sadrnezhaad, S.K.: Laser welding of NiTi shape memory alloy: comparison of the similar and dissimilar joints to AISI 304 stainless steel. Opt Laser Technol. 54, 151–158 (2013)
36. Jia, Q., Guo, W., Li, W., Zhu, Y., Peng, P., Zou, G.: "Microstructure and tensile behavior of fiber laser-welded blanks of DP600 and DP980 steels". Journal of Materials Processing Technology. 236 (2017)
DOI:10.1016/j.jmatprotec.2016.05.011
37. Akman, E., Demir, A., Canel, T., Sınmazçelik, T. "Laser welding of Ti6Al4V titanium alloys". Journal of Materials Processing Technology. 209, 3705-3713 (2009). https://doi.org/10.1016/j.jmatprotec.2008.08.026
38. Kashaev, N., Ventzke, V., Fomichev, V., Fomin, F., Riekehr, S. "Effect of Nd:YAG laser beam welding on weld morphology and mechanical properties of Ti–6Al–4V butt joints and T-joints". Optics and Lasers in Engineering. 86(9), 172-180 (2016).
DOI:10.1016/j.optlaseng.2016.06.004
39. Lei, Z., Dong, Z., Chen, Y., Zhang, J., Zhu, R. "Microstructure and tensile properties of laser beam welded Ti–22Al–27Nb alloys". Materials & Design**.** 46, 151-156 **(**2013**).**
https://doi.org/10.1016/j.matdes.2012.10.022
40. Shanmugarajan, B., Shrivastava, R., Sathiya, P., Buvanashekaran, G.: Optimisation of laser welding parameters for welding of P92 material using Taguchi based grey relational analysis. Defence Technology. 12, 343–350 (2016)
41. Artinov, A., Bachmann, M., Rethmeier, M.: Equivalent heat source approach in a 3D transient heat transfer simulation of full-penetration high power laser beam welding of thick metal plates. International Journal of Heat and Mass Transfer. **122**, 1003–1013 (2018)

42. Bachmann, M., Avilov, V., Gumenyuk, A., Rethmeier, M.: “Multi-Physics Process Simulation of Static Magnetic Fields in High Power Laser Beam Welding of Aluminum”. COMSOL Conference (Milan, Italy) (2012)
43. Courtois, M., Carin, M., Masson, P., Gaied, S.: Keyhole formation during spot laser welding. heat and fluid flow modeling in a 2d axisymmetric configuration. Excerpt from the Proceedings of the 2012 COMSOL Conference in Milan (2012)
44. Zhao,H., Niu,W., Zhang, B., Lei,Y., Kodama,M.,Ishide,T.:Modelling of keyhole dynamics and porosity formation considering the adaptive keyhole shape and three-phase coupling during deep-penetration laserwelding.Journal of Physics D: Applied Physics.**44**, 485302 (13pp) (2011)
45. Ai, Y., Jiang, P., Shao, X., Li, P., Wang, C., Mi, G., Geng, S., Liu, Y., Liu W.: The prediction of the whole weld in fiber laser keyhole welding based on numerical simulation. Applied Thermal Engineering. **113**, 980–993 (2017)
46. Ai, Y., Jiang, P., Shao, X., Li, P., Wangc, C.: A three-dimensional numerical simulation model for weldcharacteristics analysis in fiber laser keyhole welding. International Journal of Heat and Mass Transfer. **108**, 614–626 (2017)
47. Kooa, B.S., Thasanaraphan, P., Niedc, H.F.:Numerical simulation of the formation of hourglass welds during laser welding.Journal of Materials Processing Technology. **263**, 176–185 (2019)
48. Gao, Z., Jiang, P., Mi, G., Cao, L., Wei, L.: Investigation on the weld bead profile transformation with the keyhole and molten pool dynamic behaviour simulation in high power laser welding. International Journal of Heat and Mass Transfer. **116**, 1304–1313 (2018)
49. Ramkumar KD, Mishra D, Vignesh MK, Raj BG, Arivazhagan N, Naren SV, Kumar SS (2014) Metallurgical and mechanical characterization of electron beam welded super-duplex stainless steel UNS 32750. J Manuf Process 16(4):527–534
50. Saravanan S, Raghukandan K, Sivagurumanikandan N (2017) Pulsed Nd: YAG laser welding and subsequent post-weld heat treatment on super duplex stainless steel. J Manuf Process 25:284–289
51. Sato YS, Nelson TW, Sterling CJ, Steel RJ, Pettersson CO (2005) Microstructure and mechanical properties of friction stir welded SAF 2507 super duplex stainless steel. Mater Sci Eng A 397(1-2):376–384

52. Luchtenberg P, Campos PT, Soares P, Laurindo CAH, Maranho O, Torres RD (2019) Effect of welding energy on the corrosion and tribological properties of duplex stainless steel weld overlay deposited by GMAW/CMT process. Surf Coat Technol 375:688–693
53. Pavan AR, Arivazhagan B, Vasudevan M, Prasanthi TN, Sudha C (2023) Study on the microstructure and mechanical properties of hybrid laser + MIG welded joints of 316LN stainless steel. Opt Laser Technol 163:109410
54. Karimi A, Karimipour A, Akbari M, Razzaghi MM, Ghahderijani MJ (2023) Investigating the mechanical properties and fusion zone microstructure of dissimilar laser weld joint of duplex 2205 stainless steel and A516 carbon steel. Opt Laser Technol 158:108875
55. Madhankumar S, Ashwin S, Robert JA, Francis JC, Kalyan RB, Raj AK, Anton WJ (2021) Experimental investigation on ultimate tensile strength of laser butt welded Inconel 718 alloy and 2205 duplex stainless steel. Mater Today: Proc 45:6783–6787
56. Ahmada GN, Raza MS, Singh NK, Kumar H (2020) Experimental investigation on Ytterbium fiber laser butt welding of Inconel 625 and Duplex stainless steel 2205 thin sheets. Opt Laser Technol 126:106117
57. Kose C, Topal C (2023) Dissimilar laser beam welding of AISI 2507 super duplex stainless to AISI 317L austenitic stainless steel. Mater Sci Eng A 862:144476
58. Mansur VM, Mansur RAF, Carvalho SM, Siqueira RHM, Lima MSF (2021) Effect of laser welding on microstructure and mechanical behaviour of dual phase 600 steel sheets. Heliyon 7:e08601
59. Kumar P, Sinha AN (2019) Effect of heat input in pulsed Nd:YAG laser welding of titanium alloy (Ti6Al4V) on microstructure and mechanical properties. Weld World 63:673–689
60. Ahmad GN, Raza MS, Singh NK, Muvvala G (2021) Investigating the effect of process parameters on weld pool thermal history and mechanical properties of laser welded Inconel 625 and Duplex stainless steel 2205 dissimilar welds. Optik 248:168134
61. Benyounis KY, Olabi AG, Hashmi MSJ (2008) Multi-response optimization of CO2 laser-welding process of austenitic stainless steel. Opt Laser Technol 40(1):76-87

62. Sunny KT, Korra NN, Arivazhagan B (2022) Parameter optimization and experimental validation of A-TIG welding of super austenitic stainless steel AISI 904L using response surface methodology. Proc Inst Mech Eng E: J Process Mech Eng 236(6):2608-2617
63. Sun H, Zhu J, Zhang B, Liu C, Miao C, Wang K, Zhao X (2022) Optimization of Laser-MAG Hybrid Welding Parameters of Ship Steel Based on Response Surface Methodology. Materials (Basel) 15(12):4328
64. Heydari H, Akbari M (2020) Investigating the effect of process parameters on the temperature field and mechanical properties in pulsed laser welding of Ti6Al4V alloy sheet using response surface methodology. Infrared Phys Technol 106:103267 DOI:10.1016/j.infrared.2020.103267
65. Cheepu M, Venkateswarlu D, Rao PN, Kumaran SS, Srinivasan N (2019) Optimization of Process Parameters Using Surface Response Methodology for Laser Welding of Titanium Alloy. Mater Sci Forum 969:539-545
66. Chellu PK, Padmanaban R, Vignesh RV, Menon AS, Shariff SM, Padmanabham G (2019) Experimental Study on Laser Welding of AISI 304 Steel with Design of Experiments Approach. IOP Conf Ser: Mater Sci Eng 577:012117
67. Torabi A, Kolahan F (2018) Optimizing pulsed Nd:YAG laser beam welding process parameters to attain maximum ultimate tensile strength for thin AISI316L sheet using response surface methodology and simulated annealing algorithm. Opt Laser Technol 103:300-310
68. Joyce, P., Radice, J., Tresansky, A., Watkins, J.: A COMSOL model of damage evolution due to high energy laser irradiation of partially absorptive materials. Excerpt from the Proceedings of the 2012 COMSOL Conference in Boston.
69. Metais, A., Mattei, S., Tomashchuk, I., Gaied, S.: Modelling of transport phenomena in laser welding of steels. Excerpt from the Proceedings of the 2015 COMSOL Conference in Grenoble.

PhD Thesis_Aritra Ghosh.pdf

19.09.23

Professor
Dept. of Mechanical Engineering
Jadavpur University, Kolkata-32

WORD COUNT	31528	TIME SUBMITTED	13-SEP-2023 05:42PM
		PAPER ID	102705243

PhD Thesis_Aritra Ghosh.pdf

ORIGINALITY REPORT

7%
SIMILARITY INDEX

MATCH ALL SOURCES (ONLY SELECTED SOURCE PRINTED)

★www.ajol.info
Internet
1%

EXCLUDE QUOTES	ON	EXCLUDE SOURCES	OFF
EXCLUDE BIBLIOGRAPHY	ON	EXCLUDE MATCHES	< 14 WORDS

19.09.23

Professor
Dept. of Mechanical Engineering
Jadavpur University, Kolkata-32